

Quartz Crystal Microbalance with Dissipation Monitoring Applications in Polymer Thin Films Analysis

Gehui Liu

Dissertation submitted to the faculty of the Virginia Polytechnic Institute and State University in
partial fulfillment of the requirements for the degree of

Doctor of Philosophy
in
Chemistry

Alan R. Esker, Chair
Harry C. Dorn
Louis A. Madsen
Feng Lin

December 15, 2021
Blacksburg, VA

Keywords: Chitin, Poly(ether imide), Polyethylene, Thin Films, Adsorption, Crosslinking,
Solvent Resistance, Photo-oxidation, Quartz Crystal Microbalance with Dissipation Monitoring

Copyright 2021, Gehui Liu

Quartz Crystal Microbalance with Dissipation Monitoring Applications in Polymer Thin Films Analysis

Gehui Liu

ABSTRACT

Natural and synthetic polymers are highly related to people's daily life in every perspective and determine everyone's life quality. This study investigated the interactions between polymer thin films and other molecules, specifically natural polymer films with other components in plant and fungal cell walls, crosslinked thermoplastic films with solvent molecules, as well as commodity thermoplastic films with air and moisture during aging by a powerful surface analysis instrument, a quartz crystal microbalance with dissipation monitoring (QCM-D).

The assembly and interactions of glucan and chitin are crucial for understanding the fungal infection mechanism. Adsorption of mixed-linkage glucan (MLG) onto regenerated chitin (RChitin) and cellulose (RC) surfaces were investigated by QCM-D and atomic force microscopy (AFM). MLG was irreversibly adsorbed onto both surfaces and formed soft hydrogel-like layers with viscoelastic properties. This work established a QCM-D method to mimic the assembly of natural polymers in fungal cell walls and provided insight into the interactions of these polymers with chitin and cellulose.

Poly(ether imide) (PEI) has poor solvent resistance towards solvents including chloroform, dimethylformamide (DMF), dichloromethane (DCM), and N-methyl pyrrolidone (NMP). Exposure to these solvents severely affects the thermal and mechanical performances of PEI. Therefore, crosslinked PEI (X-PEI) films was prepared from azide-terminated PEI (N₃-PEI-N₃) via a thermal crosslinking reaction. X-PEIs maintain outstanding solvent resistance towards

common solvents by swelling ratio tests using QCM-D. Meanwhile, the thermal and mechanical properties of X-PEI were enhanced compared to the original PEI.

Photo-oxidation is one of the dominant degradation mechanisms affecting the lifespan of polymers. The effect of photooxidative aging on the physiochemical properties of low-density polyethylene (LDPE) films were investigated using QCM-D, differential scanning calorimetry (DSC), and tensile stress-strain tests. The crystallinity, mechanical properties, and weight loss were correlated to understand the aging behavior. Materials after aging showed higher tensile stress and modulus, with reduced mass and elongation properties. Particularly, the aging-induced damage of polymer chain integrity was first determined by QCM-D through the evolution of mass loss during aging, providing supports to the changes of mechanical properties under aging.

Quartz Crystal Microbalance with Dissipation Monitoring Applications in Polymer Thin Films Analysis

Gehui Liu

GENERAL AUDIENCE ABSTRACT

Natural polymers and thermoplastics are two major materials that are highly related to modern life. The interactions of these polymers with other molecules are important research topics for people to understand and predict the material properties. This dissertation studied the following three topics using a quartz crystal microbalance with dissipation monitoring (QCM-D): 1) interactions between plant natural polymer films and polymers in fungal cell wall; 2) solvent resistance of crosslinked thermoplastic films; and 3) physiochemical changes during photo-oxidation degradation of thermoplastic films.

Pathogenic fungal cells can attack beneficial plant cell hosts by adhering themselves onto the plant cells, followed by penetration and enzymatic degradation of the multilayered plant cell walls until the host is digested. Therefore, the interaction between the components in fungal and plant cell walls is critical to understand pathogenic fungal cell invasion. Adsorption of mixed-linkage glucan (MLG) onto regenerated chitin (RChitin) and cellulose (RC) surfaces was monitored by QCM-D and atomic force microscopy (AFM). An irreversible binding interaction of MLG with chitin and cellulose films and a soft hydrogel-like layer on both surfaces were observed in our work.

Poly(ether imide) (PEI) is a high-performance polymer with excellent thermal and mechanical properties. However, the good solubilities in common organic solvents that facilitate reasonable processibility limits its applications in solvent-related domains. Several methods of PEI

crosslinking were developed in the literature to improve solvent resistance. This study prepared crosslinked PEI (X-PEI) films from azide-terminated PEI (N_3 -PEI- N_3) via a simple thermal crosslinking reaction. X-PEI had better resistance to organic solvents from QCM-D measurements and maintained good thermal and mechanical performances.

Photo-oxidation from air and sunlight slowly degrades plastics, shortens their service time, and leads to environmental pollution. This work bridged the gap between molecular integrity and its effect on the overall macroscopic mechanical changes through accurate measurement of the mass loss during degradation using a QCM-D. This work is essential in ensuring polymer design and active environmental protection.

Acknowledgements

First and foremost, I would like to express my deepest thanks to my dear advisor, Prof. Alan R. Esker. With his continuous encouragement, support, and guidance, I could successfully finish every milestone during my Ph.D. journey in the past four and a half years. He was always the right person I could seek for help in life and my research.

I would also like to acknowledge my committee members, Prof. Harry C. Dorn, Prof. Louis A. Madsen, and Prof. Feng Lin for their professional suggestions, feedback, and motivation. They have helped me through every stage of my Ph.D. study.

I would like to thank my closest research collaborators, Prof. Guoliang Liu and Zhen Xu. They gave me lots of inspiration in my research and I could learn new things from them in every perspective. Without their involvement and support, I could not have finished several parts of my research.

I am grateful to all my colleagues in the Esker group, Dr. Jianzhao Liu, Dr. Guoqiang Yu, Dr. Chao Wang, Tianyi Liu, Candace E. Wall, and Ethan Fink for their collaboration in research and friendship in life. I could always share my ideas as well as my happiness with them every day at lab.

I'm also grateful to the Department of Chemistry at Virginia Tech for offering me assistantships and creating such a fantastic environment to learn and study. I want to give my thanks to Dr. John Morris and Ms. Joli Huynh for the assistance they provided during every milestone of my journey.

I would like to thank my friends Dr. Yumin Dai, Zhe Wang, Dr. Xuan Zhang, Dr. Xiaodong Yu, Bowen Shen, Yumeng Zhu, Dr. Tianyu Liu, Dr. Xi Chen, Dr. Yufeng Ma, Joel Serrano, and

Shravan Uppala, whose support and time made my life so wonderful in Blacksburg. I enjoyed dancing with Xi every Monday night at McComas gym and I also had great times exploring the United States with my friends.

Finally, I would also like to thank my family members, especially my parents for their love, support, and encouragement over the years. I had only a few times for the family gathering during the past several years, however, my parents are always there supporting me.

Attributions

Dr. Guoqing Yu (Department of Chemistry at Virginia Tech) provided help and suggestions for the synthesis of trimethylsilyl chitin in Chapter 3.

Tianyi Liu (Ph.D. candidate in the Department of Chemistry at Virginia Tech) provided suggestions for the preparation of manuscript in Chapter 3.

Prof. Guoliang Liu (professor in the Department of Chemistry at Virginia Tech) provided guidance and aided in the preparation of manuscript in Chapter 4 and 5.

Zhen Xu (Ph.D. candidate in the Department of Chemistry at Virginia Tech) in the group of Prof. Guoliang Liu prepared azide terminated PEI and characterized the materials by NMR and FTIR in Chapter 4, and conducted DSC, DMA, and tensile experiments in Chapter 4 and 5.

Rachel Bianculli (Ph.D. candidate in the Department of Chemistry at Virginia Tech) in the group of Prof. Michel Schulz (professor in the Department of Chemistry at Virginia Tech) prepared poly(tetrafluorophenyl 4-vinylbenzene sulfonate) in Chapter 6.

Prof. Alan R. Esker (professor in the Department of Chemistry at Virginia Tech) supervised all the research projects and provided suggestions and help for the preparation of all the associated manuscripts.

Table of Contents

ABSTRACT	ii
GENERAL AUDIENCE ABSTRACT	iv
Acknowledgements	vi
Attributions	viii
Table of Contents	ix
List of Figures	xiv
List of Tables	xxi
Chapter 1: Overview	1
References	3
Chapter 2: Introduction and Review	5
2.1 Natural Polymers in Plant Cell Walls	5
2.1.1 Multi-layer Structure of Plant Cell Walls.....	5
2.1.2 Cellulose	7
2.1.3 Hemicellulose	9
2.1.4 Lignin.....	13
2.2 Natural Polymers in Fungal Cell Walls.....	15
2.2.1 Dynamic Structure of Fungal Cell Walls	15
2.2.2 Chitin	16

2.2.3 Glucan.....	18
2.2.4 Glycoprotein	20
2.3 Poly(ether imide).....	22
2.4 Polyethylene	25
2.5 Polymer Adsorption	26
2.6 QCM-D.....	28
2.7 References	31
Chapter 3: Viscoelastic Properties and Quantification of Mixed-Linkage β-Glucan Adsorption onto Chitin and Cellulose Surfaces	46
3.1 Abstract	46
3.2 Introduction	46
3.3 Experimental Section	49
3.3.1 Materials	49
3.3.2 Preparation of RChitin and RC Thin Films	50
3.3.3 Atomic Force Microscopy (AFM) Measurements	51
3.3.4 Film Thickness Measurements	51
3.3.5 QCM-D Measurements.....	51
3.3.6 Viscoelastic Modeling	52
3.4 Results and Discussion.....	53
3.4.1 Adsorption of MLG onto RChitin and RC Surfaces	53

3.4.2 Concentration Effects of MLG Adsorption onto RChitin and RC Surfaces	55
3.4.3 Characterization of Chitin and Cellulose Surfaces.....	56
3.4.4 Viscoelastic Properties of MLG Layers onto RChitin and RC Surfaces.....	58
3.4.5 Surface Concentration of MLG on RChitin and RC Films	62
3.5 Conclusions	64
3.6 References	65
Chapter 4: Solvent-Resistant Self-Crosslinked Poly(ether imide)	72
4.1 Abstract	72
4.2 Introduction.....	72
4.3 Experimental Section	75
4.3.1 Materials	75
4.3.2 Characterization.....	75
4.3.3 Preparation of Crosslinked PEI (X-PEI) Films	76
4.3.4 Solvent Resistance Test by QCM-D.....	76
4.4 Results and Discussion.....	77
4.4.1 Preparation of X-PEI Films	77
4.4.2 Physical Properties of X-PEIs	79
4.4.3 Solvent Resistance.....	84
4.5 Conclusions.....	90

4.6 References	91
Chapter 5: Investigation of Photo-oxidative Aging in Semi-Crystalline Polymers based upon Chemical Characterization Techniques.....	97
5.1 Abstract	97
5.2 Introduction	98
5.3 Experimental Section	101
5.3.1 Materials	101
5.3.2 UV Aging	101
5.3.3 Mechanical Testing.....	102
5.3.4 Determination of Polymer Crystallinity by Differential Scanning Calorimetry (DSC)	102
5.3.5 Evolution of Mass Loss by a Quartz Crystal Microbalance with Dissipation Monitoring (QCM-D).....	102
5.4 Results and Discussion.....	103
5.4.1 DSC Analysis	103
5.4.2 QCM-D Measurements.....	105
5.4.3 Mechanical testing.....	107
5.5 Conclusions	108
5.6 References	109
Chapter 6: Conclusions and Suggested Future Work.....	115

6.1 Overall Conclusions	115
6.2 Suggested Future Work.....	116
6.2.1 Adsorption of Mannan onto MLG coated RChitin Films and Chitinase Accessibility Evaluation.....	116
6.2.2 Interaction Parameters (χ) between Different Solvents and Regenerated Chitin (RChitin) Films.....	118
6.2.3 Crosslinking of Modified Poly(tetrafluorophenyl 4-vinylbenzene sulfonate) Films and Crosslinking Density from QCM-D Experiments.....	120
6.3 References	121

List of Figures

Chapter 2

- Figure 2.1** Basic plant cell wall structure. Reproduced from Bailey (Copyright 2007 Mariana Ruiz Villarreal).⁸ 5
- Figure 2.2** Secondary wall structure. Adapted from Complex Carbohydrate Research Center of the University of Georgia (Copyright 2001 University of Georgia).¹³ 7
- Figure 2.3** Structural repeating unit of cellulose. 7
- Figure 2.4** A representative intra/inter hydrogen bonding network in celluloses. Reproduced from Zhang (Copyright 2014 Xiao Zhang).²⁴ 8
- Figure 2.5** Interconversions of cellulose polymorphs. 9
- Figure 2.6** Structures of hemicellulose monomers. 10
- Figure 2.7** Representative structure units of (A) XXXG or (B) XXGG xyloglucan oligosaccharides and a xyloglucan segment. Reproduced from Zhang (Copyright 2014 Xiao Zhang).²⁴ 11
- Figure 2.8** Representative chemical structures of (A) a xyloglucan, (B) a galactomannan, (C) a glucomannan, (D) an arabinoxylan and (E) a glucuronoarabinoxylan. Reproduced from Wang (Copyright 2014 Chao Wang).³⁴ 12
- Figure 2.9** Structure of a mixed linkage glucan. Letter x is the degree of polymerization in the oligosaccharide units and n is the number of the 13

oligosaccharide units. Reproduced from Zhang (Copyright 2014 Xiao Zhang).²⁴

Figure 2.10	Chemical structures of common monolignols.	14
Figure 2.11	Schematic representation of a softwood lignin structure. Reproduced from Tolbert et al. (Copyright 2010 American Chemistry Society). ⁴⁰	14
Figure 2.12	Basic fungal cell wall structure. Reproduced from Antifungal Pharmacology (Copyright 2018 Mycoses Study Group Education and Research Consortium). ⁴⁷	16
Figure 2.13	Repeating unit of chitin.	17
Figure 2.14	Representative components in the fungal cell wall. Green hexagons connected in a chain represent chitin. Adapted from Gurr et al. (Copyright 2017 Elsevier). ⁴⁶	18
Figure 2.15	Structure of a β -1,3-glucan backbone with a β -1,6-glucan branch. The β -1,6-glucan is highlighted in red. Reproduced from Yu (Copyright 2021 Guoqiang Yu). ⁶³	19
Figure 2.16	β -1,3-glucan and its synthesis in the fungal cell wall. Reproduced from Monteiro et al. (Copyright 2019 IntechOpen). ⁶⁵	20
Figure 2.17	Fungal cell wall biosynthesis. Reproduced from Bowman et al. (Copyright 2006 Wiley). ⁴¹	21
Figure 2.18	Chemical structure of Polyetherimide.	22
Figure 2.19	Industrial processing of PEI.	23

Figure 2.20	Methods for decreasing processing temperatures in the literature: (A) blending PEI with a polymer processable at lower temperatures (B-D) using PEI oligomers compensated by enhanced intermolecular interactions, including (B) quadrupole hydrogen bonding, (C) anionic interactions, (D) cationic interactions, and (E) crosslinking. Reproduced from Xu et al. (Copyright 2021 Wiley). ⁷¹	24
Figure 2.21	Schematic representation of polyethene degradation. Reproduced from Ghatge et al. (Copyright 2020 Springer). ¹⁰⁷	26
Figure 2.22	Polymer formation of (a) an adsorption layer and (b) a depletion layer at a solid substrate surface. ϕ , polymer volume fraction; z , distance from the substrate surface; ϕ_s , polymer volume fraction at the surface; ϕ_b , polymer volume fraction in the bulk solution. Reproduced from Zhang (Copyright 2014 Xiao Zhang). ²⁴	27
Figure 2.23	Conformation of an adsorbed neutral polymer chain. Reproduced from Zhang (Copyright 2014 Xiao Zhang). ²⁴	28
Figure 2.24	Representative profile of (A) a QCM crystal and (B) a QCM crystal oscillating in a shear thickness mode in an alternating electric field. Reproduced from Wang (Copyright 2014 Chao Wang). ³⁴	29
Figure 2.25	Demonstration of the energy dissipation after the power is turned off in a QCM-D. Reproduced from Wang (Copyright 2014 Chao Wang). ³⁴	30
Figure 2.26	Representative depiction of the fitting parameters generated by the	31

Voigt-based viscoelastic modeling system in a QCM-D. Reproduced from Hook et al. (Copyright 2001 American Chemistry Society).¹³⁶

Chapter 3

- Figure 3.1** Dynamic fungal invasion into plant system. Reproduced from Lionetti et al. (Copyright 2014 Frontiers).¹⁷ 48
- Figure 3.2** Time-dependent $\Delta f/n$ and ΔD profiles for MLG solution ($100 \mu\text{g g}^{-1}$) adsorbed on (A) RChitin surface and (B) RC surface. Curves correspond to the fifth overtone. 54
- Figure 3.3** Summary of $\Delta f/n$ and ΔD for MLG adsorption onto RChitin and RC Surfaces at different MLG concentrations. 56
- Figure 3.4** AFM height images ($2 \mu\text{m} \times 2 \mu\text{m}$) of morphology on different surfaces. (A) RChitin, (B) RC, (C) MLG coated RChitin, (D) MLG coated RC. RMS roughnesses for the images are (A) ~ 1.7 nm, (B) ~ 1.6 nm, (C) ~ 2.2 nm, and (D) ~ 2.6 nm. 58
- Figure 3.5** Adsorption of MLG ($100 \mu\text{g g}^{-1}$) onto a RChitin substrate from SA buffer at 20°C and best fits were obtained from Voigt-based viscoelastic modeling. Isolated symbols represent the experimental data from $n = (\bullet) 3, (\blacktriangle) 5, (\blacksquare) 7, (\blacktriangledown) 9, (\blacklozenge) 11$ and $(\blacktriangleright) 13$ and solid lines represent fits of the experimental data set. 61
- Figure 3.6** Representative time dependent evolution of changes in parameters associated with the frequency-dependent viscoelastic modeling for the 62

adsorption of MLG ($100 \mu\text{g g}^{-1}$) onto a RChitin substrate: (A) thickness versus time; (B) shear elastic modulus versus time; (C) viscosity versus time; (D) frequency dependence α' of μ and α'' of η versus time.

Figure 3.7 Surface concentrations versus bulk concentrations for MLG adsorption onto (A) RChitin and (B) RC surfaces at $20 \text{ }^\circ\text{C}$. The dashed line is present to approximate a plateau value and facilitate comparisons. 64

Chapter 4

Figure 4.1 Synthesis and preparation of $\text{N}_3\text{-PEI-N}_3$ and X-PEI. 78

Figure 4.2 (A) ^1H NMR of $\text{NH}_2\text{-PEI-NH}_2$ and $\text{N}_3\text{-PEI-N}_3$ with $M_n = 8.9 \text{ kDa}$. (B) FTIR spectra of $\text{NH}_2\text{-PEI-NH}_2$ ($M_n = 8.9 \text{ kDa}$) and $\text{N}_3\text{-PEI-N}_3$ with varying molecular weights. 79

Figure 4.3 (A) Storage moduli and (B) $\text{Tan } \delta$ of Ultem 1010 and XPEIs. (C) Tensile stress–strain curves of Ultem 1010, X-PEI-15, and X-PEI-12 measured at room temperature. 81

Figure 4.4 DSC and TGA traces of Ultem 1010, $\text{NH}_2\text{-PEI-NH}_2$, X-PEI-7, X-PEI-8, X-PEI-12, and X-PEI-15. The legend for B also applies to A. The arrows indicate T_g . 83

Figure 4.5 Solvent resistance of X-PEI-8 in NMP, DMF, chloroform, DCM, and THF. X-PEI-8 was resistant to all solvents, while the noncrosslinked $\text{NH}_2\text{-PEI-NH}_2$ and $\text{N}_3\text{-PEI-N}_3$ were soluble in NMP, DMF, chloroform, and DCM, and softened in THF. 85

Figure 4.6	QCM-D vapor adsorption tests of THF, DCM, chloroform, hexanes, and methanol on various PEIs at 20 °C. The activities for all solvents were ~0.9.	87
Figure 4.7	Bending test of an X-PEI-8 film (A) in a dry state, (B) immersed in CHCl ₃ and saturated by the solvent, and (C) saturated by CHCl ₃ but out of the solvent.	89
Figure 4.8	Flexibility test of N ₃ -PEI-N ₃ -7 and X-PEI-7 (top) Before crosslinking, N ₃ -PEI-N ₃ -7 cannot form intact films by solution casting. (Bottom) After crosslinking, X-PEI-7 film showed drastically improved flexibility. The film remained intact after abusive folding, stretching, and tension.	89
Figure 4.9	Upon folding, X-PEI-8 film saturated by CHCl ₃ showed a crack near the folding line.	90
Chapter 5		
Figure 5.1	Degradation pathways of synthetic polymers under environmental factors. Reproduced from Knepper et al. (Copyright 2018 Springer). ¹¹	99
Figure 5.2	(A) Evolution of crystallinity as a function of photo-oxidation aging time obtained from DSC, (B) DSC thermograms of LDPE films with varying photo-oxidation aging times.	104
Figure 5.3	Schematic representation of chemi-crystallization due to photo-oxidation. Upon exposure to UV light, the molecular chains in the	105

amorphous region break and degrade causing the formation of additional crystals within the amorphous domain.

Figure 5.4 Evolution of the minute mass ratio between the aged and unaged samples as a function of photo-oxidation aging time obtained from the QCM-D test. The minute mass ratio is presented for three film thicknesses: 200 nm, 158 nm, and 146 nm represented by circles, diamonds, and squares, respectively. 107

Figure 5.5 Average stress-strain curves from each LDPE film with three replicates corresponding to different aging times (i.e., 0, 40, 74, 98, and 112 h). 108

Chapter 6

Figure 6.1 Process of fungal invasion into plants. 117

Figure 6.2 Structures of the fungal cell walls. Adapted from Hardison et al. (Copyright 2012 Springer Nature).⁹ 118

Figure 6.3 Crosslinking of modified poly(tetrafluorophenyl 4-vinylbenzene sulfonate) films. 121

List of Tables

Chapter 3

Table 3.1A	Thickness and Viscoelastic Parameters of Adsorbed MLG Layers on RChitin Surfaces from Voigt-Based Model.	60
Table 3.2B	Thickness and Viscoelastic Parameters of Adsorbed MLG Layers on RC Surfaces from Voigt-Based Model.	60

Chapter 4

Table 4.1	Physical properties of N ₃ -PEI-N ₃ and X-PEIs.	84
Table 4.2	Solvent resistance of N ₃ -PEI-N ₃ and X-PEIs.	87
Table 4.3	Hansen solubility parameters and total solubility parameters of PEI, DCM, chloroform, and THF.	88

Chapter 6

Table 6.1	Vapor sorption results between pyridine and RChitin films.	121
------------------	--	-----

Chapter 1: Overview

During recent times, natural polymers have gained increasing interest because of their abundance in nature, biodegradability, and sustainability.¹⁻³ They provide alternate solutions for the renewable materials and serve as functional materials for different applications.⁴⁻⁵ Large amounts of natural polymers are found in plant and fungal cell walls, and they play a significant role in ecological systems. A complete understanding of their interactions is essential to unveil the fundamental mechanism of fungal cell wall assembly and fungal invasion of plants.

Thermoplastics, on the other hand, are highly related to modern life and industries, from plastic packaging to medical devices and aerospace exploration.⁶⁻⁸ However, there are still some barriers (*e.g.*, solvent resistance, degradation, plastic lifetime prediction, sustainability, etc.) that limit the applications of thermoplastics.⁹⁻¹⁰ Therefore, developing methods to investigate these issues and provide corresponding solutions are of great importance for their applications.

A quartz crystal microbalance with dissipation monitoring (QCM-D) is a powerful surface analysis instrument, and it enables real-time, label free measurements of molecular adsorption and/or interactions on surfaces.¹¹⁻¹² QCM-D not only quantifies mass changes but provides novel insights regarding structural (viscoelastic) properties of adsorbed layers.¹³ Based upon these advantages, in this dissertation, QCM-D is introduced to investigate the interactions between natural polymer films in plant and fungal cell walls, solvent resistance of thermoplastics films, as well as the evolution of mass changes during degradation of plastic films.

Chapter 2 gives an overall introduction to the structure of plant and fungal cell walls and the major polymeric components, such as cellulose (plant cell walls) and chitin (fungal cell walls). At the same time, two common thermoplastics, polyetherimide and polyethylene, are also introduced with general properties, applications, and research motivation. In addition, interfacial adsorption

is briefly introduced. Finally, QCM-D, as a key surface analysis technique, is discussed with respect to the principles and primary applications.

Chapter 3 introduces a QCM-D method to mimic the assembly of natural polymers in fungal and plant cell walls and monitor the adsorption of mixed-linkage glucan (MLG) onto regenerated chitin (RChitin) and cellulose (RC) surfaces. The morphology changes during adsorption are studied by atomic force microscopy (AFM). Viscoelastic modeling method is used to interpret the QCM-D data of the adsorbed MLG layers.

Chapter 4 presents the preparation of crosslinked PEI (X-PEI) films via a thermal trigger method. The thermal and mechanical properties of X-PEIs with different molecular weights are investigated by differential scanning calorimetry (DSC) and dynamic mechanical analyzer (DMA), respectively. More importantly, QCM-D is utilized to study and compare the solvent resistance of PEI before and after crosslinking for common organic solvents including methanol, dimethylformamide (DMF), chloroform, dichloromethane (DCM), and hexane.

Chapter 5 describes the effect of photooxidative aging on the physiochemical properties of low-density polyethylene (LDPE) using QCM-D, DSC, and tensile stress-strain characterizations. The crystallinity, mechanical properties, and weight loss were correlated to understand the aging behavior. Particularly, polymer film damage induced by aging was first determined by QCM-D through the evolution of mass loss during aging, providing supports to the evolution of mechanical properties during aging.

Chapter 6 provides overall conclusions of this dissertations as well as suggestions for the future work related to this dissertation.

References

1. Kulkarni Vishakha, S.; Butte Kishor, D.; Rathod Sudha, S., Natural polymers-A comprehensive review. *Int. J. Res. Pharm. Biomed. Sci.* **2012**, *3*, 1597-1613.
2. Thomas, S. P.; Visakh, P.; Mathew, A. P., Advances in natural polymers. *Adv. Struct. Mater.* **2013**, *8*, 255-312.
3. Wang, C. Renewable natural polymer thin films and their interactions with biomacromolecules. Ph.D. Dissertation, Virginia Tech, Blacksburg, VA, 2014.
4. Shanmugam, S.; Manavalan, R.; Venkappayya, D.; Sundaramoorthy, K.; Mounnissamy, V. M.; Hemalatha, S.; Ayyappan, T., Natural polymers and their applications. *Nat. Prod. Res.* **2005**, *4*, 478-481.
5. Olatunji, O., *Natural polymers: industry techniques and applications*. Springer: 2015.
6. Yin, J.; Zhu, G.; Deng, B., Multi-walled carbon nanotubes (MWNTs)/polysulfone (PSU) mixed matrix hollow fiber membranes for enhanced water treatment. *J. Membr. Sci.* **2013**, *437*, 237-248.
7. Karataş, M. A.; Gökkaya, H., A review on machinability of carbon fiber reinforced polymer (CFRP) and glass fiber reinforced polymer (GFRP) composite materials. *Def. Technol.* **2018**, *14*, 318-326.
8. Benzait, Z.; Trabzon, L., A review of recent research on materials used in polymer–matrix composites for body armor application. *J. Compos. Mater.* **2018**, *52*, 3241-3263.
9. Xu, Z.; Croft, Z. L.; Guo, D.; Cao, K.; Liu, G., Recent development of polyimides: Synthesis, processing, and application in gas separation. *J. Polym. Sci.* **2021**, *59*, 943-962.
10. Cao, K.; Guo, Y.; Zhang, M.; Arrington, C. B.; Long, T. E.; Odle, R. R.; Liu, G., Mechanically strong, thermally stable, and flame retardant poly (ether imide) terminated with phosphonium bromide. *Macromolecules* **2019**, *52*, 7361-7368.

11. Dixon, M. C., Quartz crystal microbalance with dissipation monitoring: enabling real-time characterization of biological materials and their interactions. *J. Biomol. Tech.* **2008**, *19*, 151-158.
12. Tuantranont, A.; Wisitsora-At, A.; Sritongkham, P.; Jaruwongrungrunsee, K., A review of monolithic multichannel quartz crystal microbalance: A review. *Anal. Chim. Acta* **2011**, *687*, 114-128.
13. Höök, F.; Kasemo, B., The QCM-D technique for probing biomacromolecular recognition reactions. *Piezoelectric sensors* **2006**, *5*, 425-447.

Chapter 2: Introduction and Review

2.1 Natural Polymers in Plant Cell Walls

Plant cell walls are semi-permeable multi-layered structures that are comprised of cellulose, hemicelluloses, pectin and proteins in primary cell walls and cellulose, hemicelluloses and lignin in secondary cell walls.¹⁻³ Because of their exterior location next to plant cell membranes, plant cell walls play significant roles in forming the shape of plant cells, plant growth, intercellular communication, protection, absorption and secretion of substances in plant cells.⁴ Plant cell walls expand through a process of controlled polymer creep, which involves enzymatic hydrolysis of the polysaccharides or rearrangement of the matrix.^{1, 5}

2.1.1 Multi-layer Structure of Plant Cell Walls

Plant cell walls are composed of three different layers: the middle lamella forming the interface between adjacent plant cells, primary walls surrounding the growing cells or cells capable of growth, and secondary walls surrounding the specialized cells such as vessel elements or fiber cells.⁶⁻⁷ The cell wall structure is schematically depicted in Figure 2.1.

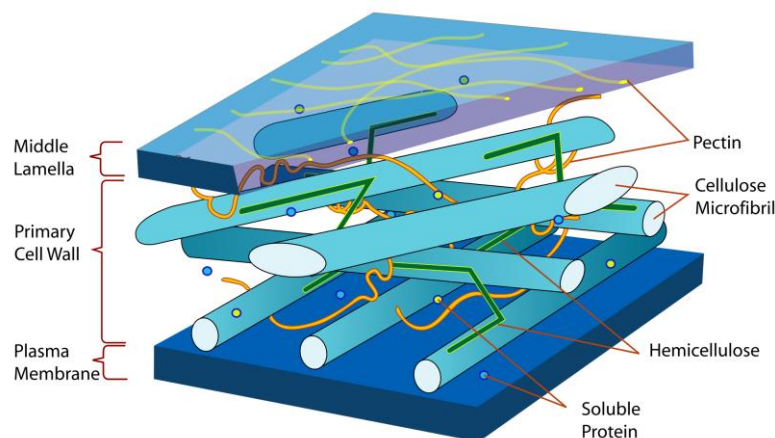


Figure 2.1 Basic plant cell wall structure. Reproduced from Bailey (Copyright 2007 Mariana Ruiz Villarreal).⁸

The middle lamella, a glue-like layer between cells, is the outermost plant cell wall and is laid down before the primary cell wall. It glues adjacent cells together and contributes to tissue cohesion.⁹ The middle lamella is a highly enriched biomaterial mainly composed of pectins, which have adhesive properties. The primary cell wall is a flexible and extendable layer, formed among actively growing cells or cells capable of growth. Primary cell walls are mainly composed of cellulose, hemicelluloses, pectin and proteins with a thickness around 0.1 μm .¹⁰ The cellulose microfibrils are accumulated during the time of growth in the primary cell wall. After accumulation, the primary wall may stop growing due to an increase in rigidity or cell wall thickness. Cellulose microfibrils and hemicelluloses are physically cross-linked into a network that may contain other cell wall components.¹¹ The secondary cell wall is deposited when the cells stop growing and is therefore a thick layer between the primary cell wall and the cell membrane. With a thickness of 10 to 20 μm , secondary walls can occupy most of the volume of the plant cell, thus becoming the major component of woody tissues. In some cases, the secondary cell wall can be separated into three different layers S1, S2 and S3 based upon the orientation of cellulose microfibrils (Figure 2.2).¹¹ Cellulose, hemicelluloses and lignin are the main components of secondary cell walls. Compared with primary cell walls, secondary cell walls have different compositions and are much thicker. Many secondary cell walls are filled with lignin, which serves as a waterproofing agent and also provides mechanical strength.¹²

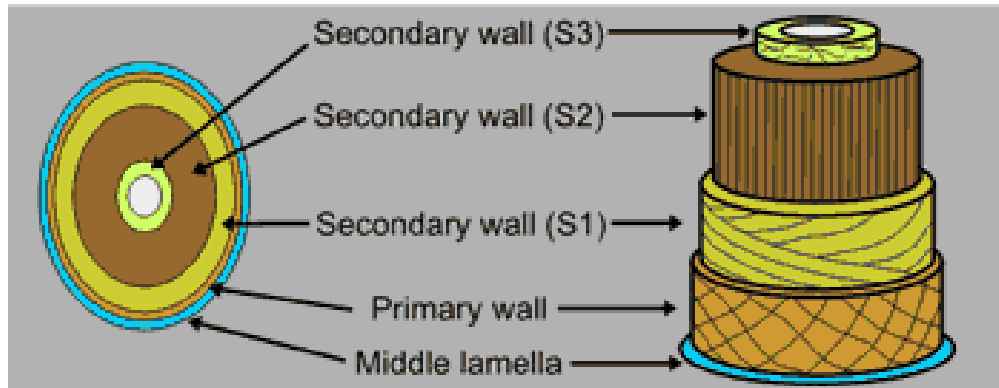


Figure 2.2 Secondary wall structure. Adapted from Complex Carbohydrate Research Center of the University of Georgia (Copyright 2001 University of Georgia).¹³

2.1.2 Cellulose

Cellulose was discovered in 1838 by Anselme Payen, who isolated it from plant cell walls and identified its chemical formula.¹⁴⁻¹⁵ As the most abundant organic substance on the planet, cellulose is the major polymer constituent of plant cell walls. It accounts for around 50% of dry wood, 57% of dried hemp, and 90% of cotton by mass.¹⁵⁻¹⁶ Cellulose is a linear polysaccharide of D-glucose units linked together by β -(1 \rightarrow 4) glycosidic bonds that are found in the primary plant cell wall. The glucose dimer of cellobiose is the structural repeating unit of cellulose shown in Figure 2.3. In plant cell walls, cellulose is synthesized by the cellulose synthase complex in the plasma membrane and cellulose chains can aggregate and be linked by hydrogen bonds to form crystalline microfibrils that are mechanically strong and highly resistant to enzymatic attack.¹⁷

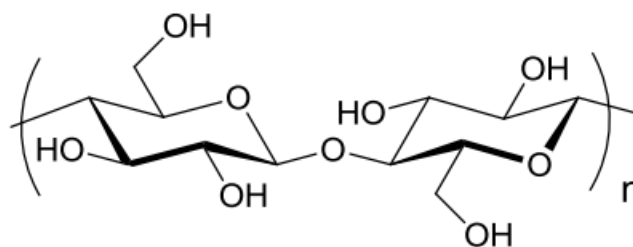


Figure 2.3 Structural repeating unit of cellulose.

Cellulose is tasteless, odorless, and insoluble in water and most organic solvents owing to strong intermolecular and intramolecular hydrogen bonding.¹⁸⁻¹⁹ However, some solvent systems have been found for the dissolution of cellulose, including N,N-dimethylacetamide (DMAc)/lithium chloride (LiCl),²⁰ N-methylmorpholine-N-oxide (NMNO),²¹ phosphoric acid as well as various ionic liquids.²² Six different crystalline structures of cellulose (I, II, III₁, III₁₁, IV₁, IV₁₁) are known, corresponding to the location of hydrogen bonds between and within strands (Figure 2.4).²³ The interconversions between these cellulose polymorphs are summarized in Figure 2.5. In nature, cellulose is partially crystalline, including both highly ordered crystalline cellulose I and disordered amorphous regions.

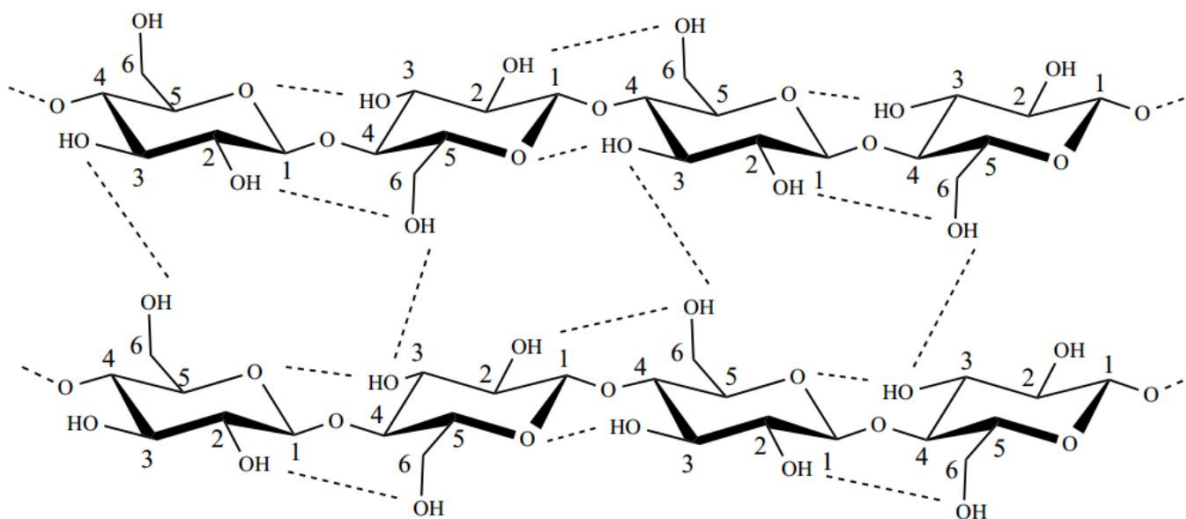


Figure 2.4 A representative intra/inter hydrogen bonding network in celluloses. Reproduced from Zhang (Copyright 2014 Xiao Zhang).²⁴

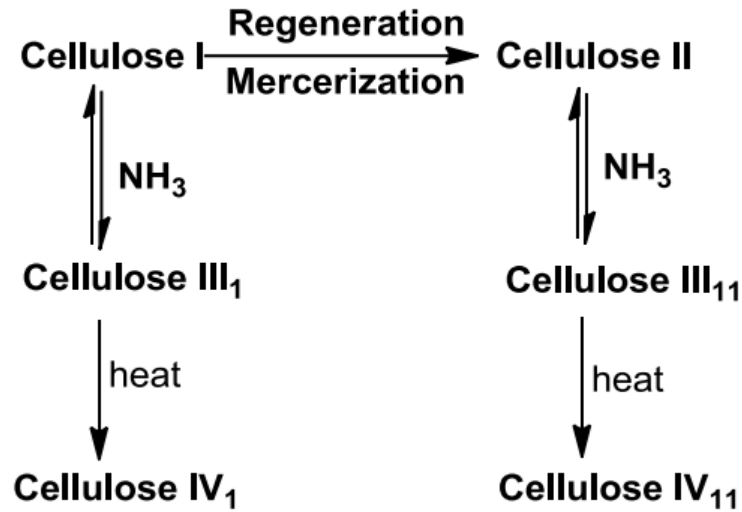


Figure 2.5 Interconversions of cellulose polymorphs.

2.1.3 Hemicellulose

Hemicelluloses, found in almost all primary and secondary plant cell walls, comprise 25 to 33% of the plant mass and the exact value is dependent upon plant species and growth period.²⁵ Compared with cellulose, which is linear, crystalline, and resistant to hydrolysis, hemicelluloses are amorphous and branched polysaccharides composed of various monosaccharides, including D-glucopyranose, D-galactopyranose, D-mannopyranose, D-xylopyranose, L-arabinofuranose, and L-rhamnopyranose (Figure 2.6). Because of shorter chain lengths or lower degrees of polymerization, hemicelluloses relative to cellulose are more easily hydrolyzed by dilute base or acid as well as a myriad of hemicellulases.¹ In plant cell walls, hemicelluloses are linked to cellulose by hydrogen bonds and connected to lignin by covalent and physical interactions forming a cross-linked network.²⁶ Hemicelluloses are synthesized from nucleotide sugars in the Golgi apparatus by glycan synthases. After synthesis, hemicelluloses are transported to the plasma membrane via Golgi vesicles.²⁷ Hemicelluloses have widespread applications in drug delivery, pulp, paper products, and energy industries.²⁸⁻³⁰

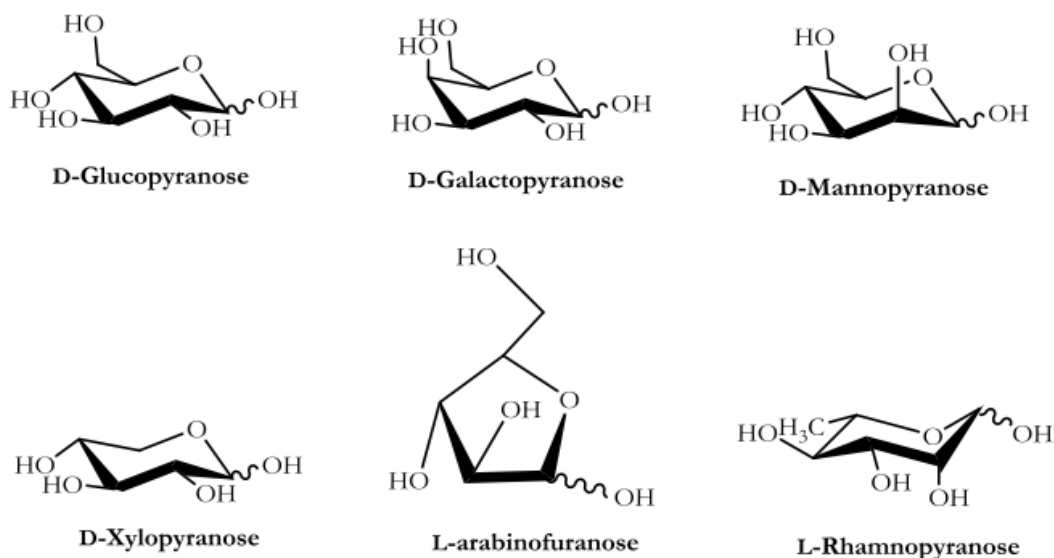


Figure 2.6 Structures of hemicellulose monomers.

In general, hemicelluloses are categorized as xyloglucans, xylans, β -glucans and mannans based upon different sugar monomers.³¹ Xyloglucans (Figure 2.7), the most abundant hemicelluloses in the primary cell walls of non-graminaceous plants, have a backbone similar to cellulose and can be decorated with xylose branches on 3 out of 4 glucose residues. As the principal coating and crosslinking polysaccharides, xyloglucans are closely connected to cellulose by surface adsorption and entrapment within the cellulose microfibrils.³² Xylans are also an abundant hemicellulose and have β -(1 \rightarrow 4)-D-xylose linkages for their backbone and various side group substituents on the O-2 and O-3 positions.³³ In nature, glucuronoxylans make up around 10 to 35% of hemicelluloses in hardwoods by mass and arabinoglucuronoxylans accounts for 10 to 15% of hemicelluloses in softwoods by mass.³¹ Mannans have backbones of β -(1 \rightarrow 4) linked D-mannose or a combination of D-mannose and D-glucose (glucomannan). The O-6 positions of mannans are widely modified with α -D-galactosyl residues. Mannans can represent up to 90% of hemicelluloses in plants by mass.³¹ The representative chemical structures for xyloglucans, galactomannans, glucomannans, arabinoxylan and glucuronoarabinoxylans are shown in Figure 2.8.

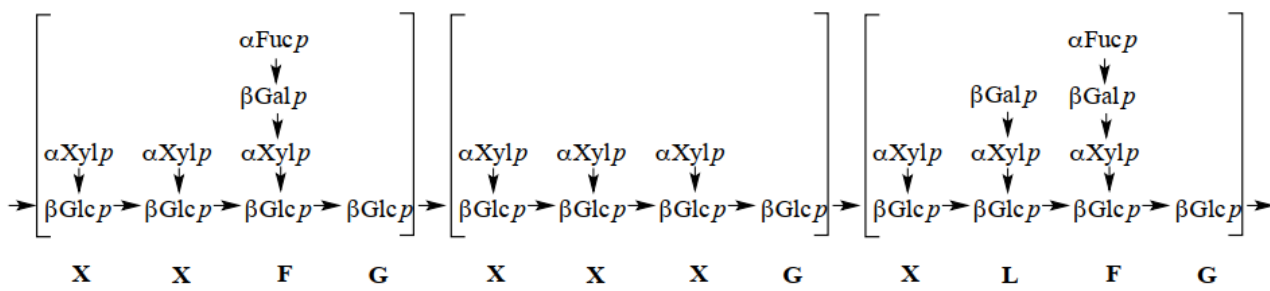
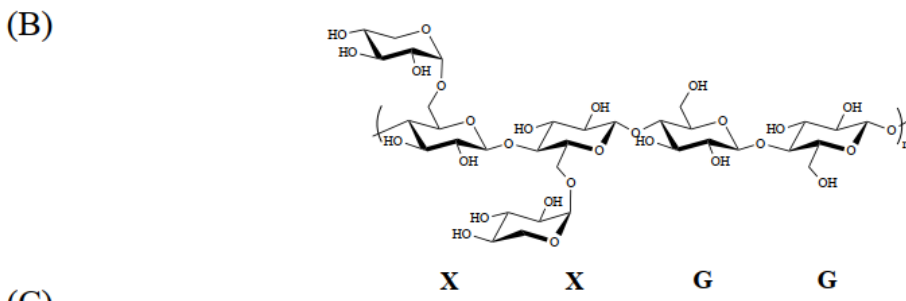
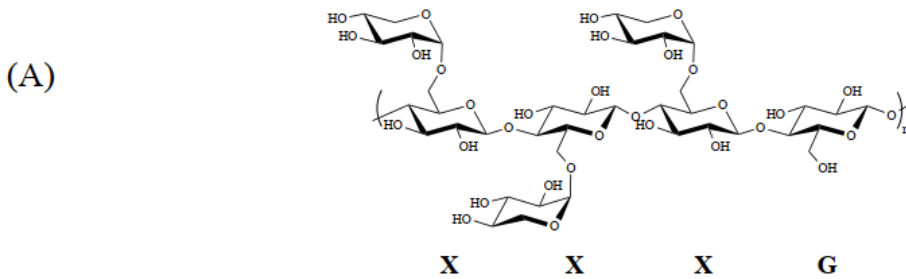


Figure 2.7 Representative structure units of (A) XXXG or (B) XXGG xyloglucan oligosaccharides and a xyloglucan segment. Reproduced from Zhang (Copyright 2014 Xiao Zhang).²⁴

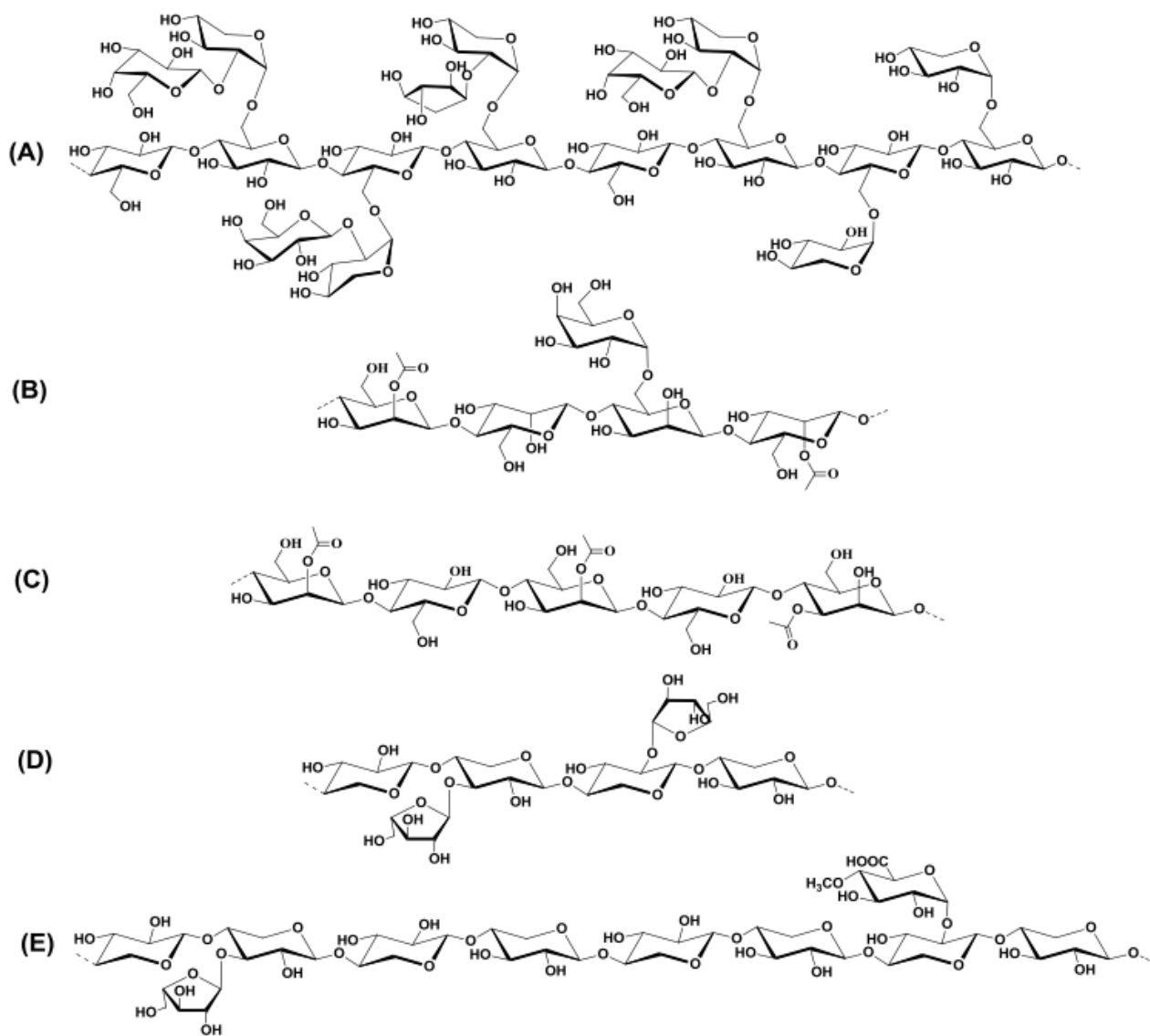


Figure 2.8 Representative chemical structures of (A) a xyloglucan, (B) a galactomannan, (C) a glucomannan, (D) an arabinoxylan and (E) a glucuronoarabinoxylan. Reproduced from Wang (Copyright 2014 Chao Wang).³⁴

Mixed linkage glucans (MLGs) account for about 3 to 5% of the cell wall dry mass of Poales, cereals and some fungal species.³⁵ The MLGs are unbranched polysaccharides consisting of β -D(1-3) and β -D(1-4) linked glucose as shown in Figure 2.9. Being connected with cellulose

microfibrils during cell growth, MLGs will be hydrolyzed into small fragments after the growth is finished. Hence, a critical role in cell wall growth is inferred.³⁶

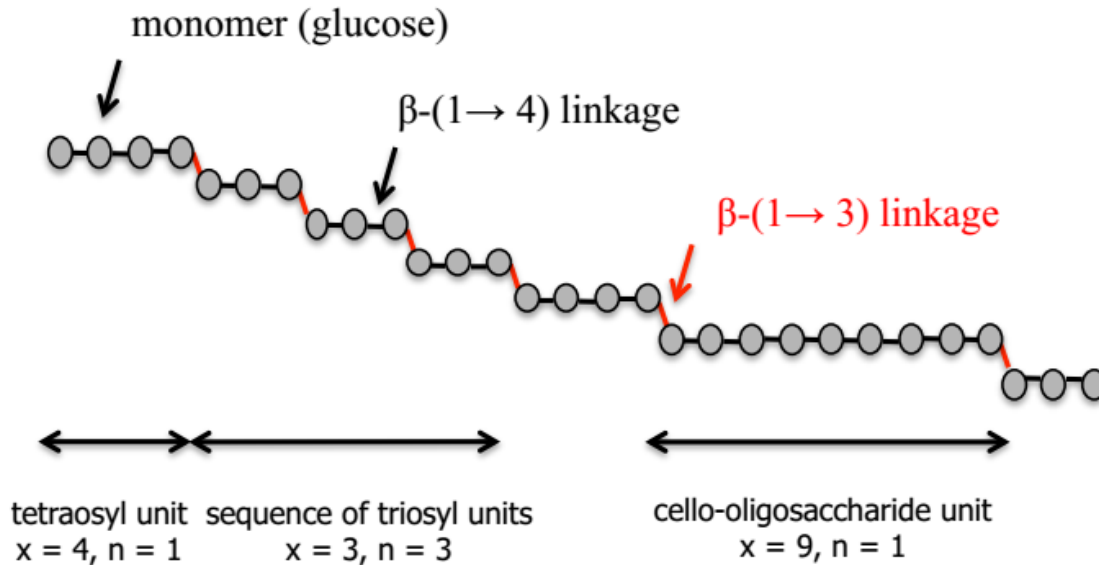


Figure 2.9 Structure of a mixed linkage glucan. Letter x is the degree of polymerization in the oligosaccharide units and n is the number of the oligosaccharide units. Reproduced from Zhang (Copyright 2014 Xiao Zhang).²⁴

2.1.4 Lignin

Lignin is a cross-linked phenolic heteropolymer that forms important structural material in the xylem tissues of vascular plants. As one of the most abundant organic polymers on earth, lignin accounts for 30% of non-fossil organic carbon and 20 to 35% of the dry mass of wood.³⁷⁻³⁸ Owing to the hydrophobic nature, lignin serves as waterproofing agents in vascular tissues, thus enabling water and nutrient transport throughout plants.³⁷ Three primary monolignols have been identified for the synthesis of lignin in plant cell walls: p-coumaryl alcohol, coniferyl alcohol, and sinapyl alcohol. The chemical structures of these three monolignols are shown in Figure 2.10, differing in the degree of methoxylation. Although many efforts have been made to elucidate the structure of

native lignin, the exact structure is still unpredictable due to the structural complexity and inevitable damage during the isolation process. More recently, non-traditional lignin building blocks have been discovered.³⁹ Figure 2.11 shows a schematic representation of a softwood lignin structure.

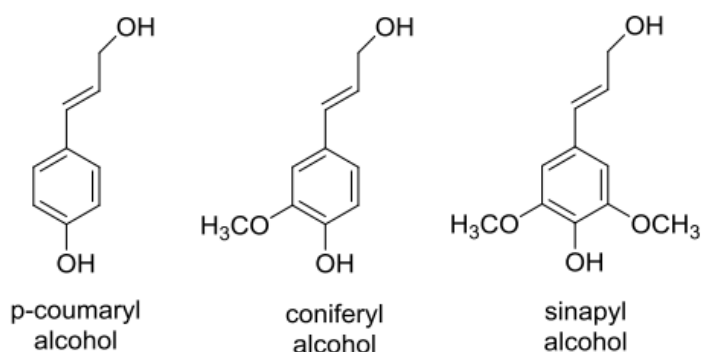


Figure 2.10 Chemical structures of common monolignols.

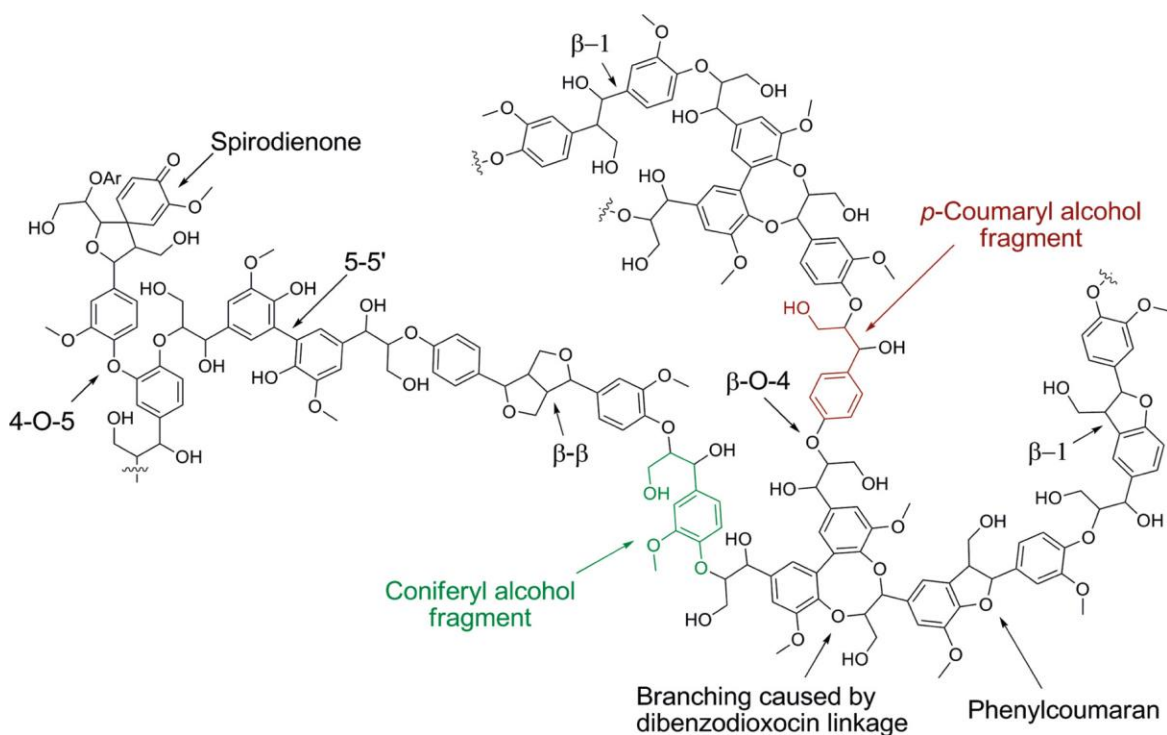


Figure 2.11 Schematic representation of a softwood lignin structure. Reproduced from Tolbert et al. (Copyright 2010 American Chemistry Society).⁴⁰

2.2 Natural Polymers in Fungal Cell Walls

Fungal cell walls are dynamic structures that can protect fungal cells from changes in osmotic pressure and other external conditions, while making it possible for fungal cells to interact simultaneously with their surroundings. Based upon this dynamic cell wall structure, fungal cell walls are of significant importance for the growth, survival, and morphogenesis of fungi by providing protection, mechanical strength, adequate plasticity, and a pathway for communications with their surroundings.⁴¹⁻⁴² Concurrently, the pathogenic fungal cell walls are vital for virulence and pathogenicity. The cell walls of pathogenic fungi mediate cell adhesion and adherence to other substrates, which is critical for invasion of host tissue.

2.2.1 Dynamic Structure of Fungal Cell Walls

The primary components in fungal cell walls are chitin, glucans and glycoproteins.⁴³ Although variations in composition and organization for different fungal species and cell types exist, the cell wall is organized as shown in Figure 2.12. Chitin is synthesized by plasma membrane-associated chitin synthases and most of the chitin is located next to the plasma membrane as a linear polymer.⁴⁴ The glucans, which are synthesized by plasma membrane-associated glucan synthases, extend from the plasma membrane into the whole cell wall space.⁴² The glycoproteins are synthesized in endoplasmic reticulum-associated ribosomes and many of them have glycosylphosphatidylinositol (GPI) anchors, which makes them stick to the plasma membrane while others are secreted into the cell wall space.⁴⁵ Once chitin, glucans and glycoproteins are extruded into the cell wall space, they are covalently cross-linked into a complex network by cross-linking enzymes, which forms the structural basis and strengthens fungal cell walls.⁴⁶

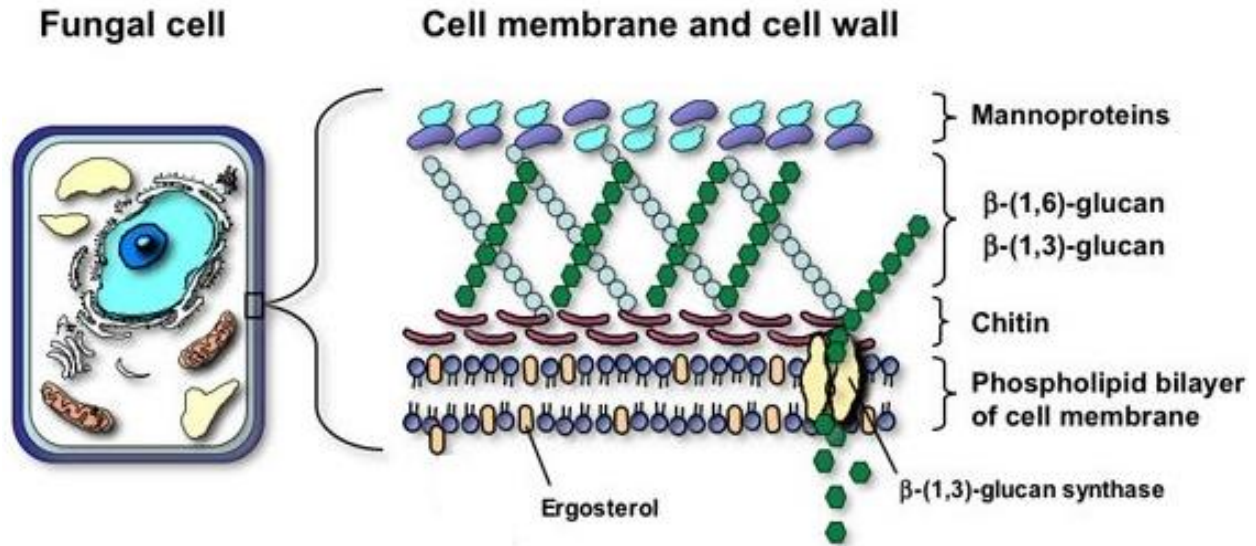


Figure 2.12 Basic fungal cell wall structure. Reproduced from Antifungal Pharmacology (Copyright 2018 Mycoses Study Group Education and Research Consortium).⁴⁷

2.2.2 Chitin

Chitin, a linear natural polysaccharide composed of β -1,4-linked N-acetylglucosamine units (Figure 2.13), is the structurally important component of fungal cell walls.⁴⁸⁻⁴⁹ Chitin accounts for 1 to 20% of the fungal cell wall mass, with yeast cell walls having only 1 to 2% chitin by mass, whereas filamentous fungal cell walls have up to 20% chitin by mass.⁵⁰⁻⁵² The synthesis of chitin is controlled by plasma membrane-associated chitin synthases and the elongation of chitin occurs by the addition of N-acetylglucosamine to the non-reducing end of chitin so that chitin can be extruded through the plasma membrane into the cell wall space.⁵³⁻⁵⁴

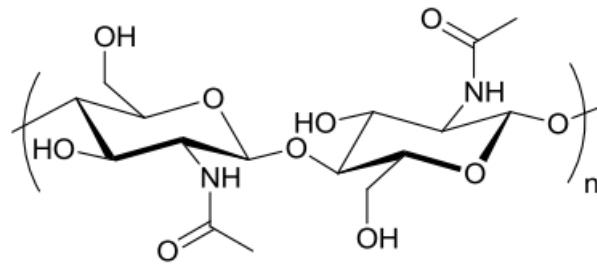


Figure 2.13 Repeating unit of chitin.

Chitin in the cell wall space can take part in interchain hydrogen bonding that results in microfibril formation with a highly crystalline structure (Figure 2.14). These microfibrils have an enormous tensile strength and significantly contribute to the overall integrity of the cell wall. Therefore, when chitin synthesis is disrupted, the fungal cell becomes malformed and osmotically unstable with a disorganized cell wall.⁵⁵ Because of the critical role chitin plays in the fungal cells, chitin synthesis has been considered a prime target for anti-fungal agents. Well-known chitin synthase inhibitors are naturally occurring nikkomycins and polyoxins which are the analogs of the chitin synthase substrate and serve as competitive inhibitors for chitin synthases. Nikkomycins and polyoxins are often used in conjunction with other anti-fungal agents.⁵⁶⁻⁵⁷

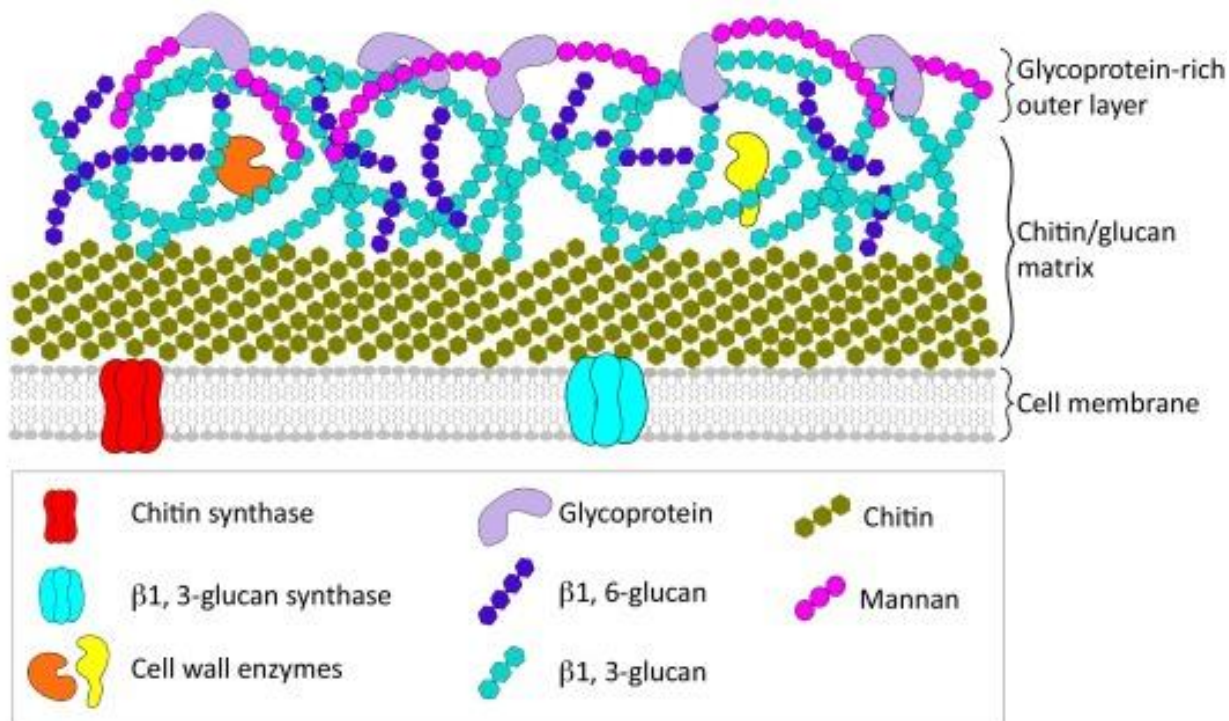


Figure 2.14 Representative components in the fungal cell wall. Green hexagons connected in a chain represent chitin. Adapted from Gurr et al. (Copyright 2017 Elsevier).⁴⁶

2.2.3 Glucan

Glucan, as one of the principle structural polysaccharides of the fungal cell wall, makes up approximately 50 to 60% of the cell wall by mass.⁵⁸ Repeating glucose residues, which are assembled into chains via various chemical linkage, constitute glucan polysaccharides. In general, β-1,3-glucan is the major glucan polymer which contributes 65 to 90% of the fungal cell wall glucan by mass.⁵⁹ Meanwhile, there are also many other types of glucans that have been found in different fungal cell walls, such as mixed β-1,3- and β-1,4-glucan, α-1,3- glucan, and β-1,6-glucan.⁶⁰⁻⁶¹ The most common structure of glucan is a β-1,3-glucan backbone with β-1,6-glucan branches, as depicted in Figure 2.15.⁶²

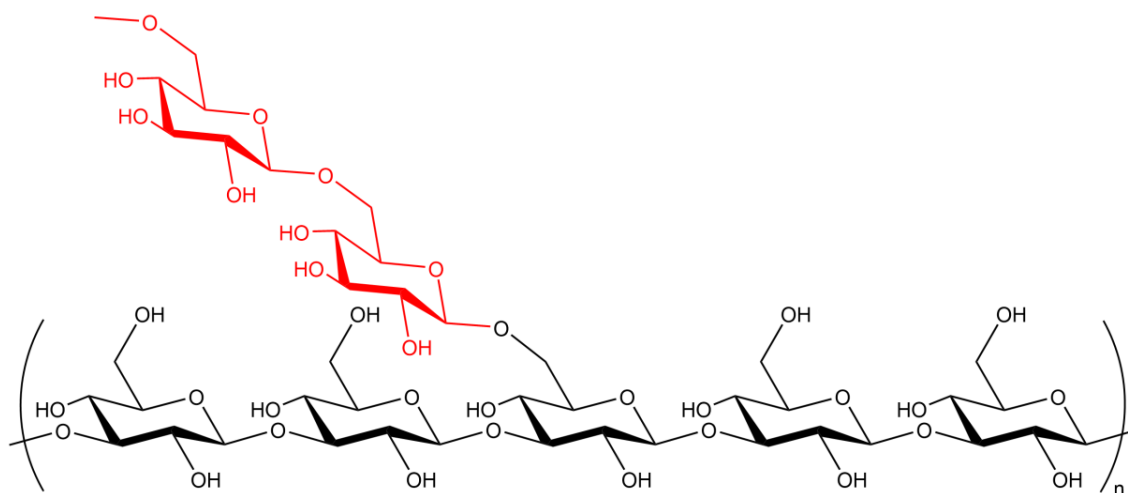


Figure 2.15 Structure of a β -1,3-glucan backbone with a β -1,6-glucan branch. The β -1,6-glucan is highlighted in red. Reproduced from Yu (Copyright 2021 Guoqiang Yu).⁶³

Serving as the main structural component, β -1,3-glucan is found to be an amorphous branched polymer with other cell wall components being covalently attached. The β -1,3-glucan is synthesized by a well-characterized plasma membrane-associated enzyme (β -1,3-glucan synthase) and extended into the extracellular space through vectorial synthesis (Figure 2.16).⁴² As with chitin, this glucan synthesis mode promotes the combination of new glucan chains within the cell wall space, facilitating the cell wall integration. The β -1,3-glucan synthase is also a prime target for antifungal agents due to its importance in cell wall biogenesis. Caspofungin, micafungin, and anidulafungin, β -1,3-glucan synthase inhibitors, have been applied for clinical treatment of aspergillosis and candidiasis by means of cell swelling and lysis.⁶⁴

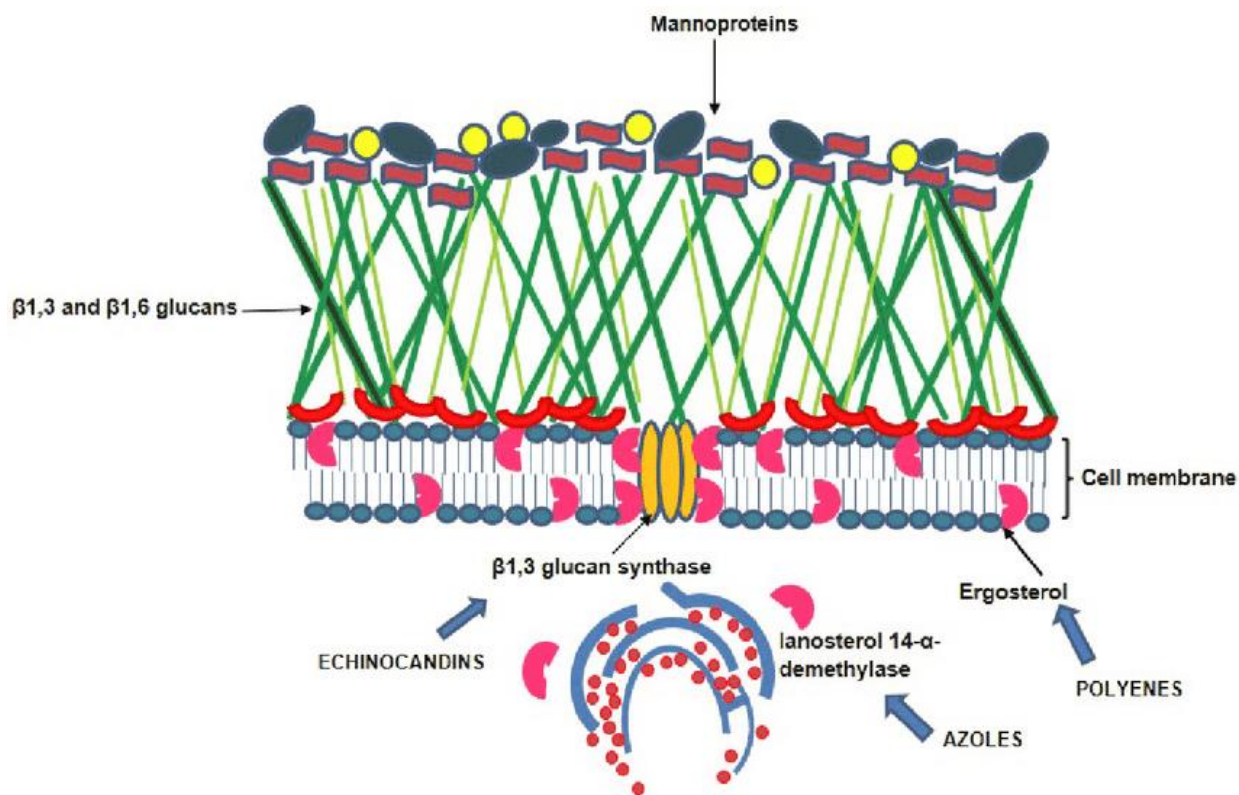


Figure 2.16 β -1,3-glucan and its synthesis in the fungal cell wall. Reproduced from Monteiro et al. (Copyright 2019 IntechOpen).⁶⁵

2.2.4 Glycoprotein

Proteins can be found in all fungal cell walls, and they are tightly linked in the chitin and glucan-based structural cell wall matrix.⁶⁶ Proteins account for approximately 15 to 50% of cell wall mass.⁴¹ Most fungal cell wall proteins are glycoproteins that have passed through the secretory pathway in transit to the cell wall. Glycoproteins are widely modified with N-linked and O-linked oligosaccharides in various fungal cell walls. In addition to these modifications, many cell wall proteins are produced as glycosylphosphatidylinositol (GPI) anchor proteins.⁴² The GPI anchor is added to select proteins that have special signal sequences and helps direct and localize these proteins to plasma membrane and cell wall space. Cell wall proteins function in cross-linking the

matrix together, mediating adhesion for cell migration and fusion, protecting the cell from other substances, and contributing to cell wall organization and biosynthesis.⁶⁷ Figure 2.17 depicts the dynamic process for fungal cell wall biosynthesis.

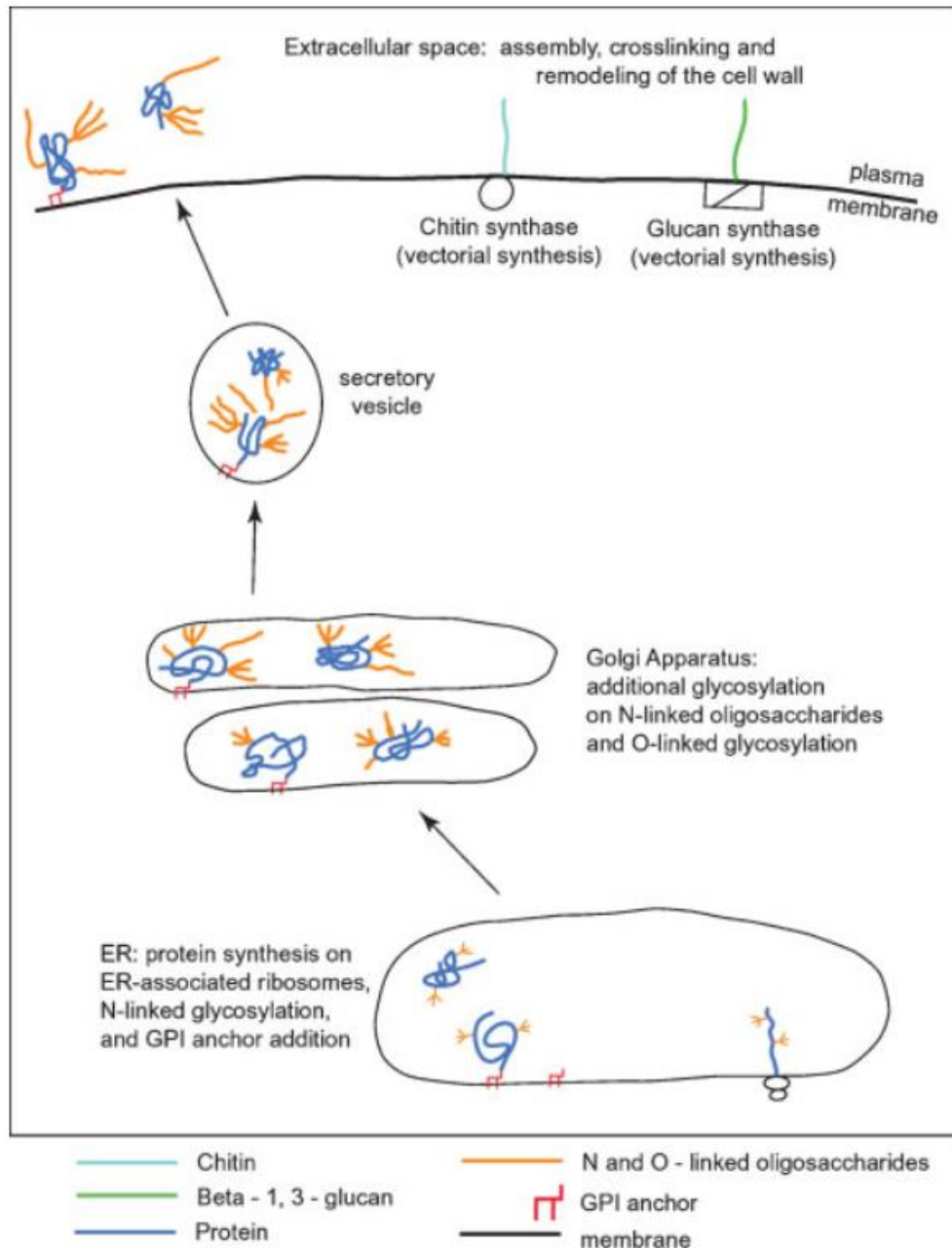


Figure 2.17 Fungal cell wall biosynthesis. Reproduced from Bowman et al. (Copyright 2006 Wiley).⁴¹

2.3 Poly(ether imide)

Poly(ether imide) (PEI) (Figure 2.18), polymerized from dianhydride and diamine monomers through polycondensation mechanism is an high-performance thermoplastic. Typically, PEI possess high thermal and mechanical properties (*e.g.*, Ultem[®] glass transition temperature = 217 °C, degradation temperature > 500 °C, tensile stress > 100 MPa, and Young's modulus > 2 GPa).⁶⁸⁻⁶⁹ Because of the excellent thermal and mechanical performance, PEI is widely used as matrix resins, adhesives, and coatings in different fields, including electronics, automotive, medical, and aerospace.⁷⁰⁻⁷²

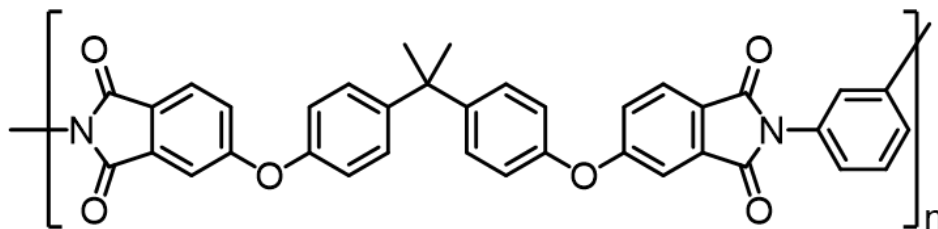


Figure 2.18 Chemical structure of Polyetherimide.

Currently, PEI is typically thermo-processed at high temperature (340 to 400 °C) to produce products with desired shapes (Figure 2.19). However, the high processing viscosity requires considerable energy consumption and therefore high energy expenditures.⁷³ In addition, the high processing temperature often leads to gradual oxidation of PEI, resulting in compromised properties.⁷¹ Therefore, there are strong demands of PEI modification to reduce the processing viscosity and temperature, and simultaneously maintain or improve the physical performance. Two major methods are proposed in the literature to improve the processibility of PEI, including polymer blending and oligomer engineering.^{72,74} Mixing PEI with flexible polymer additives (*e.g.*, polycarbonates⁷⁵⁻⁷⁶ and polyesters⁷⁷⁻⁷⁹) is a simple and economical way to reduce the melting temperature. However, the overall thermal and mechanical properties of the blends are usually

reduced due to the poor miscibility of polymers and intrinsically weaker thermal and mechanical properties of the additive polymers relative to PEI. Alternatively, PEI oligomers enhanced by terminal-functional groups possess both reduced processing viscosity and temperature, and maintain or even enhance the original performance. By oligomerization, the polymer chain entanglement is weakened which reduces the polymer melt viscosity. Below the processing temperature, the terminal groups on oligomers reestablish interpolymer interactions, such as hydrogen bonding⁷³ and ionic bonding,⁷² generating a stable supramolecular network. Incorporating crosslinkable end groups may further enhance the inter-polymer interactions through covalent crosslinks,⁸⁰⁻⁸³ forming a polymer with solvent resistance, in addition to other physical properties. Methods for reducing processing temperatures in the literature are provide in Figure 2.20.

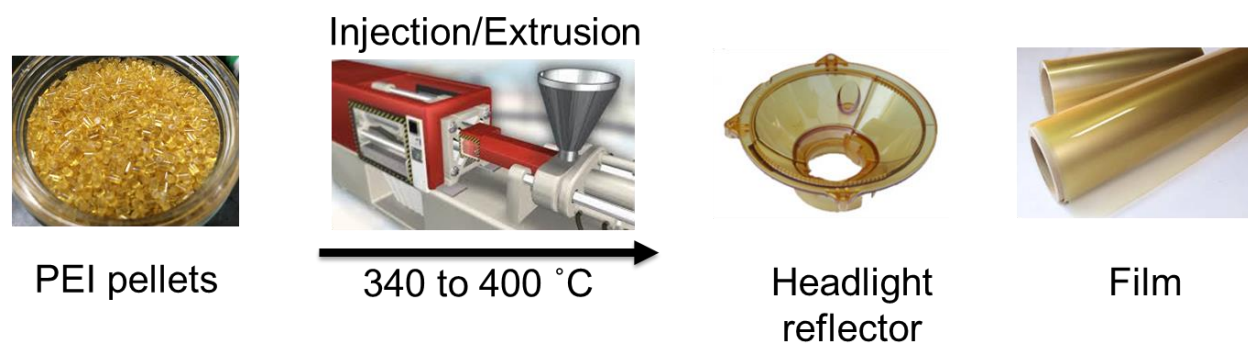


Figure 2.19 Industrial processing of PEI.

2.4 Polyethylene

Polyethylene (PE) is one of the most widely produced and utilized semicrystalline thermoplastics, synthesized from radical polymerization of ethylene, due to low production costs, good chemical resistance, high processability, flexibility, excellent electrical insulation, and transparency as thin films.⁸⁴⁻⁸⁷ PEs are commonly categorized by crystallinity which positively influence density and some physicochemical properties of PE.⁸⁸ Ultrahigh molecular weight polyethylene (UHMW), high-density polyethylene (HDPE), medium density polyethylene (MDPE), low-density polyethylene (LDPE), and linear low-density polyethylene (LLDPE) are the five primary categories with properties suitable for different applications. For example, UHMW has high-performance applications in areas such as medical devices and bullet proof vests.⁸⁹⁻⁹⁰ HDPE is more often used in construction, like the fabrication of drainpipes.⁹¹ LDPE, by contrast, is widely used in plastic packaging (grocery bags or plastic wrap) with good flexibility.⁹²⁻⁹³

PE is often exposed to complex environmental conditions during their lifespan.⁹⁴⁻⁹⁵ Ultra-violet (UV) light, thermal, mechanical, or chemical processes gradually compromise the polymer chain integrity, leading to material failures, through a process commonly termed as aging (Figure 2.21).⁹⁶⁻⁹⁸ Investigation of PE aging mechanisms has long interested academia for several reasons: 1) revealing the aging mechanism is helpful to the design of durable materials; 2) predict the lifetime of a material; and 3) understand the material behavior under specific conditions (*e.g.*, high temperatures, high humid, strong sunlight).⁹⁹⁻¹⁰⁰ In addition, the discovery of micro/nanoplastics (M/NPs) in the polar region in the recent year has further addressed the importance of studying aging.¹⁰¹⁻¹⁰² Valuable progress has been made in the M/NPs tracing, biological impact, polymer screening, and M/NPs imaging. Nonetheless, the understanding to the M/NPs formation mechanism remain shallow, primarily due to the insensitivity of the common technologies (FTIR,

Raman, SEM, and optical microscopes) to the minute physiochemical changes, or the incapability of capturing M/NPs and sampling them for analysis.¹⁰³⁻¹⁰⁶

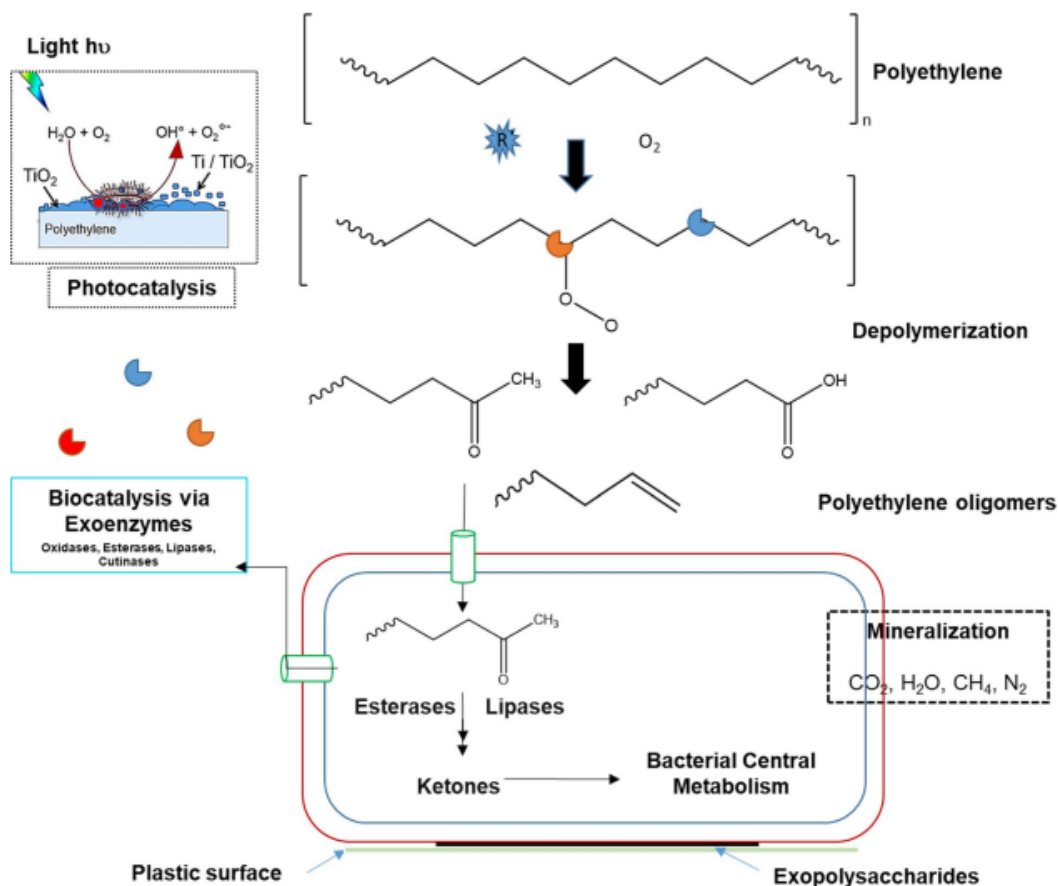


Figure 2.21 Schematic representation of polyethylene degradation. Reproduced from Ghatge et al. (Copyright 2020 Springer).¹⁰⁷

2.5 Polymer Adsorption

Adsorption is a surface process which causes the adhesion of atoms, ions, or molecules from a fluid bulk to a surface. Adsorption can be found at different interfaces including liquid-liquid, gas-liquid, solid-liquid, and gas-solid interfaces with a classification of chemisorption or physisorption.¹⁰⁸ Chemisorption is an irreversible process with chemical bonds formed and usually involves with chemical modification of the adherend.¹⁰⁹⁻¹¹⁰ Physisorption, however, is a reversible

process with weak physical interactions (van der Waals forces) and normally has no adherend change after desorption.¹¹¹⁻¹¹² Adsorption occurs in many systems, such as natural, physical, biological, and chemical systems. It has wide industrial applications in heterogeneous catalysts, synthetic resins, water purification, etc.¹¹³⁻¹¹⁴

Polymer adsorption usually forms irreversibly adsorbed layers on the solid substrate and the volume fraction occupied by polymers decrease with an increase of the distance from the surface (Figure 2.22A).¹¹⁵⁻¹¹⁷ However, a depletion layer can be formed close to the substrate surface when the interaction between the polymer and the substrate is less favorable than the interaction between solvent and the substrate, as shown in Figure 2.22B.¹¹⁸

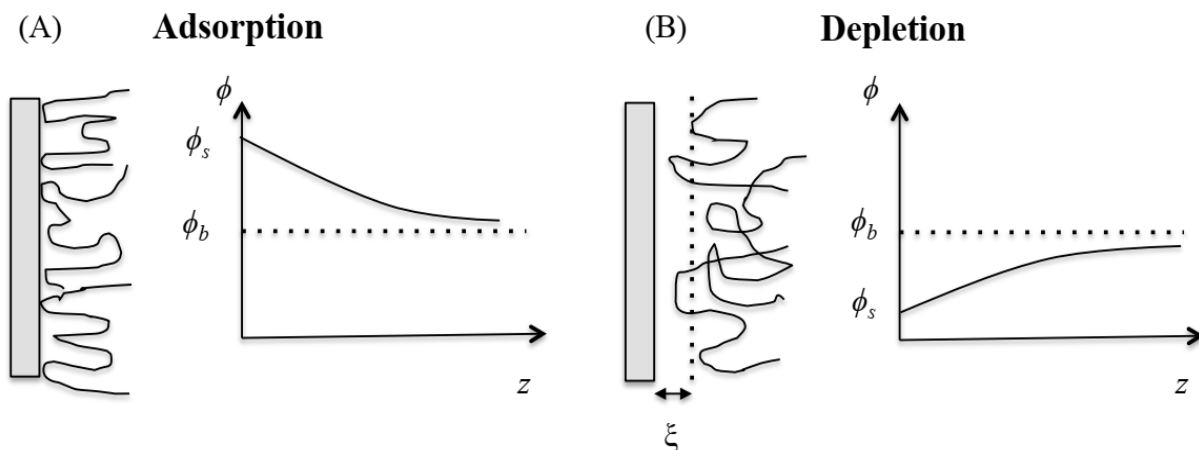


Figure 2.22 Polymer formation of (a) an adsorption layer and (b) a depletion layer at a solid substrate surface. ϕ , polymer volume fraction; z , distance from the substrate surface; ϕ_s , polymer volume fraction at the surface; ϕ_b , polymer volume fraction in the bulk solution. Reproduced from Zhang (Copyright 2014 Xiao Zhang).²⁴

A common model to describe the conformation of polymer adsorption onto a solid substrate is called the “loop-train-tail” model (Figure 2.23).¹¹⁹⁻¹²⁰ The polymer chain can be regarded as the integration of loops, trains, and tails onto the substrate. The amount of chain segments in contact

with the substrate, which can be called “trains” is small. Loops refer the internal chain segments that extended into the bulk system. Tails are the end chain segments with one contact point onto the substrate.

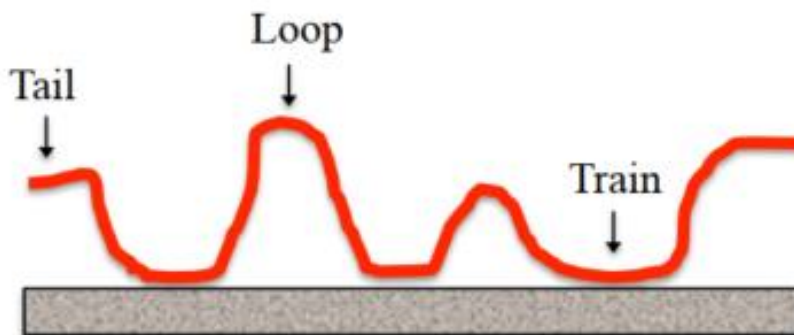


Figure 2.23 Conformation of an adsorbed neutral polymer chain. Reproduced from Zhang (Copyright 2014 Xiao Zhang).²⁴

2.6 QCM-D

Use of a quartz crystal microbalance with dissipation monitoring (QCM-D) enables real-time, label free measurements of molecular adsorption and/or interactions on various surfaces. Traditional quartz crystal microbalances (QCM) have been applied to analyze mass changes on rigid surfaces. QCM-D, based upon QCM, can not only quantify the adsorbed masses, measured as changes in frequency of the quartz crystal, but obtain novel insights regarding structural (viscoelastic) properties of adsorbed layers, provided by the dissipation parameter (D).¹²¹ Due to these unique features, QCM-D can be used to study various processes including the adsorption/desorption, binding, degradation, and swelling in research areas such as drug discovery, biomaterials, nanotechnology, biofuels, environmental science, etc.¹²²⁻¹³⁰

The QCM technique relies on a voltage being applied to a quartz crystal that can cause the quartz crystal to oscillate at a specific frequency (Figure 2.24A and B). The thin film coated on

the crystal surface could be treated as part of the QCM crystal and mass of this attached film leads to changes in frequency of the oscillating crystal through the Sauerbrey relationship from Equation 2.1.¹³¹

$$\Delta m = -c \frac{\Delta f}{n} \quad (2.1)$$

The constant C is 0.177 mg m⁻² Hz⁻¹ for a 5 MHz crystal and n is the overtone number.

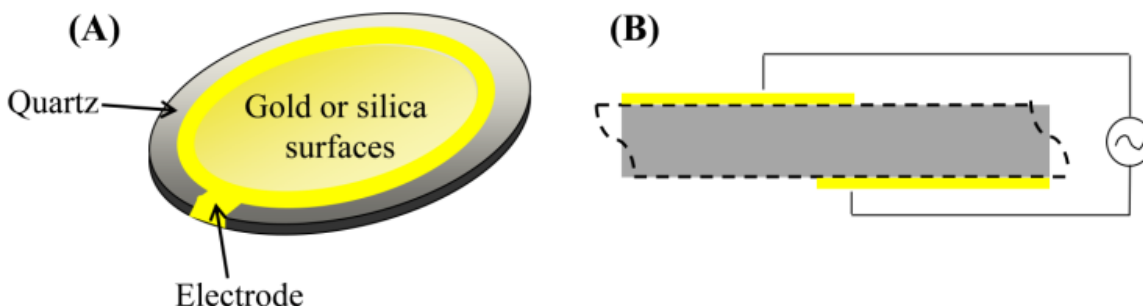


Figure 2.24 Representative profile of (A) a QCM crystal and (B) a QCM crystal oscillating in a shear thickness mode in an alternating electric field. Reproduced from Wang (Copyright 2014 Chao Wang).³⁴

The Sauerbrey relation is only valid for rigid, evenly distributed, and sufficiently thin adsorbed layers. However, for soft or viscoelastic films that cannot fully couple to the oscillatory motion of the QCM crystal or dissipate the oscillation, the Sauerbrey relationship underestimates the mass of a viscoelastic film. Therefore, a new analytical method is needed to fully characterize such films. QCM with dissipation monitoring (QCM-D) can be applied to study viscoelastic films by measuring the dissipation when the driving voltage to the crystal is shut off and the energy of the oscillating crystal dissipates from the system.¹³²⁻¹³³ This procedure can be repeated over 200 times per second, which gives QCM-D great sensitivity and high resolution. The dissipation (D)

is defined as the ratio between the energy dissipated ($E_{\text{dissipated}}$) and the energy stored (E_{stored}) during one oscillation cycle (Equation 2.2).

$$D = \frac{E_{\text{dissipated}}}{E_{\text{stored}}} \quad (2.2)$$

Dissipation measurements can qualify the structural properties of adsorbed films so that different adsorbed materials can be compared and checked if the Sauerbrey relation will accurately estimate the adsorbed mass or not. For a rigid film, energy dissipates slowly, and D is relatively small, while energy dissipates quickly, and D is large for a soft film (Figure 2.25).

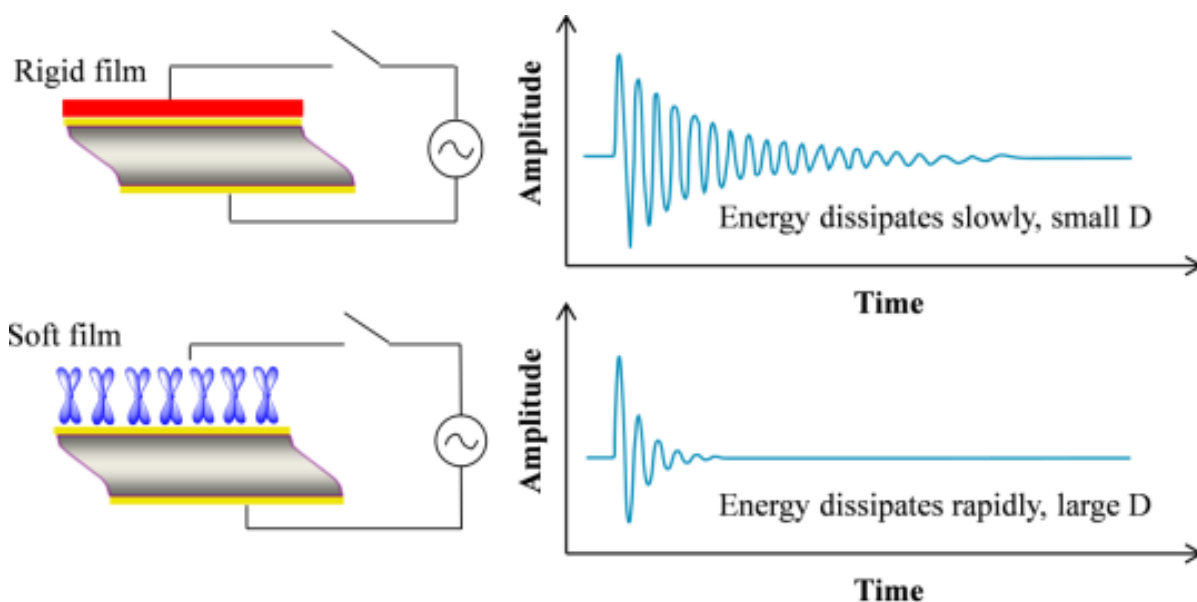


Figure 2.25 Demonstration of the energy dissipation after the power is turned off in a QCM-D. Reproduced from Wang (Copyright 2014 Chao Wang).³⁴

Furthermore, by combining frequency (f) and dissipation (D) measurements from multiple harmonics (overtones) and applying simulations using a Voigt-based viscoelastic model from Qsense Dfind software, the QCM-D technique enables quantitative analysis of the thickness (d), shear elastic modulus (μ), and viscosity (η) of the soft and dissipative adsorbed films. These unknown parameters can be obtained by fitting experimental frequency and dissipation data based

upon two or more overtones.^{130, 134-135} A schematic depiction of the parameters necessary for the Voigt-based viscoelastic model are shown in Figure 2.26.

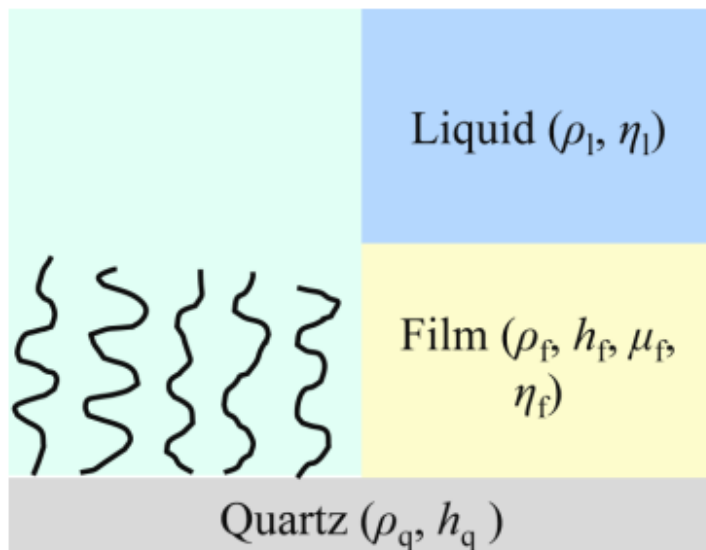


Figure 2.26 Representative depiction of the fitting parameters generated by the Voigt-based viscoelastic modeling system in a QCM-D. Reproduced from Hook et al. (Copyright 2001 American Chemistry Society).¹³⁶

2.7 References

1. Cosgrove, D. J., Growth of the plant cell wall. *Nat. Rev. Mol. Cell. Biol.* **2005**, *6*, 850-861.
2. Cosgrove, D. J., Plant cell wall extensibility: connecting plant cell growth with cell wall structure, mechanics, and the action of wall-modifying enzymes. *J. Exp. Bot.* **2016**, *67*, 463-476.
3. Lampugnani, E. R.; Khan, G. A.; Somssich, M.; Persson, S., Building a plant cell wall at a glance. *J. Cell Sci.* **2018**, *131*, 1-6.
4. Somerville, C.; Bauer, S.; Brininstool, G.; Facette, M.; Hamann, T.; Milne, J.; Osborne, E.; Paredez, A.; Persson, S.; Raab, T.; Vorwerk, S.; Youngs, H., Toward a systems approach to understanding plant cell walls. *Science* **2004**, *306*, 2206-2211.

5. Cosgrove, D. J., Wall structure and wall loosening. A look backwards and forwards. *Plant Physiol.* **2001**, *125*, 131-134.
6. Timell, T. E., Recent progress in the chemistry of wood hemicelluloses. *Wood Sci. Technol.* **1967**, *1*, 45-70.
7. Palin, R. J. A comparison of cell wall properties of *Arabidopsis thaliana*. Ph.D. Dissertation, University of Birmingham, United Kingdom, 2011.
8. Bailey, R. Cell Wall Structure and Function. <https://www.thoughtco.com/cell-wall-373613> (accessed 2021-10-21).
9. Jarvis, M. C.; Briggs, S. P. H.; Knox, J. P., Intercellular adhesion and cell separation in plants. *Plant Cell Environ.* **2003**, *26*, 977-989.
10. Bidlack, J. In *Molecular structure and component integration of secondary cell walls in plants*, Proc. Okla. Acad. Sci., 1992; pp 51-56.
11. Keegstra, K., Plant cell walls. *Plant Physiol.* **2010**, *154*, 483-486.
12. Barros, J.; Serk, H.; Granlund, I.; Pesquet, E., The cell biology of lignification in higher plants. *Ann. Bot.* **2015**, *115*, 1053-1074.
13. Complex Carbohydrate Research Center. <https://glygen.ccrcc.uga.edu/ccrc/mao/intro/outline.htm> (accessed 2021-10-21).
14. Young, R. A.; Rowell, R. M., *Cellulose: structure, modification, and hydrolysis*. John Wiley & Sons: 1986.
15. Klemm, D.; Heublein, B.; Fink, H. P.; Bohn, A., Cellulose: fascinating biopolymer and sustainable raw material. *Angew. Chem. Int. Ed. Engl.* **2005**, *44*, 3358-3393.
16. Habibi, Y.; Lucia, L. A.; Rojas, O. J., Cellulose nanocrystals: chemistry, self-assembly, and applications. *Chem. Rev.* **2010**, *110*, 3479-3500.

17. Habibi, Y.; Mahrouz, M.; Vignon, M. R., Microfibrillated cellulose from the peel of prickly pear fruits. *Food Chem.* **2009**, *115*, 423-429.
18. Marchessault, R. H.; Sundararajan, P. R., Cellulose. In *The polysaccharides*, Elsevier: 1983; pp 11-95.
19. Updegraff, D. M., Semimicro determination of cellulose in biological materials. *Anal. Biochem.* **1969**, *32*, 420-424.
20. Potthast, A.; Rosenau, T.; Sixta, H.; Kosma, P., Degradation of cellulosic materials by heating in DMAc/LiCl. *Tetrahedron Lett.* **2002**, *43*, 7757-7759.
21. Heinze, T.; Liebert, T., Unconventional methods in cellulose functionalization. *Prog. Polym. Sci.* **2001**, *26*, 1689-1762.
22. Welton, T., Room-Temperature Ionic Liquids. Solvents for Synthesis and Catalysis. *Chem. Rev.* **1999**, *99*, 2071-2084.
23. O'sullivan, A. C., Cellulose: the structure slowly unravels. *Cellulose* **1997**, *4*, 173-207.
24. Zhang, X. Adsorption of biomacromolecules onto polysaccharide surfaces. Ph.D. Dissertation, Virginia Tech, Blacksburg, VA, 2014.
25. Wilder, B. M.; Albersheim, P., The Structure of Plant Cell Walls: IV. A Structural Comparison of the Wall Hemicellulose of Cell Suspension Cultures of Sycamore (*Acer PseudoPlatanus*) and of Red Kidney Bean (*Phaseolus Vulgaris*). *Plant Physiol.* **1973**, *51*, 889-893.
26. He, C.; Ma, J.; Wang, L., A hemicellulose-bound form of silicon with potential to improve the mechanical properties and regeneration of the cell wall of rice. *New Phytol.* **2015**, *206*, 1051-1062.
27. Haigler, C. H.; Brown, R. M., Transport of rosettes from the Golgi apparatus to the plasma membrane in isolated mesophyll cells of *Zinnia elegans* during differentiation to tracheary elements in suspension culture. *Protoplasma* **1986**, *134*, 111-120.

28. Peng, P.; She, D., Isolation, structural characterization, and potential applications of hemicelluloses from bamboo: a review. *Carbohydr. Polym.* **2014**, *112*, 701-720.
29. Li, Z.; Pan, X., Strategies to modify physicochemical properties of hemicelluloses from biorefinery and paper industry for packaging material. *Rev. Environ. Sci. Biotechnol.* **2018**, *17*, 47-69.
30. Liu, Z.; Fatehi, P.; Sadeghi, S.; Ni, Y., Application of hemicelluloses precipitated via ethanol treatment of pre-hydrolysis liquor in high-yield pulp. *Bioresour. Technol.* **2011**, *102*, 9613-9618.
31. Scheller, H. V.; Ulvskov, P., Hemicelluloses. *Annu. Rev. Plant Biol.* **2010**, *61*, 263-289.
32. Lopez, M.; Bizot, H.; Chambat, G.; Marais, M. F.; Zykwincka, A.; Ralet, M. C.; Driguez, H.; Buleon, A., Enthalpic studies of xyloglucan-cellulose interactions. *Biomacromolecules* **2010**, *11*, 1417-1428.
33. Hoch, G., Cell wall hemicelluloses as mobile carbon stores in non-reproductive plant tissues. *Funct. Ecol.* **2007**, *21*, 823-834.
34. Wang, C. Renewable natural polymer thin films and their interactions with biomacromolecules. Ph.D. Dissertation, Virginia Tech., Blacksburg, VA, 2014.
35. Wood, P. J., Relationships between solution properties of cereal beta-glucans and physiological effects-a review. *Trends Food Sci. Technol.* **2004**, *15*, 313-320.
36. Buckeridge, M. C.; Rayon, C.; Urbanowicz, B.; Tiné, M. A. S.; Carpita, N. C., Mixed linkage (1→3),(1→4)-β-d-glucans of grasses. *Cereal Chem.* **2004**, *81*, 115-127.
37. Boerjan, W.; Ralph, J.; Baucher, M., Lignin biosynthesis. *Annu. Rev. Plant Biol.* **2003**, *54*, 519-546.

38. Xiong, W.; Qiu, X.; Zhong, R.; Yang, D., Characterization of the adsorption properties of a phosphorylated kraft lignin-based polymer at the solid/liquid interface by the QCM-D approach. *Holzforschung* **2016**, *70*, 937-945.
39. Vanholme, R.; Ralph, J.; Akiyama, T.; Lu, F.; Pazo, J. R.; Kim, H.; Christensen, J. H.; Van Reusel, B.; Storme, V.; De Rycke, R.; Rohde, A.; Morreel, K.; Boerjan, W., Engineering traditional monolignols out of lignin by concomitant up-regulation of F5H1 and down-regulation of COMT in Arabidopsis. *Plant J.* **2010**, *64*, 885-897.
40. Zakzeski, J.; Bruijninx, P. C.; Jongerius, A. L.; Weckhuysen, B. M., The catalytic valorization of lignin for the production of renewable chemicals. *Chem. Rev.* **2010**, *110*, 3552-3599.
41. Bowman, S. M.; Free, S. J., The structure and synthesis of the fungal cell wall. *Bioessays* **2006**, *28*, 799-808.
42. Free, S. J., Fungal cell wall organization and biosynthesis. *Adv. Genet.* **2013**, *81*, 33-82.
43. Kang, X.; Kirui, A.; Muszynski, A.; Widanage, M. C. D.; Chen, A.; Azadi, P.; Wang, P.; Mentink-Vigier, F.; Wang, T., Molecular architecture of fungal cell walls revealed by solid-state NMR. *Nat. Commun.* **2018**, *9*, 2747-2758.
44. Roncero, C., The genetic complexity of chitin synthesis in fungi. *Curr. Genet.* **2002**, *41*, 367-378.
45. Ruiz-Herrera, J.; Gonzalez-Prieto, J. M.; Ruiz-Medrano, R., Evolution and phylogenetic relationships of chitin synthases from yeasts and fungi. *FEMS Yeast Res.* **2002**, *1*, 247-256.
46. Gow, N. A. R.; Latge, J. P.; Munro, C. A., The Fungal Cell Wall: Structure, Biosynthesis, and Function. *Microbiol. Spectr.* **2017**, *5*, FUNK-0035-2016.
47. Consortium, M. S. G. E. a. R., Fungal Cell Structure and Targets. 2018.
48. Minke, R.; Blackwell, J., The structure of alpha-chitin. *J. Mol. Biol.* **1978**, *120*, 167-181.

49. Tharanathan, R. N.; Kittur, F. S., Chitin-The undisputed biomolecule of great potential. *Crit. Rev. Food Sci. Nutr.* **2003**, *43*, 61-87.
50. Klis, F. M., Review: cell wall assembly in yeast. *Yeast* **1994**, *10*, 851-869.
51. Bartnicki-Garcia, S., Cell wall chemistry, morphogenesis, and taxonomy of fungi. *Annu. Rev. Microbiol.* **1968**, *22*, 87-108.
52. Saito, Y.; Okano, T.; Gaill, F.; Chanzy, H.; Putaux, J. L., Structural data on the intra-crystalline swelling of beta-chitin. *Int. J. Biol. Macromol.* **2000**, *28*, 81-88.
53. Merzendorfer, H., The cellular basis of chitin synthesis in fungi and insects: common principles and differences. *Eur. J. Cell Biol.* **2011**, *90*, 759-769.
54. Bulawa, C. E., Genetics and molecular biology of chitin synthesis in fungi. *Annu. Rev. Microbiol.* **1993**, *47*, 505-534.
55. Specht, C. A.; Liu, Y. L.; Robbins, P. W.; Bulawa, C. E.; Iartchouk, N.; Winter, K. R.; Riggle, P. J.; Rhodes, J. C.; Dodge, C. L.; Culp, D. W., The *chsD* and *chsE* Genes of *Aspergillus nidulans* and Their Roles in Chitin Synthesis. *Fungal Genet. Biol.* **1996**, *20*, 153-167.
56. Ruiz-Herrera, J.; San-Blas, G., Chitin synthesis as a target for antifungal drugs. *Curr. Drug Targets Infect. Disord.* **2003**, *3*, 77-91.
57. Rinaudo, M., Chitin and chitosan: Properties and applications. *Prog. Polym. Sci.* **2006**, *31*, 603-632.
58. Kapteyn, J. C.; Van Den Ende, H.; Klis, F. M., The contribution of cell wall proteins to the organization of the yeast cell wall. *Biochim. Biophys. Acta* **1999**, *1426*, 373-83.
59. Brown, G. D.; Gordon, S., Fungal beta-glucans and mammalian immunity. *Immunity* **2003**, *19*, 311-315.

60. Grün, C. H.; Hochstenbach, F.; Humbel, B. M.; Verkleij, A. J.; Sietsma, J. H.; Klis, F. M.; Kamerling, J. P.; Vliegthart, J. F., The structure of cell wall α -glucan from fission yeast. *Glycobiology* **2004**, *15*, 245-257.
61. Chen, J.; Seviour, R., Medicinal importance of fungal beta-(1->3), (1->6)-glucans. *Mycol. Res.* **2007**, *111*, 635-652.
62. Camilli, G.; Tabouret, G.; Quintin, J., The Complexity of Fungal beta-Glucan in Health and Disease: Effects on the Mononuclear Phagocyte System. *Front Immunol.* **2018**, *9*, 673-681.
63. Yu, G. Interactions of Chitin and Lignin Thin Films with Other Molecules. Ph.D. Dissertation, Virginia Tech, Blacksburg, VA, 2021.
64. Chen, S.; Slavin, M. A.; Sorrell, T. C., Echinocandin antifungal drugs in fungal infections: a comparison. *Drugs* **2011**, *71*, 11-41.
65. Monteiro, C. D. A. Phytochemicals and Their Antifungal Potential against Pathogenic Yeasts. <https://www.intechopen.com/chapters/67874> (accessed 2021-10-21).
66. Wright, S. F.; Upadhyaya, A., Extraction of an abundant and unusual protein from soil and comparison with hyphal protein of arbuscular mycorrhizal fungi. *Soil Sci.* **1996**, *161*, 575-586.
67. Nevalainen, K. M.; Te'o, V. S.; Bergquist, P. L., Heterologous protein expression in filamentous fungi. *Trends Biotechnol.* **2005**, *23*, 468-474.
68. Johnson, R. O.; Burlhis, H. S. In *Polyetherimide: A new high-performance thermoplastic resin*, Journal of Polymer Science: Polymer Symposia, Wiley Online Library: 1983; pp 129-143.
69. Eastmond, G. C.; Paprotny, J., Scope in the synthesis and properties of poly(ether imide)s. *React. Funct. Polym.* **1996**, *30*, 27-41.

70. Wang, G.; Weng, Y.; Chu, D.; Xie, D.; Chen, R., Preparation of alkaline anion exchange membranes based on functional poly (ether-imide) polymers for potential fuel cell applications. *J. Membr. Sci.* **2009**, *326*, 4-8.
71. Xu, Z.; Croft, Z. L.; Guo, D.; Cao, K.; Liu, G., Recent development of polyimides: Synthesis, processing, and application in gas separation. *J. Polym. Sci.* **2021**, *59*, 943-962.
72. Cao, K.; Guo, Y.; Zhang, M.; Arrington, C. B.; Long, T. E.; Odle, R. R.; Liu, G., Mechanically strong, thermally stable, and flame retardant poly (ether imide) terminated with phosphonium bromide. *Macromolecules* **2019**, *52*, 7361-7368.
73. Cao, K.; Liu, G., Low-molecular-weight, high-mechanical-strength, and solution-processable telechelic poly (ether imide) end-capped with ureidopyrimidinone. *Macromolecules* **2017**, *50*, 2016-2023.
74. Cao, K.; Serrano, J. M.; Liu, T.; Stovall, B. J.; Xu, Z.; Arrington, C. B.; Long, T. E.; Odle, R. R.; Liu, G., Impact of metal cations on the thermal, mechanical, and rheological properties of telechelic sulfonated polyetherimides. *Polym. Chem.* **2020**, *11*, 393-400.
75. Ramiro, J.; Eguiazabal, J. I.; Nazabal, J., Phase structure and mechanical properties of blends of poly(ether imide) and bisphenol A polycarbonate. *Polym. J.* **2004**, *36*, 705-715.
76. Blanco, I.; Cicala, G.; Ognibene, G.; Rapisarda, M.; Recca, A., Thermal properties of polyetherimide/polycarbonate blends for advanced applications. *Polym. Degrad. Stab.* **2018**, *154*, 234-238.
77. Lin, C. H.; Wang, C. S., Miscibility of poly (etherimide) and poly (butylene naphthalate) blends. *Polym. Bull.* **2001**, *46*, 191-196.

78. Su, C. C.; Shih, C. K., Miscibility and transesterification in ternary blends of poly(ethylene naphthalate)/poly(pentamethylene terephthalate)/poly(ether imide). *J. Appl. Polym. Sci.* **2006**, *100*, 3840-3849.
79. Ramiro, J.; Eguiazabal, J. I.; Nazabal, J., Synergistic mechanical behaviour and improved processability of poly (ether imide) by blending with poly (trimethylene terephthalate). *Polym. Adv. Technol.* **2003**, *14*, 129-136.
80. Yoo, T.; Kim, K.; Han, P.; Jang, W.; Han, H., Norbornene end-capped polyimide for low CTE and low residual stress with changes in the diamine linkages. *Macromol. Res.* **2015**, *23*, 776-786.
81. Mushtaq, N.; Chen, G. F.; Sidra, L. R.; Liu, Y.; Fang, X. Z., Synthesis and crosslinking study of isomeric poly(thioether ether imide)s containing pendant nitrile and terminal phthalonitrile groups. *Polym. Chem.* **2016**, *7*, 7427-7435.
82. Gong, C.; Luo, Q.; Li, Y.; Giotto, M.; Cipollini, N. E.; Yang, Z.; Weiss, R. A.; Scola, D. A., Free radical initiated low temperature crosslinking of phenylethynyl (PE) end-capped oligomides. *J. Polym. Sci., Part A: Polym. Chem.* **2010**, *48*, 3950-3963.
83. Takeichi, T.; Tanikawa, M., Internal acetylene unit linked para to the aromatic ring as a crosslink site for polyimide. *J. Polym. Sci. Part A: Polym. Chem.* **1996**, *34*, 2205-2211.
84. Geyer, R.; Jambeck, J. R.; Law, K. L., Production, use, and fate of all plastics ever made. *Sci. Adv.* **2017**, *3*, e1700782.
85. Ronca, S., Polyethylene. In *Brydson's plastics materials*, Elsevier: 2017; pp 247-278.
86. Aggarwal, S. L.; Sweeting, O. J., Polyethylene : Preparation, Structure, and Properties. *Chem. Rev.* **1957**, *57*, 665-742.

87. Xie, T. Y.; Mcauley, K. B.; Hsu, J. C. C.; Bacon, D. W., Gas-Phase Ethylene Polymerization - Production Processes, Polymer Properties, and Reactor Modeling. *Ind. Eng. Chem. Res.* **1994**, *33*, 449-479.
88. Peacock, A. J., The chemistry of polyethylene (Reprinted from Handbook Polyethylene: Structures, properties, and applications, pg 375-414, 2000). *J. Macromol. Sci. Part C Polym. Rev.* **2001**, *41*, 285-323.
89. Muratoglu, O. K.; Bragdon, C. R.; O'Connor, D. O.; Jasty, M.; Harris, W. H.; Gul, R.; McGarry, F., Unified wear model for highly crosslinked ultra-high molecular weight polyethylenes (UHMWPE). *Biomaterials* **1999**, *20*, 1463-1470.
90. Macuvele, D. L. P.; Nones, J.; Matsinhe, J. V.; Lima, M. M.; Soares, C.; Fiori, M. A.; Riella, H. G., Advances in ultra high molecular weight polyethylene/hydroxyapatite composites for biomedical applications: A brief review. *Mater. Sci. Eng.* **2017**, *76*, 1248-1262.
91. Wu, S.; Zhang, J.; Xu, X., Studies on high density polyethylene (HDPE) functionalized by ultraviolet irradiation and its application. *Polym. Int.* **2003**, *52*, 1527-1530.
92. Shemesh, R.; Krepker, M.; Goldman, D.; Danin-Poleg, Y.; Kashi, Y.; Nitzan, N.; Vaxman, A.; Segal, E., Antibacterial and antifungal LDPE films for active packaging. *Polym. Adv. Technol.* **2015**, *26*, 110-116.
93. Piergiovanni, L.; Limbo, S., Plastic packaging materials. In *Food packaging materials*, Springer: 2016; pp 33-49.
94. Lu, X. H.; Isacson, U., Artificial aging of polymer modified bitumens. *J. Appl. Polym. Sci.* **2000**, *76*, 1811-1824.

95. Burgess, S. K.; Mubarak, C. R.; Kriegel, R. M.; Koros, W. J., Physical Aging in Amorphous Poly(ethylene furanoate): Enthalpic Recovery, Density, and Oxygen Transport Considerations. *J. Polym. Sci. B Polym. Phys.* **2015**, *53*, 389-399.
96. Rimnac, C. M.; Klein, R. W.; Betts, F.; Wright, T. M., Post-irradiation aging of ultra-high molecular weight polyethylene. *J. Bone Joint Surg. Am.* **1994**, *76*, 1052-1056.
97. Jones, J. P.; Llewellyn, J. P.; Lewis, T. J., The contribution of field-induced morphological change to the electrical aging and breakdown of polyethylene. *IEEE Trans. Dielectr. Electr. Insul.* **2005**, *12*, 951-966.
98. Fanconi, B. M., Chain Scission and Mechanical Failure of Polyethylene. *J. Appl. Phys.* **1983**, *54*, 5577-5582.
99. Tian, L.; Chen, Q.; Jiang, W.; Wang, L.; Xie, H.; Kalogerakis, N.; Ma, Y.; Ji, R., A carbon-14 radiotracer-based study on the phototransformation of polystyrene nanoplastics in water versus in air. *Environ. Sci. Nano* **2019**, *6*, 2907-2917.
100. Zhu, L.; Zhao, S.; Bittar, T. B.; Stubbins, A.; Li, D., Photochemical dissolution of buoyant microplastics to dissolved organic carbon: Rates and microbial impacts. *J. Hazard Mater.* **2020**, *383*, 121065.
101. Andrady, A. L., The plastic in microplastics: A review. *Mar. Pollut. Bull.* **2017**, *119*, 12-22.
102. El Hadri, H.; Gigault, J.; Maxit, B.; Grassl, B.; Reynaud, S., Nanoplastic from mechanically degraded primary and secondary microplastics for environmental assessments. *NanoImpact* **2020**, *17*, 100206.
103. Phuong, N. N.; Zalouk-Vergnoux, A.; Poirier, L.; Kamari, A.; Châtel, A.; Mouneyrac, C.; Lagarde, F., Is there any consistency between the microplastics found in the field and those used in laboratory experiments? *Environ. Pollut.* **2016**, *211*, 111-123.

104. Xu, J. L.; Thomas, K. V.; Luo, Z.; Gowen, A. A., FTIR and Raman imaging for microplastics analysis: State of the art, challenges and prospects. *Trends Analyt. Chem.* **2019**, *119*, 115629.
105. Dehaut, A.; Hermabessiere, L.; Duflos, G., Current frontiers and recommendations for the study of microplastics in seafood. *Trends Analyt. Chem.* **2019**, *116*, 346-359.
106. Zhou, X. X.; Hao, L. T.; Wang, H. Y.; Li, Y. J.; Liu, J. F., Cloud-Point Extraction Combined with Thermal Degradation for Nanoplastic Analysis Using Pyrolysis Gas Chromatography-Mass Spectrometry. *Anal. Chem.* **2019**, *91*, 1785-1790.
107. Ghatge, S.; Yang, Y.; Ahn, J.-H.; Hur, H.-G., Biodegradation of polyethylene: a brief review. *Appl Biol Chem* **2020**, *63*, 1-14.
108. Lavrich, D. J.; Wetterer, S. M.; Bernasek, S. L.; Scoles, G., Physisorption and Chemisorption of Alkanethiols and Alkyl Sulfides on Au(111). *J. Phys. Chem. B* **1998**, *102*, 3456-3465.
109. Lv, C.; Xue, Q.; Xia, D.; Ma, M.; Xie, J.; Chen, H., Effect of chemisorption on the interfacial bonding characteristics of graphene–polymer composites. *J. Phys. Chem. C* **2010**, *114*, 6588-6594.
110. Lv, C.; Xue, Q.; Xia, D.; Ma, M., Effect of chemisorption structure on the interfacial bonding characteristics of graphene–polymer composites. *Appl. Surf. Sci.* **2012**, *258*, 2077-2082.
111. Chung, T. C. M.; Jeong, Y.; Chen, Q.; Kleinhammes, A.; Wu, Y., Synthesis of microporous boron-substituted carbon (B/C) materials using polymeric precursors for hydrogen physisorption. *J. Am. Chem. Soc.* **2008**, *130*, 6668-6669.
112. Beyer, D.; Bohanon, T. M.; Knoll, W.; Ringsdorf, H.; Elender, G.; Sackmann, E., Surface modification via reactive polymer interlayers. *Langmuir* **1996**, *12*, 2514-2518.
113. Ihsanullah; Abbas, A.; Al-Amer, A. M.; Laoui, T.; Al-Marri, M. J.; Nasser, M. S.; Khraisheh, M.; Atieh, M. A., Heavy metal removal from aqueous solution by advanced carbon nanotubes: Critical review of adsorption applications. *Sep Purif Technol* **2016**, *157*, 141-161.

114. Xu, J.; Cao, Z.; Zhang, Y.; Yuan, Z.; Lou, Z.; Xu, X.; Wang, X., A review of functionalized carbon nanotubes and graphene for heavy metal adsorption from water: Preparation, application, and mechanism. *Chemosphere* **2018**, *195*, 351-364.
115. de Gennes, P. G., Polymers at an interface; a simplified view. *Adv. Colloid Interface Sci.* **1987**, *27*, 189-209.
116. Douglas, J. F.; Johnson, H. E.; Granick, S., A simple kinetic model of polymer adsorption and desorption. *Science* **1993**, *262*, 2010-2012.
117. Gregory, J., Polymer Adsorption and Flocculation in Sheared Suspensions. *Colloids Surf.* **1988**, *31*, 231-253.
118. de Gennes, P. G., Polymer solutions near an interface. 1. Adsorption and depletion layers. *Macromolecules* **1981**, *14*, 1637-1644.
119. Welch, D.; Lettinga, M. P.; Ripoll, M.; Dogic, Z.; Vliegenthart, G. A., Trains, tails and loops of partially adsorbed semi-flexible filaments. *Soft Matter* **2015**, *11*, 7507-7514.
120. Scheutjens, J. M. H. M.; Fleer, G. J., *J. Phys. Chem.* **1980**, *84*, 178-190.
121. Irwin, E. F.; Ho, J. E.; Kane, S. R.; Healy, K. E., Analysis of interpenetrating polymer networks via quartz crystal microbalance with dissipation monitoring. *Langmuir* **2005**, *21*, 5529-5536.
122. Chen, Q.; Xu, S.; Liu, Q.; Masliyah, J.; Xu, Z., QCM-D study of nanoparticle interactions. *Adv. Colloid Interface Sci.* **2016**, *233*, 94-114.
123. Dixon, M. C., Quartz crystal microbalance with dissipation monitoring: enabling real-time characterization of biological materials and their interactions. *J. Biomol. Tech.* **2008**, *19*, 151-158.

124. Nileback, E.; Feuz, L.; Uddenberg, H.; Valiokas, R.; Svedhem, S., Characterization and application of a surface modification designed for QCM-D studies of biotinylated biomolecules. *Biosens. Bioelectron.* **2011**, *28*, 407-413.
125. Edvardsson, M.; Svedhem, S.; Wang, G.; Richter, R.; Rodahl, M.; Kasemo, B., QCM-D and reflectometry instrument: applications to supported lipid structures and their biomolecular interactions. *Anal. Chem.* **2009**, *81*, 349-361.
126. Tammelin, T.; Saarinen, T.; Osterberg, M.; Laine, J., Preparation of Langmuir/Blodgett-cellulose surfaces by using horizontal dipping procedure. Application for polyelectrolyte adsorption studies performed with QCM-D. *Cellulose* **2006**, *13*, 519-535.
127. Ahola, S.; Österberg, M.; Laine, J., Cellulose nanofibrils-adsorption with poly (amideamine) epichlorohydrin studied by QCM-D and application as a paper strength additive. *Cellulose* **2008**, *15*, 303-314.
128. Richter, R. P.; Brisson, A., QCM-D on mica for parallel QCM-D-AFM studies. *Langmuir* **2004**, *20*, 4609-4613.
129. Tagaya, M., In situ QCM-D study of nano-bio interfaces with enhanced biocompatibility. *Polym. J.* **2015**, *47*, 599-608.
130. Eisele, N. B.; Andersson, F. I.; Frey, S.; Richter, R. P., Viscoelasticity of thin biomolecular films: a case study on nucleoporin phenylalanine-glycine repeats grafted to a histidine-tag capturing QCM-D sensor. *Biomacromolecules* **2012**, *13*, 2322-2332.
131. Cho, N. J.; Kanazawa, K. K.; Glenn, J. S.; Frank, C. W., Employing two different quartz crystal microbalance models to study changes in viscoelastic behavior upon transformation of lipid vesicles to a bilayer on a gold surface. *Anal. Chem.* **2007**, *79*, 7027-7035.

132. Liu, Z.; Choi, H.; Gatenholm, P.; Esker, A. R., Quartz crystal microbalance with dissipation monitoring and surface plasmon resonance studies of carboxymethyl cellulose adsorption onto regenerated cellulose surfaces. *Langmuir* **2011**, *27*, 8718-8728.
133. Feiler, A. A.; Sahlholm, A.; Sandberg, T.; Caldwell, K. D., Adsorption and viscoelastic properties of fractionated mucin (BSM) and bovine serum albumin (BSA) studied with quartz crystal microbalance (QCM-D). *J. Colloid Interface Sci.* **2007**, *315*, 475-481.
134. Malmstrom, J.; Agheli, H.; Kingshott, P.; Sutherland, D. S., Viscoelastic modeling of highly hydrated laminin layers at homogeneous and nanostructured surfaces: quantification of protein layer properties using QCM-D and SPR. *Langmuir* **2007**, *23*, 9760-9768.
135. Stengel, G.; Hook, F.; Knoll, W., Viscoelastic modeling of template-directed DNA synthesis. *Anal. Chem.* **2005**, *77*, 3709-3714.
136. Hook, F.; Kasemo, B.; Nylander, T.; Fant, C.; Sott, K.; Elwing, H., Variations in coupled water, viscoelastic properties, and film thickness of a Mefp-1 protein film during adsorption and cross-linking: a quartz crystal microbalance with dissipation monitoring, ellipsometry, and surface plasmon resonance study. *Anal. Chem.* **2001**, *73*, 5796-5804.

Chapter 3: Viscoelastic Properties and Quantification of Mixed-Linkage β -Glucan

Adsorption onto Chitin and Cellulose Surfaces

3.1 Abstract

Fungal cell walls are an important front-line defense during fungal infection. As the major cell wall components, the assembly and interactions of glucan and chitin are crucial for understanding the fungal infection mechanism. In this study, adsorption of mixed-linkage glucan (MLG) onto regenerated chitin (RChitin) and cellulose (RC) surfaces are investigated and quantified by using a quartz crystal microbalance with dissipation monitoring (QCM-D) and atomic force microscopy (AFM). The QCM-D results showed that MLG was irreversibly adsorbed onto both surfaces and MLG adsorption increased with increasing concentration of MLG solutions before a plateau was achieved for concentration $> 50 \mu\text{g g}^{-1}$. Viscoelastic modeling was introduced into the QCM-D data analysis since the adsorbed MLG layers were dissipative soft layers. Voigt-based viscoelastic modeling results indicated that adsorbed MLG layers on RChitin and RC surfaces had similar shear viscosities of $\eta \sim 10^{-3} \text{ N s m}^{-2}$ and elastic shear moduli of $\mu \sim 10^5 \text{ N m}^{-2}$ with a layer thickness of $\sim 10 \text{ nm}$. MLG formed a soft hydrogel-like layer on both RChitin and RC surfaces based upon the modeling results. This work successfully established a QCM-D method to mimic and assemble the MLG layer observed in fungal and some plant cell walls.

3.2 Introduction

Fungal infections destroy more than 125 million tons of five vital crops: rice, wheat, potatoes, maize, and soybeans every year in the world.¹⁻² This amount could feed 600 million people.³ A recent report indicated that if these five crops were damaged simultaneously, a third of the world's population would struggle with starvation.⁴ Besides a threat in the field, fungal infections also lead to large losses at the post-harvest stage during product transport and storage. Various fungal

diseases in plants include: alternaria stem canker, cytosporina dieback, yellow leaf disease, etc.⁵ Hence, fungal infections and the further development of anti-fungal agents have been important topics in scientific research and medical areas over the past decades.⁶

Fungal cell walls are vital for the fungal infections and serve as the front line in host-pathogen interactions.⁷ The fungal cell is encapsulated within a complex matrix of cell wall, which is mainly composed of cross-linked polysaccharides and proteins.⁸⁻⁹ Fungal cell walls are dynamic structures with strong mechanical strength that protect fungal cells from deactivation under osmotic pressure, high salinity, temperature or other external conditions, and simultaneously allow fungal cells to communicate with the outer environment.¹⁰⁻¹¹ These cell walls mediate cell adhesion to the hosts by releasing specific adhesive enzymes, which are critical for the invasion of the host plant tissues.¹² Due to the defensive nature, the host plant cells excrete inhibitor proteins to prevent degradation induced by fungal enzymes and release reactive polysaccharide enzymes to degrade the fungal cell walls.¹³ Interestingly, fungal cells have a similar response mechanism to minimize the host-induced degradation of the cell walls.¹⁴ Therefore, the interplay between fungal and plant enzymes and their respective inhibitors plays an important role in the outcome of pathogenesis.¹⁵ Because of the significant role of the cell wall on fungal physiology, fungal cell walls have been considered as an excellent target for anti-fungal agents.^{11, 16} A dynamic invasion process is shown in Figure 3.1.

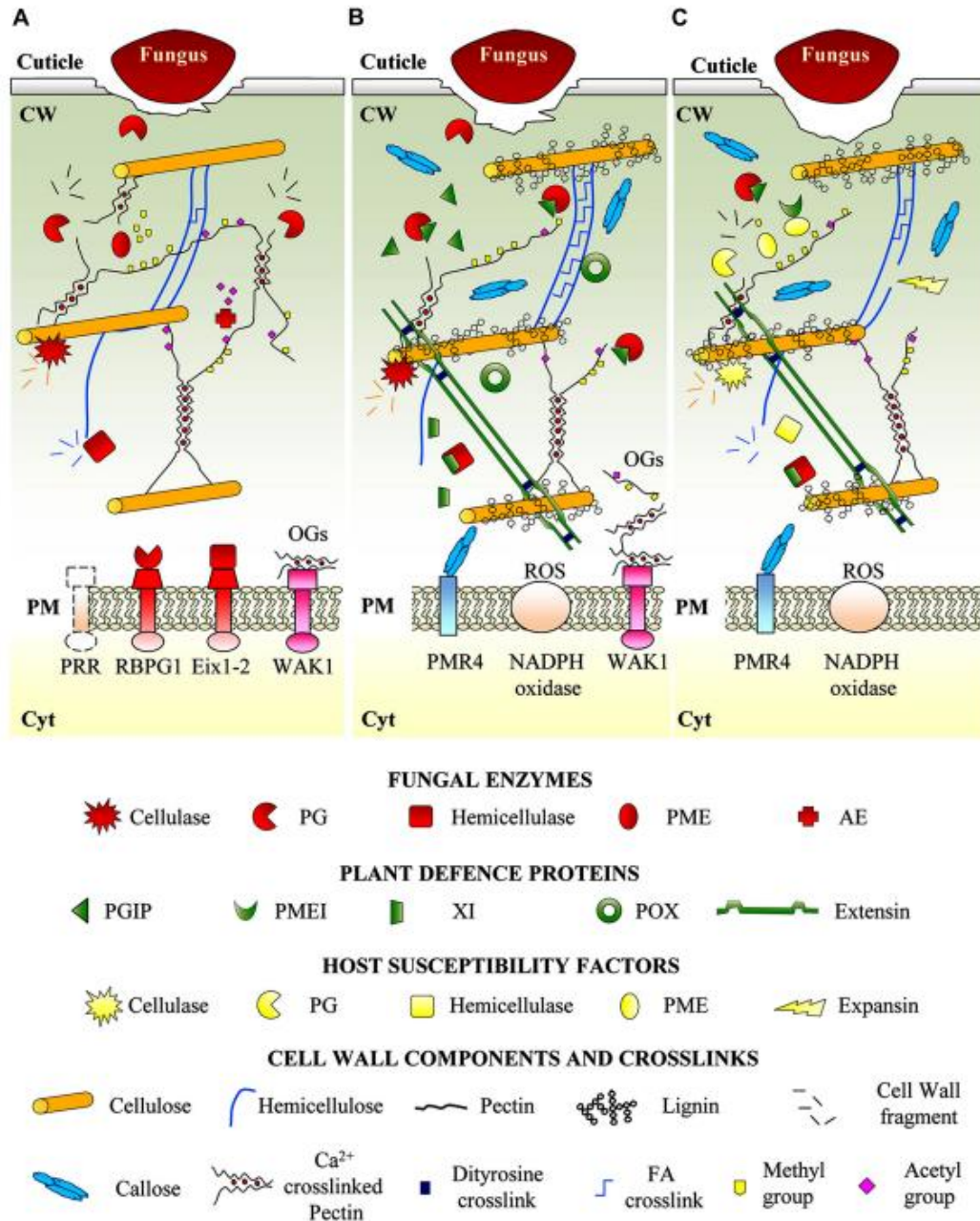


Figure 3.1 Dynamic fungal invasion into plant system. Reproduced from Lionetti et al. (Copyright 2014 Frontiers).¹⁷

Fungal cell walls differ greatly from cellulose-based plant cell walls in their structure and composition.¹⁸⁻¹⁹ The fungal cell walls are dynamic structures and are mainly comprised of chitin, different linkage glucans and glycoproteins with additional minor components that vary across

fungal species.^{7, 20-23} Plant cell walls are semi-permeable multi-layered structures that are comprised of celluloses, hemicelluloses, pectin, and proteins in primary cell walls and cellulose, hemicelluloses, and lignin in secondary cell walls.²⁴⁻²⁷ Mixed β -1,3- β -1,4-glucan (mixed-linkage glucan, MLG), as a major constituent in both fungal and plant cell walls, not only serves as a key structural element in fungal cell walls, but provides plant cells a defensive barrier against pathogenic fungal species.^{11, 28-29} Chitin and cellulose are major structural components in fungal and plant cell walls, respectively and they play a critical role in structural formation, the overall integrity, and physical strength of fungal and plant cell walls.^{11, 30-32}

A previous study demonstrated that MLG could be irreversibly adsorbed onto cellulose surfaces, forming a thick hydrogel. In plants, the MLG layer serves as attachable media for other polysaccharides and this feature was also studied.² However, the composition assembly and interactions of these polysaccharides in fungal cell walls are still poorly known. Therefore, in this work, we investigated and compared the adsorption of MLG onto chitin and cellulose surfaces through quartz crystal microbalance with dissipation monitoring (QCM-D) and atomic force microscopy (AFM) experiments. Viscoelastic properties and surface concentrations of the adsorbed MLG layers were determined and analyzed. This work employed a simplified in vitro QCM-D method to study the assembly of MLG onto chitin, an important structural element of fungal cell walls.

3.3 Experimental Section

3.3.1 Materials

α -Chitin from shrimp shells (practical grade, >95% acetylated) was purchased from Sigma-Aldrich and converted to trimethylsilyl chitin (TMSChitin, DS = 2.0) following a similar method in the literature.³³ Microcrystalline cellulose (Avicel PH-101, Fluka) was modified into

trimethylsilyl cellulose (TMSC, DS = 3.0) as previously reported.³⁴ Mixed-linkage glucan from Icelandic moss was purchased from Megazyme (Wicklow, Ireland). Gold sensors for QCM-D (diameter = 14 mm, thickness = 0.3 mm) were purchased from Q-sense AB. Ultrapure water (18.2 M Ω cm, <5 ppb inorganic impurities) was obtained from a Synergy UV system (Millipore) and used in all experiments. All other chemicals and solvents were used as received from Fisher Scientific.

3.3.2 Preparation of RChitin and RC Thin Films

The QCM-D gold sensors were initially cleaned prior to use by exposure to UV/ozone for 20 min, followed by immersion into a 1:1:5 by volume solution of hydrogen peroxide: ammonium hydroxide: ultrapure water at 80 °C for 1 h. Then the sensors were rinsed with ultrapure water and dried with nitrogen.

The synthesized TMSChitin powder was dissolved in a mixture of chloroform: tetrachloroethane (4:1, v/v) to make 0.8 wt% TMSChitin solutions which were then filtered with 0.45 μ m PTFE syringe filters. These solutions were spin-coated by dynamic dispersion of 100 μ L solution onto the top of the cleaned sensors spinning at a speed of 3000 rpm for 1 min. The resulting TMSChitin films were converted to amorphous regenerated chitin (RChitin) films by exposure to the vapor of a 10 wt% aqueous hydrochloric acid solution for 2 min. 1.2 wt% TMSC solutions in toluene were spin-coated by dynamic dispersion of 100 μ L solution onto the cleaned sensors spinning at a speed of 2000 rpm for 1 min. The TMSC films were then exposed to the vapor of a 10 wt% aqueous hydrochloric acid solution for 2 min to produce regenerated cellulose (RC) films.

3.3.3 Atomic Force Microscopy (AFM) Measurements

An MFP-3D-Bio AFM (Asylum Research) was applied in tapping mode for imaging of different surfaces. Samples were dried at 50 °C for several hours prior to analysis by AFM. Height images were collected under ambient conditions using a silicon tip (OMCL-AC160TS, Olympus Corp.). Root mean square roughness (RMS) of the films were calculated based upon $2\ \mu\text{m} \times 2\ \mu\text{m}$ scan areas.

3.3.4 Film Thickness Measurements

Thicknesses of RChitin and RC films were determined using ellipsometry (J.A. Woollam Co. VASE variable angle spectroscopic ellipsometer) under different angles of incidence (60-80° in 2° intervals). Measurements were performed in the spectral range between 250-800 nm at these incident angles. The thicknesses of the films were modeled using WVASE 32 software and each film was measured at three spots to obtain the average thickness with one standard deviation.

3.3.5 QCM-D Measurements

Adsorption of MLG onto RChitin and RC surfaces was monitored by QCM-D (Q-Sense E4, Biolin Scientific AB). The QCM-D sensors spincoated with RChitin or RC films were placed in a flow cell and equilibrated in air and sodium acetate buffer (SA, 20 mM, pH 5.5) at a flow rate of $0.20\ \text{mL}\cdot\text{min}^{-1}$ at 20 °C. After that, the MLG solution was injected into the system until a stable state was established. Pure SA buffer was then flowed over the sensor for the removal of reversibly adsorbed MLG. Changes in (Δf) and dissipation (ΔD) were monitored simultaneously for all six odd overtones ($n = 3, 5, 7, \dots, 13$), corresponding to resonance frequencies of 15, 25, 35, ..., 65 MHz, respectively. Changes in dissipation and scaled frequency ($\Delta f/n$) were obtained. QCM-D experiments were performed three times for each system.

3.3.6 Viscoelastic Modeling

The thickness and viscoelastic properties of the MLG layers were estimated by fitting the MLG adsorption data to a Voigt-based viscoelastic model.³⁵⁻³⁶ In this model, the adsorbed MLG layers were treated as a viscoelastic layer between the elastic sensor and viscous bulk solution. This model related the measured Δf and ΔD (eq 1 and 2) to the viscoelastic properties of the adsorbed MLG layers and bulk solution.

$$\Delta f = \frac{Im(\beta)}{2\pi t_q \rho_q} \quad (3.1)$$

$$\Delta D = -\frac{Re(\beta)}{\pi f t_q \rho_q} \quad (3.2)$$

In the above equations, ρ_q is the density of quartz ($2650 \text{ kg}\cdot\text{m}^{-3}$) and β is a complex function of viscosity, elasticity, and density of the bulk solution and MLG layers. The Voigt model describes the viscoelastic properties of MLG layers via a complex shear modulus G :

$$G = G' + iG'' = \mu + i2\pi f \eta \quad (3.3)$$

where G' and G'' are the storage and loss moduli, respectively; μ and η are the shear elastic modulus and viscosity. In the standard viscoelastic model, shear elastic modulus and viscosity are independent of frequency. In the advanced model, power law frequency dependent shear elastic moduli and viscosities are more realistic and yield better modeling results.³⁷ For the elastic shear modulus μ :

$$\mu = \mu_0 (f/f_0)^{\alpha'} \quad (3.4)$$

where μ_0 is the shear elastic modulus at the fundamental frequency ($f_0 = 5 \text{ MHz}$) and α' is the exponent for μ ($0 \leq \alpha' \leq 2$). For the shear viscosity η :

$$\eta = \eta_0(f/f_0)^{\alpha''} \quad (3.5)$$

where η_0 is the shear viscosity at the fundamental frequency and α'' is the exponent for η ($-1 \leq \alpha'' \leq 1$).

In this study, the QCM-D adsorption data were analyzed using Qsense modeling software at different overtones. Estimates of the five fitting parameters in the advanced model: the thickness (h_f), viscoelastic parameters (μ and η) and frequency dependent exponents (α' and α'') were obtained. For the standard model, only three fitting parameters were obtained (h_f , μ and η). Density of the MLG film (ρ_f) and h_f were not independent variables, so ρ_f was set to $1050 \text{ kg}\cdot\text{m}^{-3}$ for a water-rich MLG film to estimate thickness.² The fitting results were obtained by minimizing χ^2 value, where $Y_{theory,i}$ and $Y_{meas,i}$ represent the theoretically predicted and experimentally measured values of Δf and ΔD for different overtones ($n = 3, 5, 7, 9, 11, 13$), respectively.³⁸ σ_i is the standard

$$\chi^2 = \sum_i \left(\frac{Y_{theory,i} - Y_{meas,i}}{\sigma_i} \right)^2 \quad (3.6)$$

deviation for each data point. The surface concentrations ($\Gamma_{\text{QCM-D}}$) for the MLG adsorption onto RChitin and RC surfaces were deduced from the equation:

$$\Gamma_{\text{QCM-D}} = h_f \rho_f \quad (3.7)$$

3.4 Results and Discussion

3.4.1 Adsorption of MLG onto RChitin and RC Surfaces

Herein, we employed QCM-D to study the adsorption with time dependent profiles for the $\Delta f/n$ and ΔD values and representative QCM-D data are provided in Figure 3.1. There were significant $\Delta f/n$ decreases and ΔD increases when MLG buffer solutions were introduced into the system. These changes were caused by MLG adsorption and increased viscosity and density of the

bulk polymer solution relative to the buffer. About 30 mins (for RChitin surfaces) and 40 mins (for RC surfaces) later, both $\Delta f/n$ and ΔD profiles reached plateaus, indicating the adsorption had slowed. As shown in Figure 3.2, final values of $\Delta f/n$ and ΔD did not return to baseline after the reintroduction of pure buffer solution. This demonstrates that MLG remained irreversibly bound to both RChitin and RC surfaces. When the adsorption of MLG was analyzed on both RChitin and RC surfaces, MLG saturation occurred quickly. This strong interaction with RChitin and RC would also be present in fungal cell walls where MLG also undergoes covalent crosslinking to the RChitin and RC.^{2, 39}

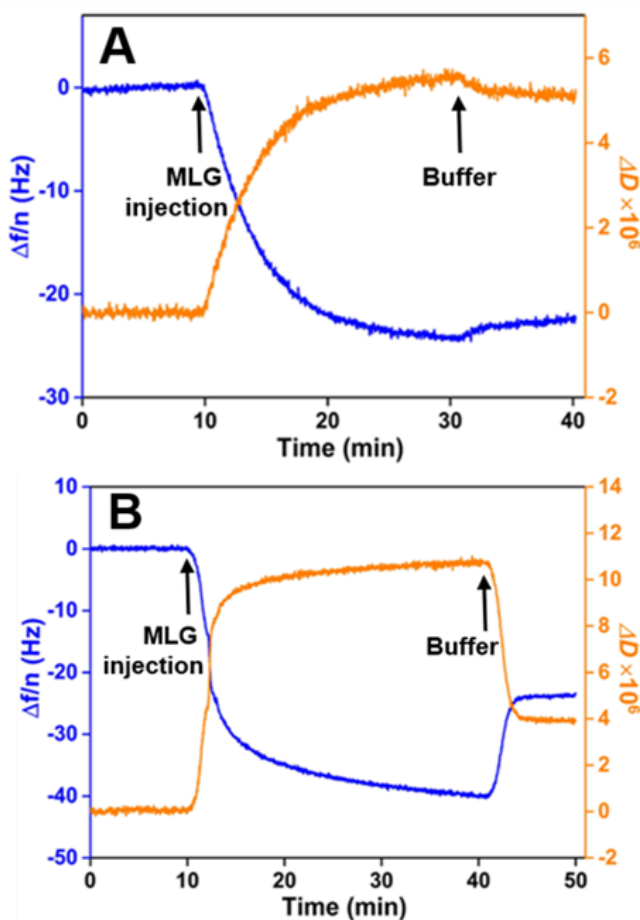


Figure 3.2 Time-dependent $\Delta f/n$ and ΔD profiles for MLG solution ($100 \mu\text{g g}^{-1}$) adsorbed on (A) RChitin surface and (B) RC surface. Curves correspond to the fifth overtone.

3.4.2 Concentration Effects of MLG Adsorption onto RChitin and RC Surfaces

The concentration effects of the MLG adsorption onto RChitin and RC surfaces were investigated and summarized in Figure 3.3. At both RChitin and RC surfaces, greater changes in $\Delta f/n$ and ΔD values were observed for the adsorption of MLG solutions at higher concentrations. An increase in dissipation was associated with greater frequency changes at higher MLG concentrations, suggesting an increase in the magnitude of the viscoelastic modeling.⁴⁰⁻⁴¹ This trend was attributed to more MLG adsorption with its coupled water at higher concentrations. When the concentrations of MLG solutions exceeded $50 \mu\text{g g}^{-1}$, constant $\Delta f/n$ and ΔD values indicated the MLG adsorption likely plateaued on both RChitin and RC surfaces. Moreover, on the plateau, adsorbed MLG caused greater frequency and smaller dissipation changes on RC than RChitin substrates. This indicated that the adsorbed MLG formed a more dense layer with less coupled water on RC surfaces than the MLG layer on RChitin surfaces.⁴² These results reflect that MLG has stronger interactions with RC than RChitin.

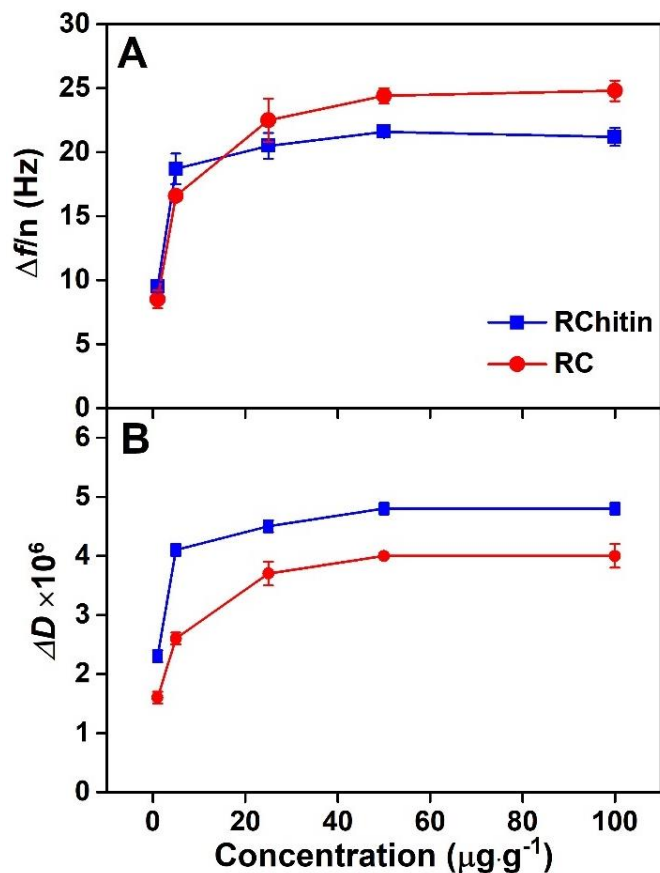


Figure 3.3 Summary of $\Delta f/n$ and ΔD for MLG adsorption onto RChitin and RC Surfaces at different MLG concentrations.

3.4.3 Characterization of Chitin and Cellulose Surfaces

The thicknesses of RChitin and RC films were determined by ellipsometry. RChitin and RC films have a similar thickness around 20 nm (23.7 ± 0.3 nm for RChitin and 22.7 ± 0.3 nm for RC). Their thicknesses are comparable to the thicknesses of chitin and cellulose layers in the real fungal and plant cells.⁴³ The morphological changes of RChitin and RC films before and after MLG adsorption were investigated by AFM. As shown in Figure 3.4A and B, before MLG adsorption, the RChitin and RC films were both smooth with RMS roughness values of 1.7 and 1.6 nm,

respectively. The roughness values of RChitin and RC films are similar to the roughness of RChitin and RC films (~1.5 nm) with a similar thickness (~20 nm) from previous studies.^{2, 44}

After MLG adsorption onto the surfaces, MLG coated RChitin and RC sensors were dried in a vacuum oven at 50 °C and then imaged with AFM. Representative AFM images are displayed in Figure 3.4. MLG aggregates were observed on both RChitin and RC substrates with RMS roughness of 2.2 nm and 2.6 nm, respectively. It was reported that small round particles in AFM images were observed for MLG deposited onto pure mica surfaces after vacuum drying because of the existence of weak interactions between MLG chains themselves and between MLG chains and the mica surface.⁴⁵ Since all the samples were vacuum-dried for AFM imaging, the network morphology indicated a relatively strong hydrogen binding interaction between MLG and RChitin/RC substrates. Further, Figure 3.4C and D confirmed that the frequency decrease and dissipation increase of QCM-D data after the introduction of MLG solution were caused by the adsorption and binding of MLG with coupled water onto RChitin and RC surfaces.

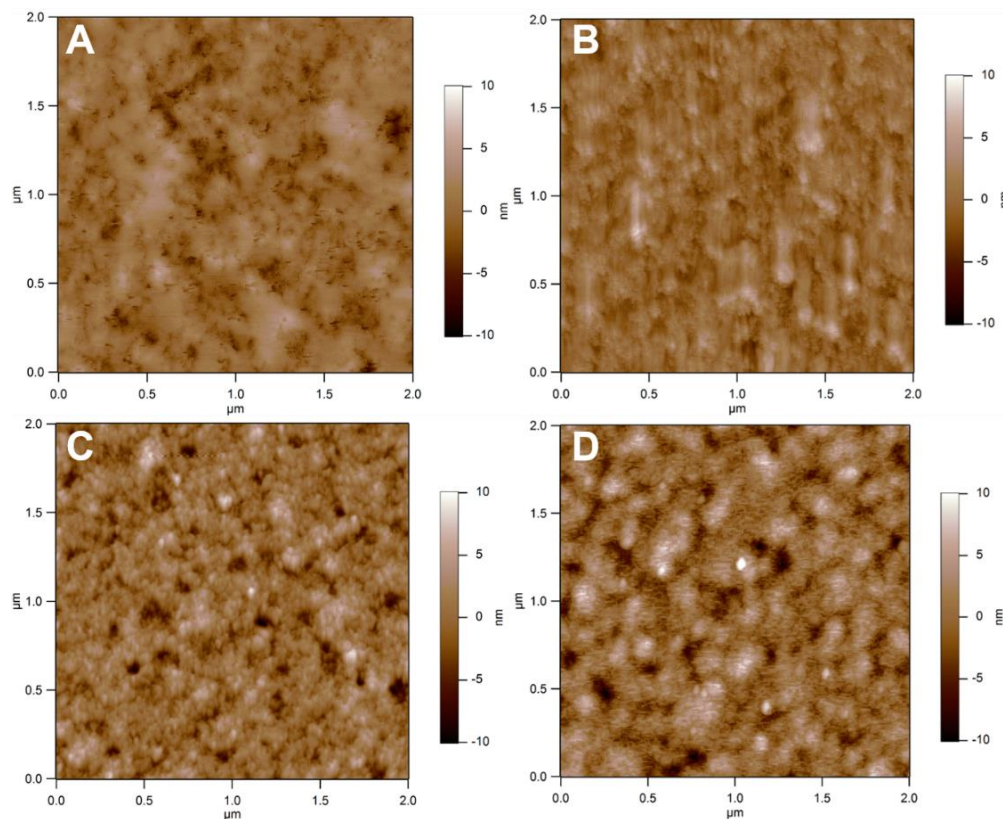


Figure 3.4 AFM height images ($2\ \mu\text{m} \times 2\ \mu\text{m}$) of morphology on different surfaces. (A) RChitin, (B) RC, (C) MLG coated RChitin, (D) MLG coated RC. RMS roughnesses for the images are (A) $\sim 1.7\ \text{nm}$, (B) $\sim 1.6\ \text{nm}$, (C) $\sim 2.2\ \text{nm}$, and (D) $\sim 2.6\ \text{nm}$.

3.4.4 Viscoelastic Properties of MLG Layers onto RChitin and RC Surfaces

The adsorption of MLG on both RChitin and RC surfaces formed soft and dissipative layers ($\Delta D > 4 \times 10^{-6}$). For such layers, Voigt-based viscoelastic modeling was introduced for the estimation of viscoelastic properties (μ and η) and the hydrodynamic thicknesses (h_f) of the adsorbed layers.⁴⁶ The adsorption QCM-D curves were analyzed and fitted with this viscoelastic model, using the combined data of Δf and ΔD at six overtones ($n = 3, 5, 7, 9, 11, 13$) to get the best estimation.⁴⁷ The density and viscosity of water were used for all the bulk solutions as the diluted electrolytes and biomacromolecules had little effect on the density and viscosity values of

the bulk solutions. For simplicity, the density of adsorbed layers (ρ_f) was assumed to be constant and set to 1050 kg m^{-3} throughout the adsorption process. In the real case, ρ_f would increase from 1000 kg m^{-3} to 1050 kg m^{-3} continuously during the adsorption process, and we therefore underestimated h_f , μ and η slightly by a few percent.

The standard viscoelastic model with three frequency-independent fitting parameters (h_f , μ and η) is a poor model for very few real-world materials in the MHz frequency range used by QCM-D. Thus, we have used a frequency dependent elastic shear modulus and viscosity. In this advanced viscoelastic model, estimates of five fitting parameters: thickness (h_f), shear elasticity and viscosity (μ and η), and frequency dependent exponents (α' and α'') were obtained. Values of h_f , μ , η , α' , and α'' were summarized in Table 3.1A and B. The modeling results showed that thicker MLG layers could be formed on both RChitin and RC surfaces with higher MLG concentrations in the bulk solutions. Both shear elastic modulus and viscosity increased as the thickness increased for the MLG layers formed on the surfaces, suggesting a stronger network structure through junction zones due to the intra and intermolecular hydrogen bonding.⁴⁸ The values of shear elastic modulus ($< 10^5 \text{ N m}^{-2}$) and the shear viscosity which was less than a factor of two and greater than water indicated a soft hydrogel-like state for the adsorbed MLG layers on RChitin and RC surfaces. This gel-like state of MLG on chitin surfaces is consistent with the hypothesis that MLG forms a gel-like matrix and interchain hydrogen bonds with chitin microfibrils in fungal cell wall that form a tensile and robust basket-like scaffold around the cell.⁸ Meanwhile, this gel-like state on cellulose surfaces also supports the hypothesis that MLG forms a gel-like matrix between cellulose microfibrils in the primary plant cell wall, providing functions such as wall hydration and cell-to-cell adhesion.⁴⁹ Moreover, the modeling results demonstrated that MLG formed a more loose and thicker layer on RChitin surfaces with weaker viscoelastic properties and less polymer chain

interactions compared to the layer formed on RC surfaces. This corresponds well to the frequency and dissipation changes of QCM-D data for the MLG adsorption on RChitin and RC substrates.

Table 3.1A Thickness and Viscoelastic Parameters of Adsorbed MLG Layers on RChitin Surfaces from Voigt-Based Model.

concentration of MLG ($\mu\text{g g}^{-1}$)	RChitin		
	thickness h_f (nm)	elastic shear modulus $\mu \times 10^{-5}$ (N m^{-2})	shear viscosity $\eta_f \times 10^3$ (N s m^{-2})
100	9.06 ± 0.14	0.50 ± 0.01	1.62 ± 0.02
50	8.92 ± 1.01	0.52 ± 0.09	1.74 ± 0.12
25	7.68 ± 0.77	0.49 ± 0.08	1.59 ± 0.04
5	5.89 ± 0.97	0.39 ± 0.04	1.32 ± 0.03
1	4.88 ± 0.20	0.31 ± 0.02	1.24 ± 0.13

Table 3.1B Thickness and Viscoelastic Parameters of Adsorbed MLG Layers on RC Surfaces from Voigt-Based Model.

concentration of MLG ($\mu\text{g g}^{-1}$)	RC		
	thickness h_f (nm)	elastic shear modulus $\mu \times 10^{-5}$ (N m^{-2})	shear viscosity $\eta_f \times 10^3$ (N s m^{-2})
100	7.84 ± 0.60	0.62 ± 0.05	2.06 ± 0.02
50	8.14 ± 0.65	0.54 ± 0.10	2.04 ± 0.14
25	6.91 ± 0.40	0.53 ± 0.06	1.96 ± 0.06
5	4.78 ± 0.17	0.42 ± 0.04	1.52 ± 0.08
1	3.19 ± 0.34	0.39 ± 0.07	1.42 ± 0.14

Representative QCM-D data for MLG adsorption from buffer solution onto RChitin substrate and the best fits (the parameter sets generated the lowest χ^2 from viscoelastic model for overtone 3-13) are displayed in Figure 3.5. As shown in Figure 3.5, there was an excellent agreement between experimental data and simulated data for all overtones. Prior to the development of frequency dependent modeling software, most research tried to estimate viscoelastic parameters

using subsets of overtones.^{2, 38, 47, 50} This approach had the disadvantage of a relative inability to fit even three overtones with large discrepancies between low and high frequency data.

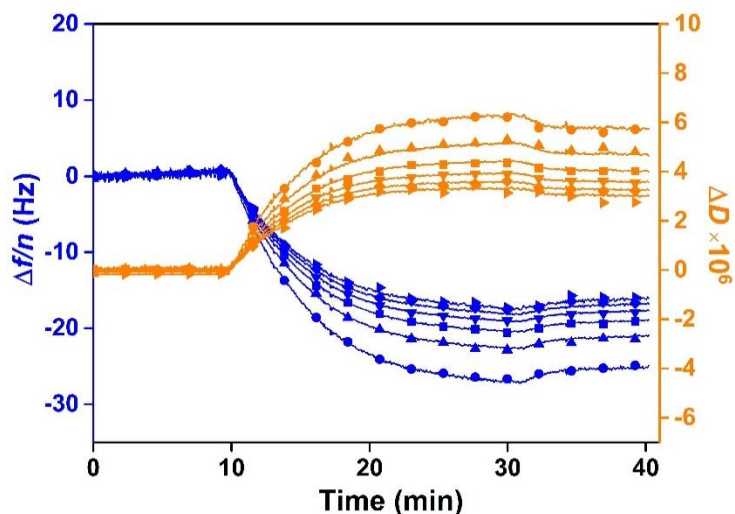


Figure 3.5 Adsorption of MLG ($100 \mu\text{g g}^{-1}$) onto a RChitin substrate from SA buffer at 20°C and best fits were obtained from Voigt-based viscoelastic modeling. Isolated symbols represent the experimental data from $n = (\bullet) 3, (\blacktriangle) 5, (\blacksquare) 7, (\blacktriangledown) 9, (\blacklozenge) 11$ and $(\blacktriangleright) 13$ and solid lines represent fits of the experimental data set.

Figure 3.6 displays time-dependent h_f , μ , η , α' , and α'' profiles corresponding to the best-fit curves in Figure 3.5. Note that μ and η here represent μ_0 and η_0 at the fundamental frequency. Both μ and η increased with the increase of h_f during the MLG adsorption process and at maximal MLG coverage ($h_{f, \max}$), μ and η reached their maximal values. This again demonstrated greater MLG content exhibited stronger viscoelastic properties. Meanwhile, α' decreased from around 0.06 to -0.05 and α'' decreased from 0.42 to 0.25 during MLG adsorption process. α' is beyond the normal range $0 \leq \alpha' \leq 2$ a little at the final state, which may be caused by instrumental noise and is still in a physically reasonable range $-0.05 \leq \alpha' \leq 2.05$.³⁸ Both α' and α'' are nonzero suggesting that the viscoelastic properties are frequency-dependent.

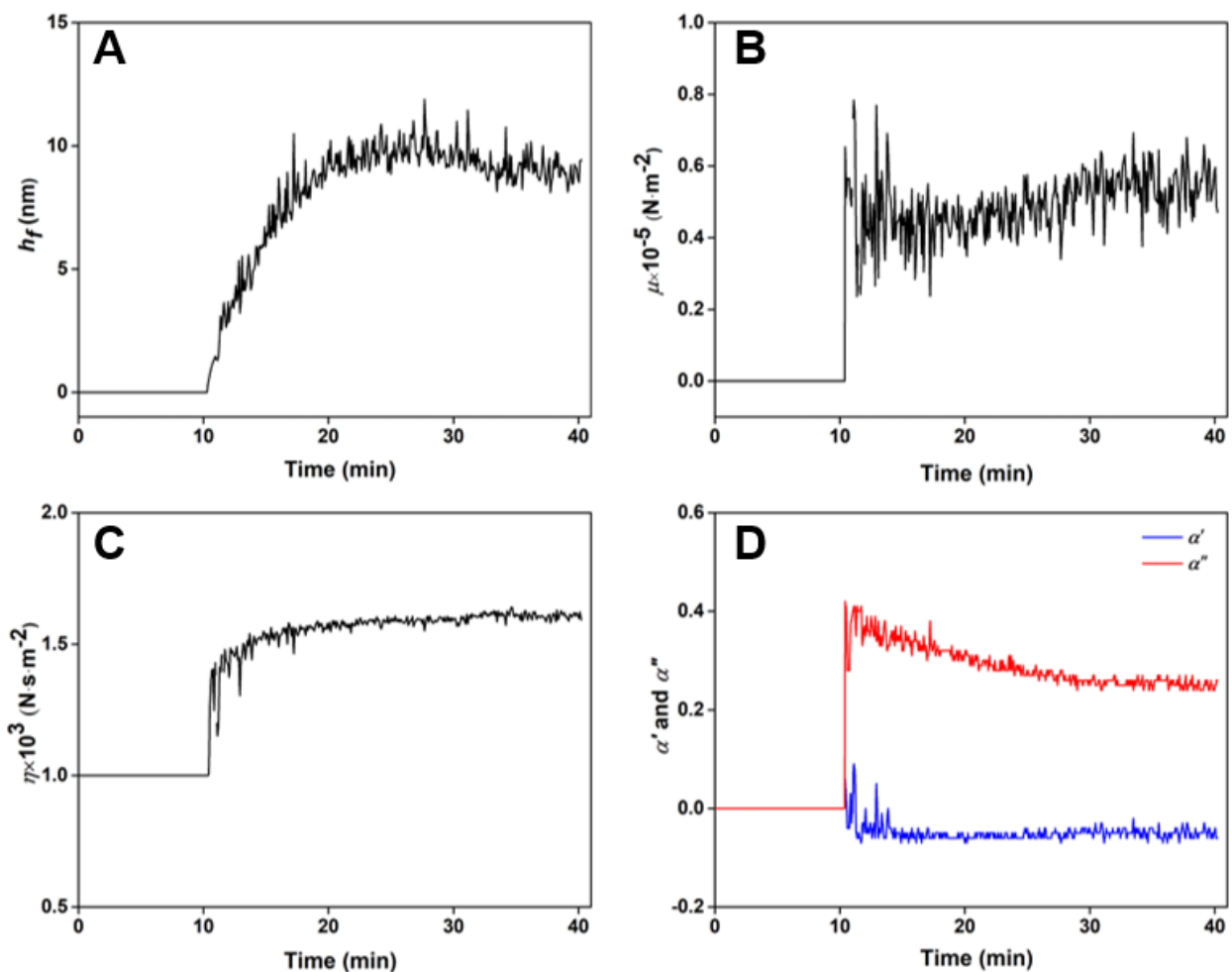


Figure 3.6 Representative time dependent evolution of changes in parameters associated with the frequency-dependent viscoelastic modeling for the adsorption of MLG ($100 \mu\text{g g}^{-1}$) onto a RChitin substrate: (A) thickness versus time; (B) shear elastic modulus versus time; (C) viscosity versus time; (D) frequency dependence α' of μ and α'' of η versus time.

3.4.5 Surface Concentration of MLG on RChitin and RC Films

Having obtained the estimated film thicknesses of the adsorbed MLG layers from the modeling results, we calculated surface concentrations, $\Gamma_{\text{QCM-D}}$ at different bulk concentrations based upon equation (3.7). Figure 3.7 shows surface concentrations versus bulk concentrations for MLG

adsorption on RChitin and RC surfaces with a surface plateau at $\Gamma_{\text{QCM-D}} \sim 9.51$ and 8.23 mg m^{-2} , respectively. Based upon the molecular structures, the adsorption of MLG onto RChitin and RC surfaces are expected to occur through hydrogen bonding at the initial stage. After that, MLG could not only bind to RChitin and RC surfaces, but also bind to MLG already adsorbed on the surfaces, thus forming a thicker MLG layer. MLG-MLG hydrogen bonding would be consistent with the aggregation of MLG which is facilitated by the high molecular weight and asymmetrical conformations of MLG.⁵¹⁻⁵² The type of substrate surfaces (RChitin versus RC) has some effects on the polymer adsorption and viscoelastic properties of the adsorbed layer. For instance, RChitin surfaces have shown stronger overall interactions towards MLG and coupled water with higher $\Gamma_{\text{QCM-D}}$ than RC surfaces ($\sim 16\%$ higher). This observation could reflect the fact that the MLG we used was extracted from lichen where interaction with chitin in the fungal cell walls would be necessary for survival. However, RC surfaces have shown greater affinity towards pure MLG with less dissipation and stronger viscoelastic properties. This may be caused by the stronger hydrogen bonding between MLG and cellulose compared to chitin surfaces.⁵³⁻⁵⁴

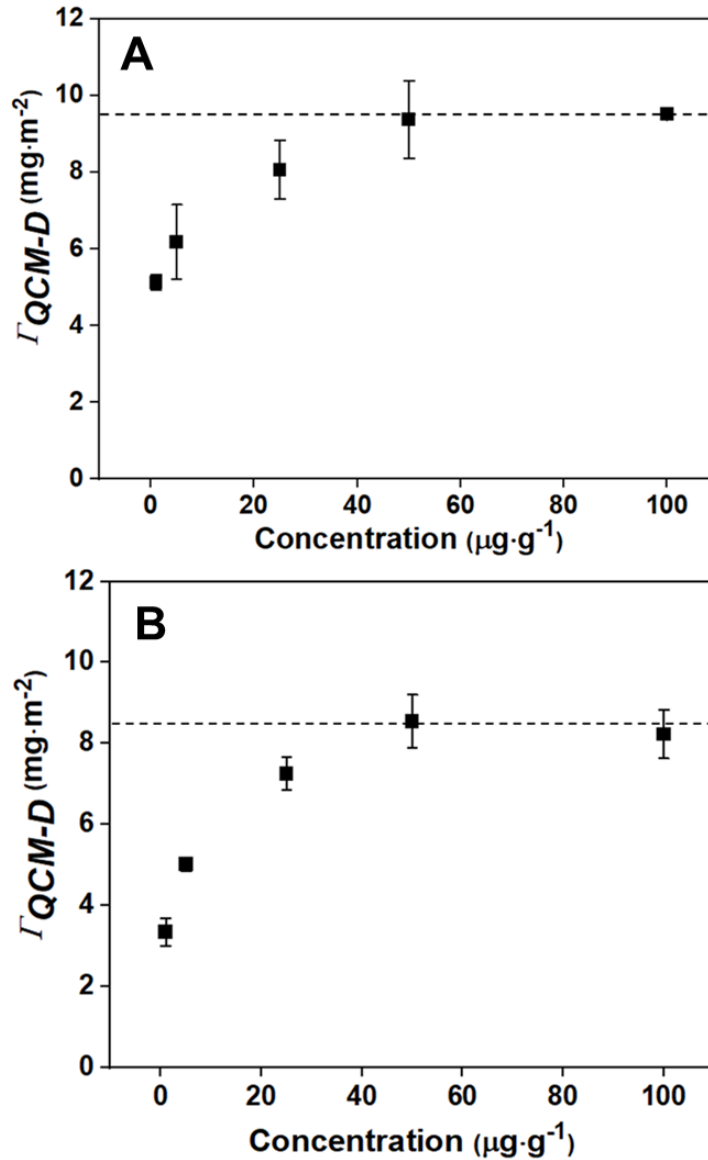


Figure 3.7 Surface concentrations versus bulk concentrations for MLG adsorption onto (A) RChitin and (B) RC surfaces at 20 °C. The dashed line is present to approximate a plateau value and facilitate comparisons.

3.5 Conclusions

This study demonstrated irreversible binding of MLG on both RChitin and RC surfaces by QCM-D and AFM. The adsorbed MLG layers which have a thickness around 10 nm, are hydrogel-

like layers with viscoelastic properties obtained from viscoelastic modeling. Surface concentrations of adsorbed MLG on both RChitin and RC surfaces were quantified based upon modeling results. Compared with RC surfaces, adsorption of MLG onto RChitin surfaces tended to be more dissipative and yielded thicker hydrogel-like layers with larger thickness. This work successfully established a method to mimic and assemble the natural polymers in fungal and plant cell walls. Further studies like enzyme accessibility to the MLG coated RChitin surfaces are anticipated to better understand the fungal infection mechanism and the further strategies for anti-fungal drugs.

3.6 References

1. Almeida, F.; Rodrigues, M. L.; Coelho, C., The Still Underestimated Problem of Fungal Diseases Worldwide. *Front. Microbiol.* **2019**, *10*, 214.
2. Kiemle, S. N.; Zhang, X.; Esker, A. R.; Toriz, G.; Gatenholm, P.; Cosgrove, D. J., Role of (1,3)(1,4)-beta-glucan in cell walls: interaction with cellulose. *Biomacromolecules* **2014**, *15*, 1727-1736.
3. Savary, S.; Ficke, A.; Aubertot, J. N.; Hollier, C., Crop losses due to diseases and their implications for global food production losses and food security. Springer: 2012.
4. Fisher, M. C.; Henk, D. A.; Briggs, C. J.; Brownstein, J. S.; Madoff, L. C.; McCraw, S. L.; Gurr, S. J., Emerging fungal threats to animal, plant and ecosystem health. *Nature* **2012**, *484*, 186-194.
5. Oliver, R. P.; Solomon, P. S., Recent fungal diseases of crop plants: is lateral gene transfer a common theme? *Mol. Plant Microbe. Interact.* **2008**, *21*, 287-293.
6. Gow, N. A.; Brown, A. J.; Odds, F. C., Fungal morphogenesis and host invasion. *Curr. Opin. Microbiol.* **2002**, *5*, 366-371.

7. Wessels, J. G. H., Developmental Regulation of Fungal Cell-Wall Formation. *Annu. Rev. Phytopathol.* **1994**, *32*, 413-437.
8. Geoghegan, I.; Steinberg, G.; Gurr, S., The Role of the Fungal Cell Wall in the Infection of Plants. *Trends Microbiol.* **2017**, *25*, 957-967.
9. Cabib, E.; Bowers, B.; Sburlati, A.; Silverman, S. J., Fungal cell wall synthesis: the construction of a biological structure. *Microbiol. Sci.* **1988**, *5*, 370-375.
10. Bowman, S. M.; Free, S. J., The structure and synthesis of the fungal cell wall. *Bioessays* **2006**, *28*, 799-808.
11. Free, S. J., Fungal cell wall organization and biosynthesis. *Adv. Genet.* **2013**, *81*, 33-82.
12. Chaffin, W. L., *Candida albicans* cell wall proteins. *Microbiol. Mol. Biol. Rev.* **2008**, *72*, 495-544.
13. Albersheim, P.; Valent, B. S., Host-pathogen interactions: VII. Plant pathogens secrete proteins which inhibit enzymes of the host capable of attacking the pathogen. *Plant Physiol.* **1974**, *53*, 684-687.
14. Ham, K. S.; Wu, S. C.; Darvill, A. G.; Albersheim, P., Fungal pathogens secrete an inhibitor protein that distinguishes isoforms of plant pathogenesis-related endo- β -1, 3-glucanases. *Plant J.* **1997**, *11*, 169-179.
15. Ferreira, R. B.; Monteiro, S.; Freitas, R.; Santos, C. N.; Chen, Z. J.; Batista, L. M.; Duarte, J.; Borges, A.; Teixeira, A. R., Fungal pathogens: The battle for plant infection. *Crit. Rev. Plant Sci.* **2006**, *25*, 505-524.
16. Debono, M.; Gordee, R. S., Antibiotics That Inhibit Fungal Cell-Wall Development. *Annu. Rev. Phytopathol.* **1994**, *48*, 471-497.

17. Bellincampi, D.; Cervone, F.; Lionetti, V., Plant cell wall dynamics and wall-related susceptibility in plant–pathogen interactions. *Front. Plant Sci.* **2014**, *5*, 228-235.
18. Bartnicki-Garcia, S., Cell wall chemistry, morphogenesis, and taxonomy of fungi. *Annu. Rev. Microbiol.* **1968**, *22*, 87-108.
19. Cosgrove, D. J., Wall structure and wall loosening. A look backwards and forwards. *Plant Physiol.* **2001**, *125*, 131-134.
20. Satoh, T.; Takeuchi, O.; Vandebon, A.; Yasuda, K.; Tanaka, Y.; Kumagai, Y.; Miyake, T.; Matsushita, K.; Okazaki, T.; Saitoh, T.; Honma, K.; Matsuyama, T.; Yui, K.; Tsujimura, T.; Standley, D. M.; Nakanishi, K.; Nakai, K.; Akira, S., The Jmjd3-Irf4 axis regulates M2 macrophage polarization and host responses against helminth infection. *Nat. Immunol.* **2010**, *11*, 936-944.
21. Reese, T. A.; Liang, H. E.; Tager, A. M.; Luster, A. D.; Van Rooijen, N.; Voehringer, D.; Locksley, R. M., Chitin induces accumulation in tissue of innate immune cells associated with allergy. *Nature* **2007**, *447*, 92-96.
22. Klis, F. M., Review: cell wall assembly in yeast. *Yeast* **1994**, *10*, 851-869.
23. Kang, X.; Kirui, A.; Muszynski, A.; Widanage, M. C. D.; Chen, A.; Azadi, P.; Wang, P.; Mentink-Vigier, F.; Wang, T., Molecular architecture of fungal cell walls revealed by solid-state NMR. *Nat. Commun.* **2018**, *9*, 2747-2758.
24. Cosgrove, D. J., Growth of the plant cell wall. *Nat. Rev. Mol. Cell. Biol.* **2005**, *6*, 850-861.
25. Lampugnani, E. R.; Khan, G. A.; Somssich, M.; Persson, S., Building a plant cell wall at a glance. *J. Cell Sci.* **2018**, *131*, 1-6.
26. Keegstra, K., Plant cell walls. *Plant Physiol.* **2010**, *154*, 483-486.

27. Wilder, B. M.; Albersheim, P., The Structure of Plant Cell Walls: IV. A Structural Comparison of the Wall Hemicellulose of Cell Suspension Cultures of Sycamore (*Acer PseudoPlatanus*) and of Red Kidney Bean (*Phaseolus Vulgaris*). *Plant Physiol.* **1973**, *51*, 889-893.
28. Buckeridge, M. C.; Rayon, C.; Urbanowicz, B.; Tiné, M. A. S.; Carpita, N. C., Mixed linkage (1→3),(1→4)-β-d-glucans of grasses. *Cereal Chem.* **2004**, *81*, 115-127.
29. Brown, G. D.; Gordon, S., Fungal beta-glucans and mammalian immunity. *Immunity* **2003**, *19*, 311-315.
30. Bayer, E. A.; Chanzy, H.; Lamed, R.; Shoham, Y., Cellulose, cellulases and cellulosomes. *Curr. Opin. Struct. Biol.* **1998**, *8*, 548-557.
31. Ruiz-Herrera, J.; San-Blas, G., Chitin synthesis as a target for antifungal drugs. *Curr. Drug Targets Infect. Disord.* **2003**, *3*, 77-91.
32. Mayer, A. M., Plant-fungal interactions: A plant physiologist's viewpoint. *Phytochemistry* **1989**, *28*, 311-317.
33. Kurita, K.; Sugita, K.; Kodaira, N.; Hirakawa, M.; Yang, J., Preparation and evaluation of trimethylsilylated chitin as a versatile precursor for facile chemical modifications. *Biomacromolecules* **2005**, *6*, 1414-1418.
34. Kontturi, E.; Thune, P. C.; Niemantsverdriet, J. W., Cellulose model surfaces-simplified preparation by spin coating and characterization by X-ray photoelectron spectroscopy, infrared spectroscopy, and atomic force microscopy. *Langmuir* **2003**, *19*, 5735-5741.
35. Voinova, M. V.; Rodahl, M.; Jonson, M.; Kasemo, B., Viscoelastic acoustic response of layered polymer films at fluid-solid interfaces: Continuum mechanics approach. *Physica. Scripta.* **1999**, *59*, 391-396.

36. Hook, F.; Kasemo, B.; Nylander, T.; Fant, C.; Sott, K.; Elwing, H., Variations in coupled water, viscoelastic properties, and film thickness of a Mefp-1 protein film during adsorption and cross-linking: A quartz crystal microbalance with dissipation monitoring, ellipsometry, and surface plasmon resonance study. *Anal. Chem.* **2001**, *73*, 5796-5804.
37. Sun, L.; Svedhem, S.; Akerman, B., Construction and Modeling of Concatemeric DNA Multilayers on a Planar Surface as Monitored by QCM-D and SPR. *Langmuir* **2014**, *30*, 8432-8441.
38. Eisele, N. B.; Andersson, F. I.; Frey, S.; Richter, R. P., Viscoelasticity of thin biomolecular films: a case study on nucleoporin phenylalanine-glycine repeats grafted to a histidine-tag capturing QCM-D sensor. *Biomacromolecules* **2012**, *13*, 2322-2332.
39. Douglas, C. M., Fungal beta(1,3)-D-glucan synthesis. *Med. Mycol.* **2001**, *39* 55-66.
40. Kittle, J. D.; Qian, C.; Edgar, E.; Roman, M.; Esker, A. R., Adsorption of Xyloglucan onto Thin Films of Cellulose Nanocrystals and Amorphous Cellulose: Film Thickness Effects. *ACS Omega* **2018**, *3*, 14004-14012.
41. Kittle, J.; Levin, J.; Levin, N., Water Content of Polyelectrolyte Multilayer Films Measured by Quartz Crystal Microbalance and Deuterium Oxide Exchange. *Sensors (Basel)* **2021**, *21*, 771-782.
42. Reviakine, I.; Johannsmann, D.; Richter, R. P., Hearing what you cannot see and visualizing what you hear: interpreting quartz crystal microbalance data from solvated interfaces. *Anal. Chem.* **2011**, *83*, 8838-8848.
43. Gow, N. A. R.; Latge, J. P.; Munro, C. A., The Fungal Cell Wall: Structure, Biosynthesis, and Function. *Microbiol. Spectr.* **2017**, *5*, 1-25.

44. Wang, C.; Kittle, J. D.; Qian, C.; Roman, M.; Esker, A. R., Chitinase activity on amorphous chitin thin films: a quartz crystal microbalance with dissipation monitoring and atomic force microscopy study. *Biomacromolecules* **2013**, *14*, 2622-2628.
45. Morgan, K. R.; Roberts, C. J.; Tendler, S. J. B.; Davies, M. C.; Williams, P. M., A ¹³C CP/MAS NMR spectroscopy and AFM study of the structure of Glucagel™, a gelling β-glucan from barley. *Carbohydr. Res.* **1999**, *315*, 169-179.
46. Raudino, M.; Giambianco, N.; Montis, C.; Berti, D.; Marletta, G.; Baglioni, P., Probing the Cleaning of Polymeric Coatings by Nanostructured Fluids: A QCM-D Study. *Langmuir* **2017**, *33*, 5675-5684.
47. Liu, Z.; Choi, H.; Gatenholm, P.; Esker, A. R., Quartz crystal microbalance with dissipation monitoring and surface plasmon resonance studies of carboxymethyl cellulose adsorption onto regenerated cellulose surfaces. *Langmuir* **2011**, *27*, 8718-8728.
48. Salgado, M.; Santos, F.; Rodríguez-Rojo, S.; Reis, R. L.; Duarte, A. R. C.; Cocero, M. J., Development of barley and yeast β-glucan aerogels for drug delivery by supercritical fluids. *J. CO₂ Util.* **2017**, *22*, 262-269.
49. Harris, P. J.; Fincher, G. B., Distribution, fine structure and function of (1, 3; 1, 4)-β-glucans in the grasses and other taxa. *Anal. Biochem.* **2009**, 621-654.
50. Chen, Q.; Xu, S.; Liu, Q.; Masliyeh, J.; Xu, Z., QCM-D study of nanoparticle interactions. *Adv. Colloid Interface Sci.* **2016**, *233*, 94-114.
51. Lazaridou, A.; Biliaderis, C.; Izydorczyk, M., Molecular size effects on rheological properties of oat β-glucans in solution and gels. *Food Hydrocoll.* **2003**, *17*, 693-712.
52. Lazaridou, A.; Biliaderis, C., Molecular aspects of cereal β-glucan functionality: Physical properties, technological applications and physiological effects. *J. Cereal Sci.* **2007**, *46*, 101-118.

53. Nishiyama, Y., Molecular interactions in nanocellulose assembly. *Philos. Trans. A Math. Phys. Eng. Sci.* **2018**, *376*, 47-57.
54. Deringer, V. L.; Englert, U.; Dronskowski, R., Nature, Strength, and Cooperativity of the Hydrogen-Bonding Network in alpha-Chitin. *Biomacromolecules* **2016**, *17*, 996-1003.

Chapter 4: Solvent-Resistant Self-Crosslinked Poly(ether imide)

Part of this chapter is adapted from a manuscript published in *Macromolecules*. Full text of the published manuscript, entitled “*Solvent-Resistant Self-Crosslinked Poly(ether imide)*” by Zhen Xu, Gehui Liu, Ke Cao, Dong Guo, Joel Serrano, Alan R. Esker, and Guoliang (Greg) Liu, *Macromolecules* **2021**, *54*, 3405-3412.

4.1 Abstract

Poly(ether imide) (PEI) is a high-performance polymer with excellent thermal and mechanical properties. However, PEI has poor solvent resistance towards solvents including chloroform, dimethylformamide, dichloromethane, and N-methyl pyrrolidone. Exposure to these solvents severely affects the thermal and mechanical performances of PEI. Herein, we introduce a simple method to prepare crosslinked PEI (X-PEI) from azide-terminated PEI (N_3 -PEI- N_3) via a thermal crosslinking reaction. X-PEIs maintain outstanding solvent resistance towards typical solvents as evidenced by swelling ratio tests using a quartz crystal microbalance with dissipation monitoring (QCM-D). The glass transition temperature, storage modulus, and swelling ratio correlate positively with crosslinking density, which is determined by the molar mass and azide concentration of the N_3 -PEI- N_3 . This work advances the chemistry of polymer materials and can be applicable to other polymers.

4.2 Introduction

With outstanding thermal and mechanical performances, poly(ether imide) (PEI) has numerous industrial applications, in the transportation, aerospace, and medical devices.¹⁻³ As a high-performance engineering thermoplastic, PEI is widely employed for the current industrial requirements, though, it still faces several challenges. First, PEI has relatively poor processibility with higher processing temperature (340 to 400 °C) than typical commodity plastics, which

requires greater energy consumption and causes slight polymer degradation.⁴⁻⁵ Second, poor solvent resistance in organic environments, including chloroform, *N,N*-dimethylformamide (DMF), tetrahydrofuran (THF), dichloromethane (DCM), and *N*-methyl pyrrolidone (NMP) limits some applications.⁶ In order to overcome these challenges, novel chemistries to improve solvent-resistance and processibility without the sacrifice of thermal and mechanical properties are required.

Two approaches have been proposed to improve processibility with reduced processing temperature, 1) polymer blending; and 2) oligomerization compensated by molecular interactions. Mixing PEI with flexible polymer additives is a simple and economical way to reduce the melting temperature and improve processibility. However, the overall thermal and mechanical properties of the blend are usually reduced due to the phase separation of the components.⁷ In the past two decades, many polymer additives have been used including polycarbonate,⁸ polyamide,⁹ and polyester.¹⁰⁻¹² Among them, only some aromatic polycarbonates and polyesters demonstrate improved processibility without a sacrifice of thermal and mechanical performances.¹³ An alternative approach is the design of terminal-functionalized PEI oligomers, which have reduced processing viscosity and energy costs.¹ After processing, these oligomers can be linked together through molecular interactions including hydrogen bonding,⁶ and ionic bonding,¹⁴⁻¹⁵ or chemical reactions of the terminal functional groups that yield covalent bonding.¹⁶⁻²⁰ Resultant PEI has enhanced interactions to compensate for the thermal and mechanical performance loss from the low molecular weight. Covalent interaction is the choice for preparing solvent resistant PEI. Introduction of crosslinkable end-groups to the oligomers allows good processibility prior to the crosslinking reaction. After processing the polymer into the desired shape, the crosslinking

reaction generates permanent covalent bonds with enhanced solvent resistance, and at the same time maintains the shape with good thermal and mechanical properties.^{19, 21-23}

Among different crosslinking approaches, ultraviolet light (UV) and thermal crosslinking are the most popular methods.²⁴⁻²⁶ Since UV crosslinking initiates at surface layers because of the strong UV-absorptive nature of PEI, extended irradiation is needed to improve the crosslinking density, and this often leads to polymer degradation.⁴ Thermal crosslinking, on the other hand, is a more uniform, efficient, and less destructive crosslinking method compared with UV crosslinking.²⁷ Thermal crosslinker such as nitrile,¹⁶ amine,²⁸ and acetylene²⁹ are typically used in the crosslinking reaction for most engineering plastics. However, the efficiency is low, and crosslinking is unreliable. For instance, P84 polyimide crosslinked by diamines have been successfully industrialized (tradenames: DuraMemTM or PuraMemTM), although they are susceptible to reversible decrosslinking³⁰ and linker leaching.³⁰ The ideal crosslinker should be efficient, environmentally-friendly, and safe. Herein, we introduce azide chemistry to prepare solvent-resistant PEI, maintaining good thermal and mechanical properties via an efficient thermal crosslinking method.³¹ Azide can be thermally triggered easily (<150 °C) and generate highly reactive nitrenes, aziridines, and dihydroazepine, which can react with groups like aryl and alkyl groups from PEI backbones.³²⁻³⁴ PEI was designed with azide end-group structure and this azide terminated PEI had a high crosslinking efficiency without linker leaching or explosion.³⁵

In this work, the azide-terminated PEIs (N₃-PEI-N₃) were prepared via a heterogenous diazotization-azidation reaction. They were then solution-cast into films and thermally crosslinked in a vacuum oven at 220 °C. Compared with conventional PEI, the crosslinked PEIs (X-PEIs) displayed enhanced thermal and mechanical properties. More importantly, X-PEIs exhibited excellent resistance to common solvents in contrast to non-crosslinked PEIs. The azide-terminated

PEI with a molecular weight of 8.9 kDa had the greatest crosslinking density and the best thermal, mechanical, and solvent resistance performances.

4.3 Experimental Section

4.3.1 Materials

Dichloromethane (DCM, Spectranalyzed®, Fisher Chemical), chloroform (HPLC, Fisher Chemical), tetrahydrofuran (THF, Fisher Chemical), *N*-methyl formamide (DMF, analytical pure, Acros Organics), *N*-methyl pyrrolidone (NMP, Reagentplus® 99%, Sigma-Aldrich), sodium azide (NaN_3 , $\geq 98\%$, Sigma-Aldrich), sodium nitrite (NaNO_2 , $\geq 98\%$, Sigma-Aldrich), acetone (analytical pure, Acros Organics), hexanes (VWR chemicals), methanol (VWR chemicals), concentrated sulfuric acid (H_2SO_4 , wt% $\geq 98\%$, Fisher Chemical), and deuterated chloroform (CDCl_3 , 99.8%, Cambridge Isotope Laboratories, Inc.) were used as received.

4.3.2 Characterization

Proton nuclear magnetic resonance (^1H NMR) spectroscopy was performed on a Varian Unity 400 spectrometer at 399.98 MHz in CDCl_3 . Thermogravimetric analysis (TGA) was performed on a Discovery TGA5500 thermogravimetric analyzer (TA Instruments). Polymers were preheated at 200 °C for 10 min, and then the weight changes were measured from 200 to 800 °C at a ramp rate of 10 °C min^{-1} under a nitrogen stream of 25 mL min^{-1} . Number average molecular weight (M_n) was measured via an EcoSEC HLC-8320GPC size exclusion chromatography equipped with two TSKgel SuperHM-H columns, a refractive index detector, and a multi-angle light scattering detector (SEC-MALS) at 50 °C with flow rate of 0.5 mL min^{-1} . The mobile phase for the SEC-MALS was DMF containing 0.05 M LiBr. Fourier transform infrared spectroscopy (FTIR) was performed at room temperature using a PerkinElmer ATR-FTIR (model Spectrum 100) in the

range of 4000–1000 cm^{-1} with 256 scans and resolution of 4 cm^{-1} . Differential scanning calorimetry (DSC) was conducted from 40 to 250 $^{\circ}\text{C}$ with a heating rate of 10 $^{\circ}\text{C min}^{-1}$ and cooling rate of 20 $^{\circ}\text{C min}^{-1}$ under a nitrogen stream of 25 mL min^{-1} on a Discovery DSC2500 (TA Instruments). The DSC instrument was calibrated using indium and zinc standards and the glass transition temperature (T_g) was determined at the midpoint of the transition during the second heating ramp. Dynamic mechanical analysis (DMA) was performed on a DMA Q800 (TA Instruments) equipped with film tension clamps. The films were fixed in the tension clamps with a torque of 3 N and a preloaded force of 0.01 N. The storage modulus was obtained using a constant strain mode at 0.04%, 1 Hz frequency, and a heating rate of 3 $^{\circ}\text{C min}^{-1}$.

4.3.3 Preparation of Crosslinked PEI (X-PEI) Films

The azide-terminated PEI ($\text{N}_3\text{-PEI-N}_3$) with different molecular weights (7.1 kDa, 8.9 kDa, 12.8 kDa, 15.2 kDa) was prepared via heterogeneous diazotization-azidation reactions and was then characterized by our collaborators. After synthesis, the powder $\text{N}_3\text{-PEI-N}_3$ was then dissolved in DCM and solution cast into a Teflon dish. The solution-cast films were thermally triggered and crosslinked in the vacuum oven using a temperature program: starting at 40 $^{\circ}\text{C}$, the oven temperature was increased to 180 $^{\circ}\text{C}$ at a rate of 10 $^{\circ}\text{C h}^{-1}$. The heating rate was then increased to 40 $^{\circ}\text{C h}^{-1}$ to reach the final 220 $^{\circ}\text{C}$ and the oven was kept isothermal at 220 $^{\circ}\text{C}$ overnight to fully crosslink $\text{N}_3\text{-PEI-N}_3$.

4.3.4 Solvent Resistance Test by QCM-D

Solvent resistance of Ultem 1010 and X-PEI films were investigated by using a QCM-D (Q-Sense E4, Biolin Scientific AB) vapor sorption test. The QCM-D sensors were spin-coated with 0.1 wt% $\text{N}_3\text{-PEI-N}_3$ solutions in chloroform and then thermally treated in a vacuum oven at 230 $^{\circ}\text{C}$ for 24 h. Gas uptake was measured with controlled activity ($a \sim 0.9$) for different solvents.³⁶ The

activity was controlled by setting the temperature of the gas saturator cell at 18.5 °C and the QCM-D sensors at 20 °C. The activity was calculated according to Equation (4.1),

$$a = \frac{P_1}{P_1^*} \quad (4.1)$$

where P_1 is the vapor pressure of the organic solvent at the temperature of gas saturator cell and P_1^* is the vapor pressure of the organic solvent at the temperature of QCM-D sensors. Ultem 1010 and X-PEIs coated sensors were placed in the QCM-D flow cells flushed by targeting vapor carried by N₂, where changes in frequency (Δf) and dissipation (ΔD) of polymer-coated quartz crystals were monitored simultaneously. Vapor exposure continued until the gas sorption reached equilibrium. The swelling ratios (α) of PEI films in different solvents were calculated based upon Equation 4.2,³⁷

$$\alpha = \frac{m_s}{m_p} = \frac{\Delta f_s}{\Delta f_p} \quad (4.2)$$

where m_s and m_p are the masses of the solvent gas and pure polymer films, respectively; Δf_s is the change in frequency due to the gas uptake; and Δf_p is the change in frequency due to the loading of PEI films. Note that, mass ratios were converted to frequency ratios according to the Sauerbrey relationship: the changes in mass on the quartz surface are proportional to changes in frequency of the oscillating crystal.³⁸

4.4 Results and Discussion

4.4.1 Preparation of X-PEI Films

The solution cast N₃-PEI-N₃ films from DCM were thermally triggered and crosslinked under a temperature-programmed vacuum oven (Figure 4.1). NMR and FTIR data from Figure 4.2 confirmed the chemical structure of N₃-PEI-N₃. N₃-PEI-N₃ displayed a greater yellowness than the original NH₂-PEI-NH₂ and the X-PEIs were the most yellow among all PEIs, as demonstrated by

the pictures in Figure 4.1. There are two reasons for the more intense yellow color of the N₃-PEI-N₃ films. First, most organic azide groups absorb light around 350 nm, resulting in some yellowness.³⁹ Moreover, the charge-transfer complex effects within the N₃-PEI-N₃ structures and the electron deficient azide groups further amplified these effects with a final deep yellow color.⁴⁰ The deeper color of X-PEIs was firstly attributed to the fact that the electron-donating amine linkages (-NH-) within the PEI backbones formed from the thermally triggered crosslinking reaction of N₃-PEI-N₃ led to the high electron density in the charge-transfer complex.⁴¹⁻⁴² Second, after crosslinking, phenyl azides produce amine, azo-compounds, hydrazine, dehydroazepines, and aziridines through complex mechanisms.⁴³ These moieties could cause intermolecular reactions and yield chromophores with deep colors.

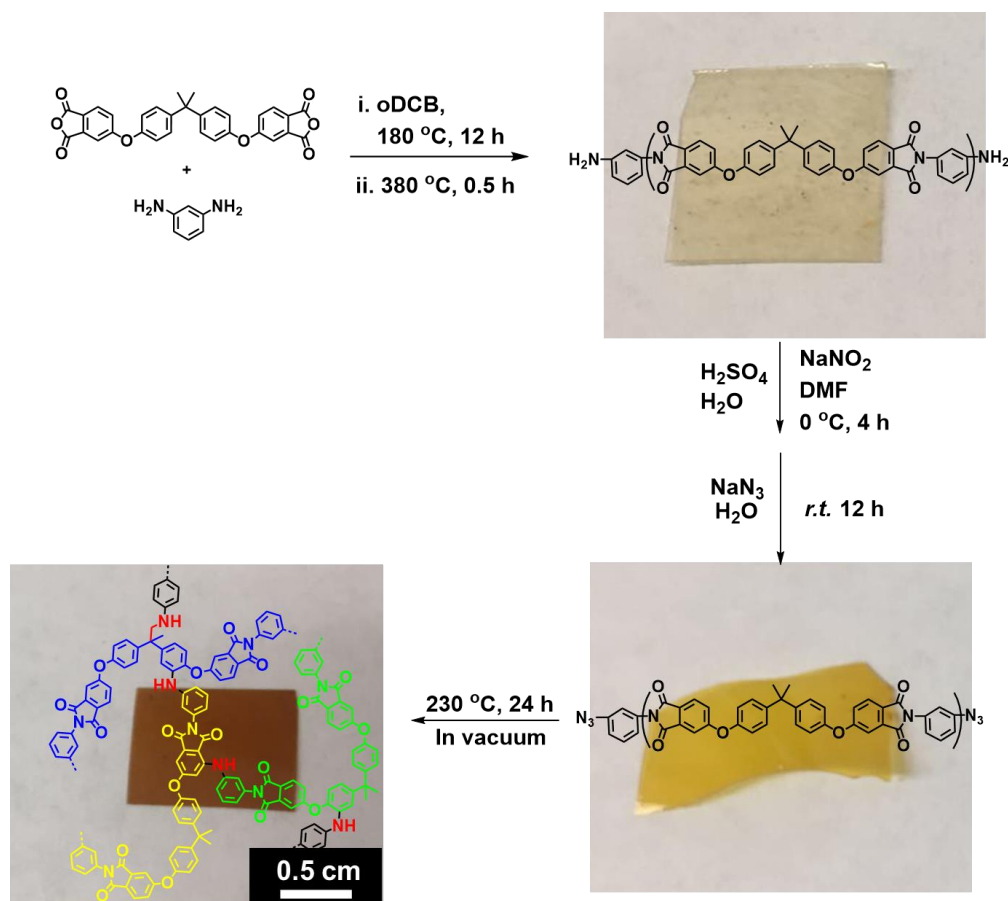


Figure 4.1 Synthesis and preparation of N₃-PEI-N₃ and X-PEI.

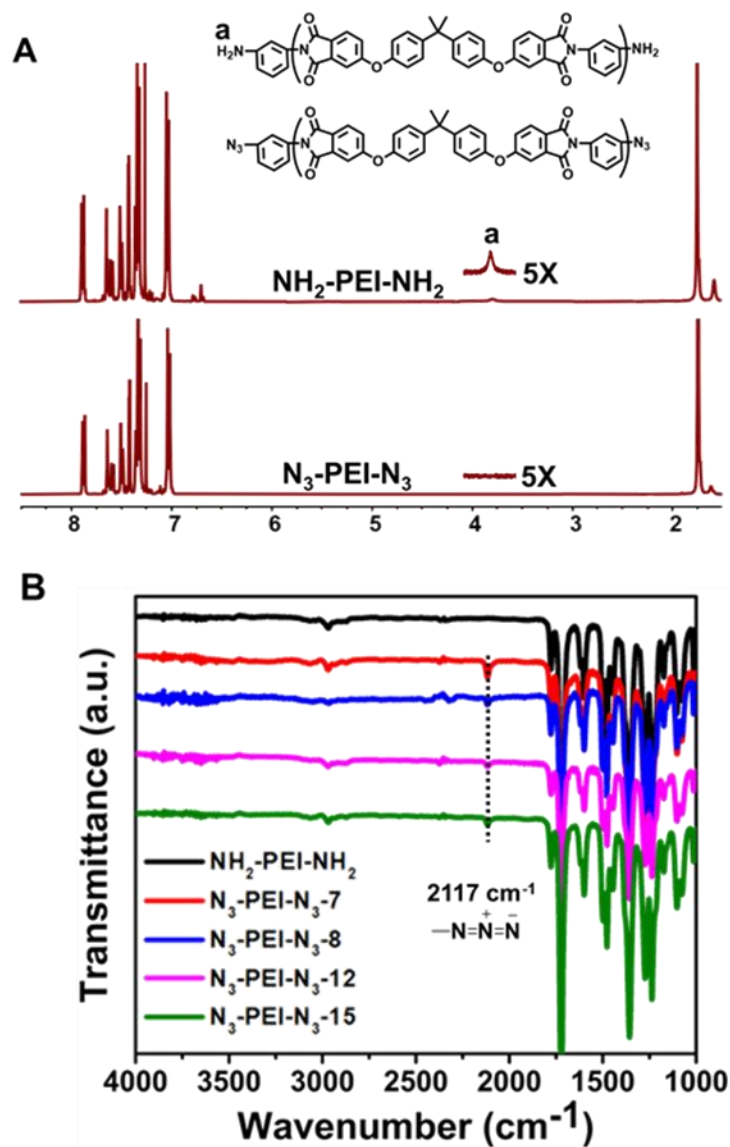


Figure 4.2 (A) ^1H NMR of $\text{NH}_2\text{-PEI-NH}_2$ and $\text{N}_3\text{-PEI-N}_3$ with $M_n = 8.9$ kDa. (B) FTIR spectra of $\text{NH}_2\text{-PEI-NH}_2$ ($M_n = 8.9$ kDa) and $\text{N}_3\text{-PEI-N}_3$ with varying molecular weights.

4.4.2 Physical Properties of X-PEIs

The mechanical behavior of X-PEIs was studied and compared with commercial PEI (Ultem 1010, 19 kDa). Below T_g , X-PEIs have higher storage moduli than Ultem 1010 except for X-PEI-15. T_g to 350 °C, X-PEIs had rubbery plateau storage moduli values, whereas Ultem 1010 flowed and fully yielded at ~ 280 °C due to melting (Figure 4.3). The different mechanical behaviors

between X-PEIs and Ultem 1010 were attributed to the crosslinking reaction, which restricted chain motion and therefore reduced damping and improved elasticity. In addition, $\tan \delta$ of X-PEIs at T_g were lower than Ultem 1010 at T_g , an indication that the X-PEIs were more elastic. We attribute the different thermomechanical behaviors between X-PEIs and Ultem 1010 to the crosslinking reaction. The crosslinked X-PEIs had restricted chain motion, thus reduced damping and improved elasticity. Above 350 °C, X-PEIs became stiff, and the storage moduli increased from <10 MPa to >500 MPa. This stiffening behavior at elevated temperatures broadened the service temperature range of X-PEIs.

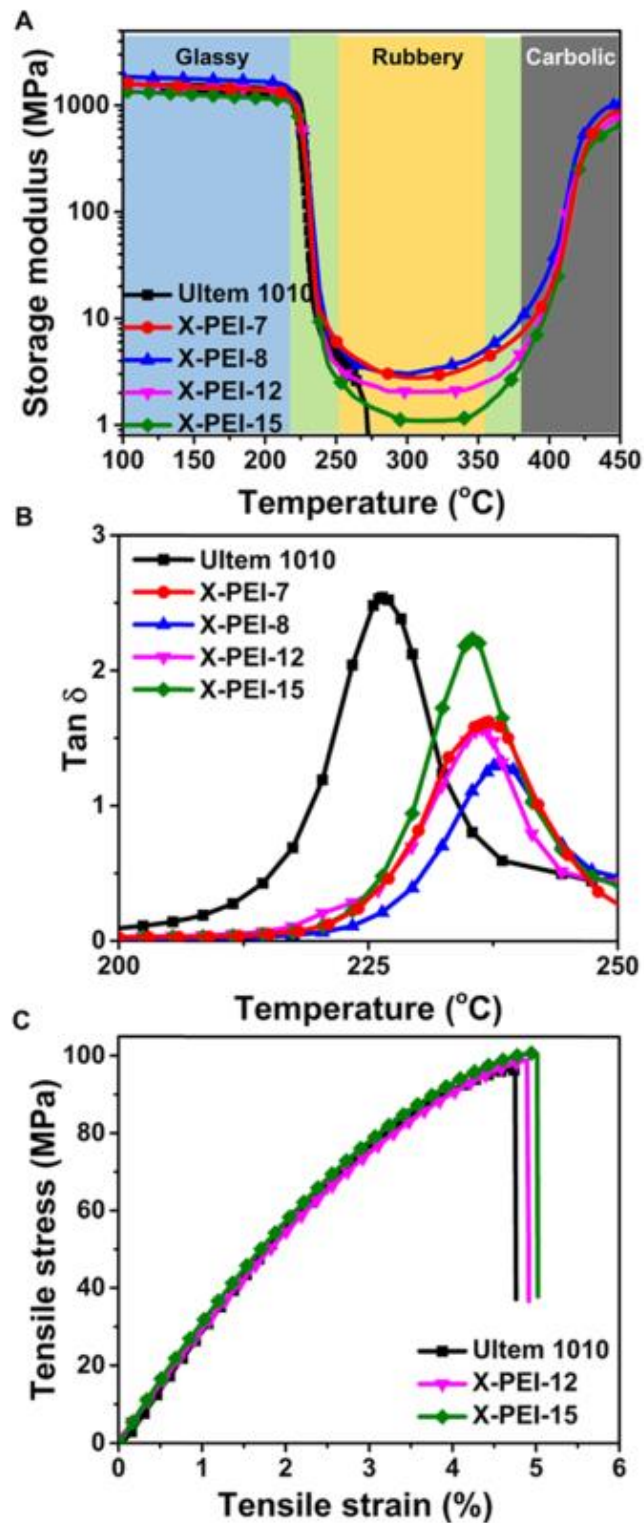


Figure 4.3 (A) Storage moduli and (B) $\text{Tan } \delta$ of Ultem 1010 and XPEIs. (C) Tensile stress-strain curves of Ultem 1010, X-PEI-15, and X-PEI-12 measured at room temperature.

The thermal properties of X-PEIs were investigated by DSC and TGA. All X-PEIs demonstrated higher T_g than commercial Ultem 1010, resulting in a wider service temperature range than commercial PEI (Figure 4.4). The glass transition temperatures of X-PEIs depended upon the crosslinking density which was then determined by the molecular weight of N_3 -PEI- N_3 and the relative azide concentration. Lower molecular weight with shorter chains prevented crosslinking reactions because of poor intermolecular interactions. However, higher molecular weight with longer chains had lower azide concentration and less crosslinking sites. As a result, a moderate molecular weight of 8.9 kDa displayed the highest T_g with the optimal chain length for crosslinking.⁴⁴⁻⁴⁵

Thermal decomposition temperatures (T_d) of X-PEIs increased with the molecular weight of N_3 -PEI- N_3 , but lower than that of Ultem 1010 (Figure 4.4B). Typically, polymers show reduced T_d after modifications, such as introduction of electron-rich CTC, less stable moieties, reversible crosslinkers, and asymmetric monomer. For X-PEIs, the reduced T_d is mainly attributed to the less thermally stable amine linkages that usually decompose at ~ 300 °C. However, it is important to note that the decomposition of amine linkages did not compromise the mechanical properties at high temperatures, because an oxidative crosslinking was initiated in the same temperature range (300 to 400 °C) to enhance the mechanical strength. A summary of physical properties of N_3 -PEI- N_3 and X-PEIs is also provided in Table 4.1.

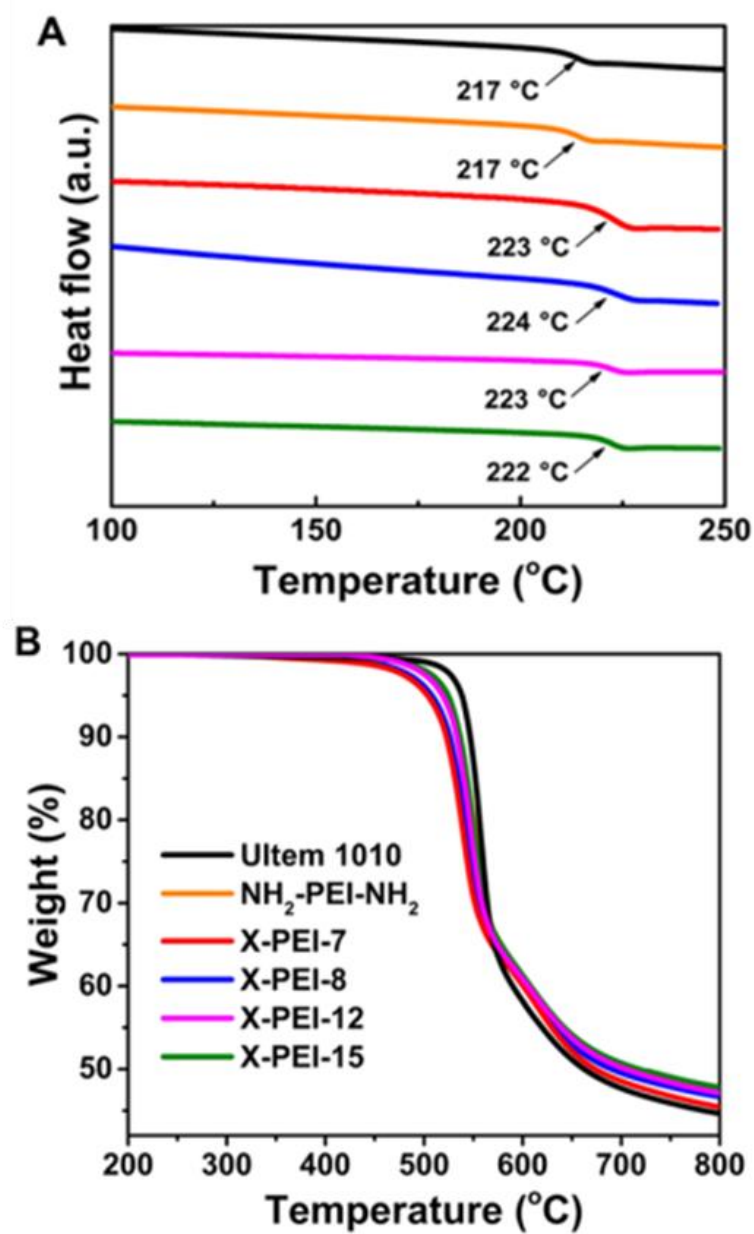


Figure 4.4 DSC and TGA traces of Ultem 1010, NH₂-PEI-NH₂, X-PEI-7, X-PEI-8, X-PEI-12, and X-PEI-15. The legend for B also applies to A. The arrows indicate T_g .

Table 4.1 Physical properties of N₃-PEI-N₃ and X-PEIs.

	M_n (kDa)		T_g (°C)		T_d (°C)	E' (GPa) ^b	Equilibrium E' (MPa) ^c
	NMR	SEC	DSC	DMA			
X-PEI-7 ^a	7.1	7.1	223	237	541	1.61 ± 0.05	2.28 ± 0.17
X-PEI-8	8.1	8.9	224	238	544	1.76 ± 0.04	2.31 ± 0.24
X-PEI-12	11.6	12.8	223	236	549	1.46 ± 0.08	1.86 ± 0.26
X-PEI-15	14.5	15.2	222	234	552	1.27 ± 0.07	1.31 ± 0.21
Ultem 1010	-	-	217	226	558	1.43 ± 0.04	-

^a The number after X-PEI refers to the number average molecular weight (in kDa) of PEI prepolymer as determined by NMR

^b The storage moduli (tensile moduli, E') were measured by DMA at 100 °C.

^c The storage moduli were measured by DMA at 280 °C.

4.4.3 Solvent Resistance

The most remarkable feature of X-PEIs is their solvent resistance. Typically, chloroform, DCM, DMF, and NMP are well-known good solvents for PEI. In an immersion test, all noncrosslinked NH₂-PEI-NH₂ and N₃-PEI-N₃ were easily dissolved in these solvents. However, after crosslinking, X-PEIs were intact after long-time immersion (Figure 4.5). To provide a harsher environment, DMF and NMP were heated at 150 °C for 1 h, but X-PEI remained undissolved. THF is a poor solvent but good plasticizer for PEI. Similarly, X-PEI was resistant to plasticization and kept the original shape after immersion.

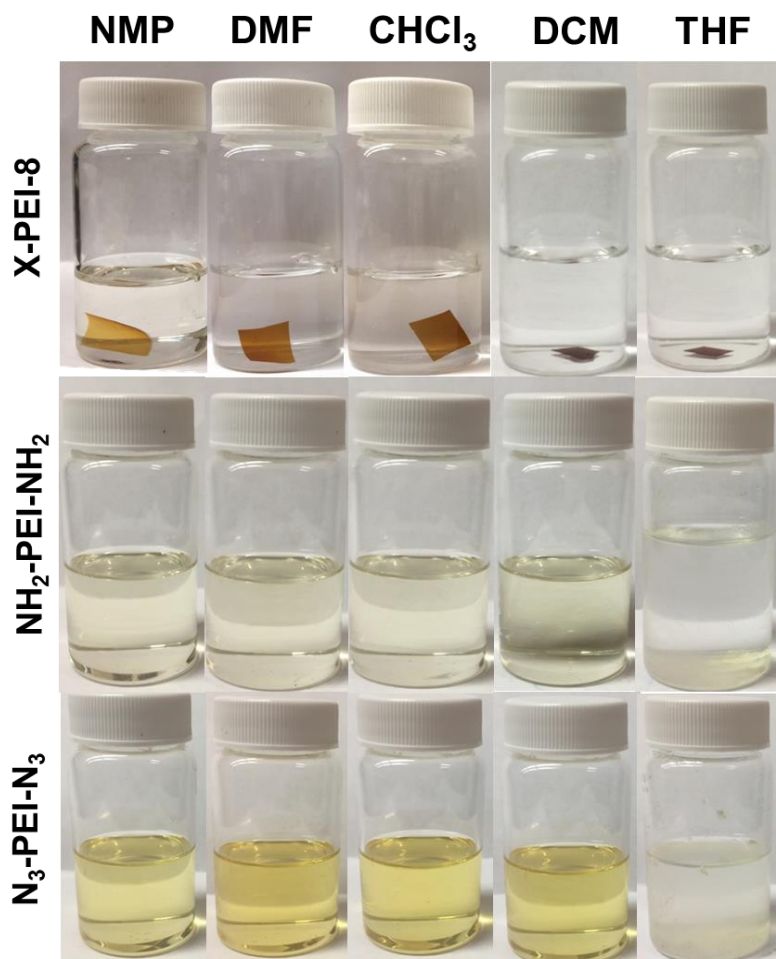


Figure 4.5 Solvent resistance of X-PEI-8 in NMP, DMF, chloroform, DCM, and THF. X-PEI-8 was resistant to all solvents, while the noncrosslinked $\text{NH}_2\text{-PEI-NH}_2$ and $\text{N}_3\text{-PEI-N}_3$ were soluble in NMP, DMF, chloroform, and DCM, and softened in THF.

To quantify the solvent resistance, X-PEIs and Ultem 1010 were exposed to DCM, chloroform, THF, methanol, and hexanes to measure vapor uptake using QCM-D (Figure 4.6). The utilization of QCM-D avoided solvent evaporation of organic solvents or moisture sorption in a typical immersion test, which provides more precise results. Ultem 1010 showed the highest swelling ratio of $\sim 40\%$ in DCM, chloroform, and THF (Table 4.2). The sorption kinetics differed drastically, and the sorption time ranged from ~ 5 min in DCM and chloroform to ~ 70 min in THF (Table 4.3 and Figure 4.6), due to (a) different affinities (or χ values) of PEI to these solvents and (b) different

diffusivities of these solvents in PEI. In a mutual diffusion system of small solvent molecules and polymer films, small χ values come with a large coefficient of mutual diffusion.⁴⁶ The good polymer-solvent affinity (small χ value) allows for adsorption of solvent molecules on the polymer chains, as well as fast diffusion of solvent molecules into the polymer films (e.g., the sorption of DCM and chloroform on PEI). As the χ value increases, although sorption still occurs, the small diffusion coefficient retards the system to reach equilibrium (e.g., the sorption of THF on PEI). When the polymer-solvent affinity is so poor that the solvent is regarded as a nonsolvent, stable sorption nor diffusion of solvent molecules barely occur in the polymer film. As the result, the polymer film reaches equilibrium quickly (e.g., the sorption of MeOH and hexanes). The swelling ratios of X-PEIs, however, were significantly lower and correlated negatively with crosslinking density. With the highest crosslinking density, X-PEI-8 had the lowest swelling ratios of 11.2, 10.4, and 4.0% in DCM, chloroform, and THF, respectively, less than half the swelling ratio of Ultem 1010. As the crosslinking density was decreased, the swelling ratios increased but remained below 26% in all test solvents.

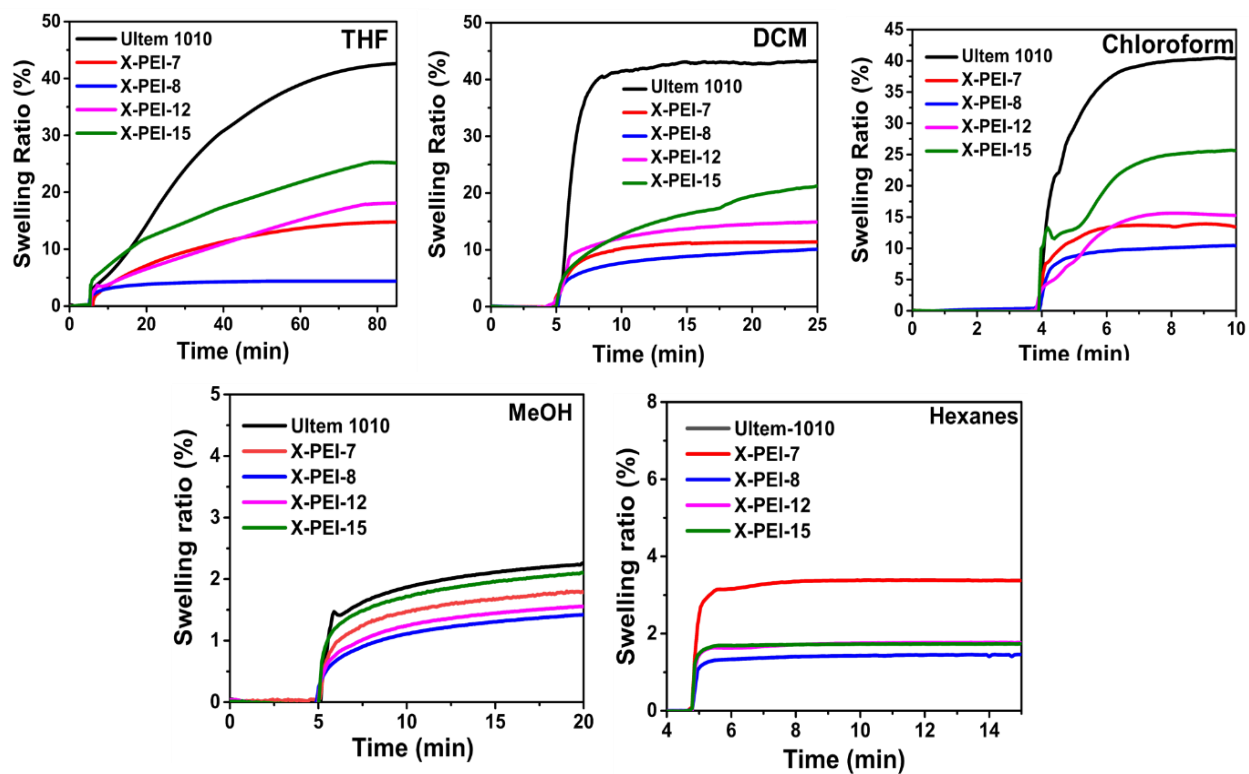


Figure 4.6 QCM-D vapor adsorption tests of THF, DCM, chloroform, hexanes, and methanol on various PEIs at 20 °C. The activities for all solvents were ~0.9.

Table 4.2 Solvent resistance of N₃-PEI-N₃ and X-PEIs.

Polymer	Swelling ratio (%)		
	CH ₂ Cl ₂	CHCl ₃	THF
X-PEI-7	13.9 ± 0.4	12.1 ± 0.7	15.7 ± 1.1
X-PEI-8	11.2 ± 0.8	10.4 ± 0.6	4.0 ± 0.3
X-PEI-12	15.3 ± 0.3	14.3 ± 1.2	19.2 ± 1.0
X-PEI-15	25.6 ± 1.1	20.8 ± 0.4	25.6 ± 1.2
Ultem 1010	40.4 ± 2.0	42.1 ± 1.5	41.3 ± 1.1

Table 4.3 Hansen solubility parameters and total solubility parameters of PEI, DCM, chloroform, and THF.

	Δ_d (Mpa ^{0.5})	δ_p (Mpa ^{0.5})	δ_h (Mpa ^{0.5})	δ_{total} (Mpa ^{0.5})	ref
PEI	21.1	7.4	7.1	23.5	47
DCM	18.2	6.3	6.1	20.2	48
Chloroform	17.8	3.1	5.7	18.9	48
THF	16.8	5.7	8.0	19.5	48

To examine the potential of using X-PEI in a solvent-rich environment, we further performed bending tests on a dry film (Figure 4.7A) and chloroform-saturated films (Figure 4.7B and C). Upon bending, the dry X-PEI-8 film was flexible and intact. The film was then immersed in CHCl₃ for 1 h. To avoid solvent evaporation from the X-PEI-8 film, the solvent saturated film was bent in CHCl₃ (Figure 4.7B), and it remained intact. Afterwards, the film was taken out of the solvent and bent again in the air (Figure 4.7C). The X-PEI-8 film showed no visible damage after bending. Therefore, X-PEI possessed good mechanical stability when saturated by a strong swelling solvent, despite the high strain exerted upon the crosslinked polymer network. Although the solvent-saturated X-PEI-8 survived the bending test, it showed reduced foldability. Dry X-PEI-8 films can be folded without noticeable damage (Figure 4.8), but the solvent-saturated X-PEI-8 film did not survive the folding test (Figure 4.9). Due to swelling-induced tension, the maximum amount of strain that X-PEI-8 can tolerate has been compromised.

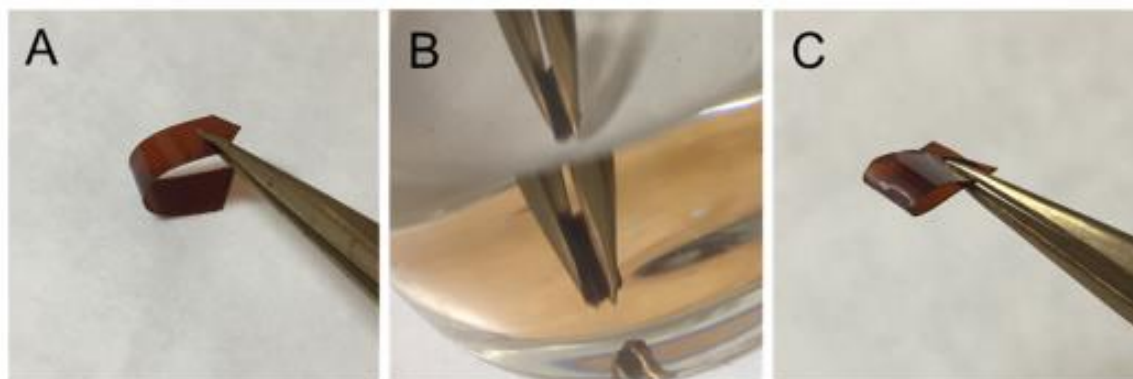


Figure 4.7 Bending test of an X-PEI-8 film (A) in a dry state, (B) immersed in CHCl_3 and saturated by the solvent, and (C) saturated by CHCl_3 but out of the solvent.



Figure 4.8 Flexibility test of $\text{N}_3\text{-PEI-N}_3\text{-7}$ and X-PEI-7 (top) Before crosslinking, $\text{N}_3\text{-PEI-N}_3\text{-7}$ cannot form intact films by solution casting. (Bottom) After crosslinking, X-PEI-7 film showed drastically improved flexibility. The film remained intact after abusive folding, stretching, and tension.

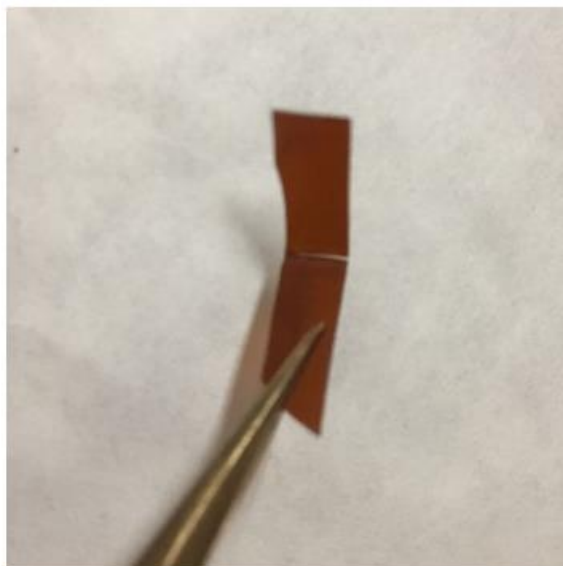


Figure 4.9 Upon folding, X-PEI-8 film saturated by CHCl_3 showed a crack near the folding line.

4.5 Conclusions

In this work, X-PEIs were prepared from $\text{N}_3\text{-PEI-N}_3$ via a simple thermal crosslinking method. Despite the much lower molecular weights of oligomer precursors, X-PEIs possessed higher T_g and storage moduli than high-molecular-weight Ultem 1010. More importantly, X-PEIs exhibited outstanding solvent-resistance to common organic solvents of PEI, including NMP, DMF, chloroform, and DCM, and X-PEIs were insoluble in all solvents tested. The competing effects between $\text{N}_3\text{-PEI-N}_3$ molecular weight and relative azide concentration determined that $\text{N}_3\text{-PEI-N}_3\text{-8}$ had the highest crosslinking density with the best physical properties (highest T_g , storage modulus, and solvent resistance). This work presents a simple and efficient method to prepare the first solvent-resistant and yet processing friendly PEI from oligomers. This approach is applicable to porous polymers and can be useful in different areas, such as battery separators,⁴⁶ fuel cell membranes,⁴⁹ and gas separation membranes.⁵⁰

4.6 References

1. Xu, Z.; Croft, Z. L.; Guo, D.; Cao, K.; Liu, G., Recent development of polyimides: Synthesis, processing, and application in gas separation. *J. Polym. Sci.* **2021**, *59*, 943-962.
2. Wang, G.; Weng, Y.; Chu, D.; Xie, D.; Chen, R., Preparation of alkaline anion exchange membranes based on functional poly(ether-imide) polymers for potential fuel cell applications. *J. Membrane Sci.* **2009**, *326*, 4-8.
3. Liu, S.; Wang, L.; Ding, Y.; Liu, B.; Han, X.; Song, Y., Novel sulfonated poly (ether ether keton)/polyetherimide acid-base blend membranes for vanadium redox flow battery applications. *Electrochim. Acta* **2014**, *130*, 90-96.
4. Cao, K.; Zhang, M.; Liu, G., The Effect of End Group and Molecular Weight on the Yellowness of Polyetherimide. *Macromol. Rapid. Commun.* **2018**, *39*, e1800045.
5. Huang, J.; Zhu, Z.; Yin, J.; Qian, X.; Sun, Y., Poly(etherimide)/montmorillonite nanocomposites prepared by melt intercalation: morphology, solvent resistance properties and thermal properties. *Polymer* **2001**, *42*, 873-877.
6. Cao, K.; Liu, G., Low-molecular-weight, high-mechanical-strength, and solution-processable telechelic poly (ether imide) end-capped with ureidopyrimidinone. *Macromolecules* **2017**, *50*, 2016-2023.
7. Rusli, A.; Raffi, N. S. M.; Ismail, H., Solubility, miscibility and processability of thermosetting monomers as reactive plasticizers of polyetherimide. *Procedia Chem.* **2016**, *19*, 776-781.
8. Blanco, I.; Cicala, G.; Ognibene, G.; Rapisarda, M.; Recca, A., Thermal properties of polyetherimide/polycarbonate blends for advanced applications. *Polym. Degrad. Stabil.* **2018**, *154*, 234-238.

9. Ramiro, J.; Eguiazábal, J. I.; Nazábal, J., Structure and mechanical properties of blends of poly(ether imide) and an amorphous polyamide. *Eur. Polym. J.* **2006**, *42*, 458-467.
10. Su, C. C.; Shih, C. K., Miscibility and transesterification in ternary blends of poly(ethylene naphthalate)/poly(pentamethylene terephthalate)/poly(ether imide). *J. Appl. Polym. Sci.* **2006**, *100*, 3840-3849.
11. Vallejo, F. J.; Eguiazábal, J. I.; Nazábal, J., Solid state features and mechanical properties of PEI/PBT blends. *J. Appl. Polym. Sci.* **2001**, *80*, 885-892.
12. Ramiro, J.; Eguiazabal, J. I.; Nazabal, J., Synergistic mechanical behaviour and improved processability of poly(ether imide) by blending with poly(trimethylene terephthalate). *Polym. Adv. Technol.* **2003**, *14*, 129-136.
13. Granado, A.; Eguiazábal, J. I.; Nazábal, J. J. M. M.; Engineering, Processability, Structure and Mechanical Properties of Poly(ether imide)/Amorphous Copolyester Blends. *Macromol. Mater. Eng.* **2010**, *295*, 476-483.
14. Cao, K.; Guo, Y.; Zhang, M.; Arrington, C. B.; Long, T. E.; Odle, R. R.; Liu, G., Mechanically strong, thermally stable, and flame retardant poly(ether imide) terminated with phosphonium bromide. *Macromolecules* **2019**, *52*, 7361-7368.
15. Cao, K.; Serrano, J. M.; Liu, T. Y.; Stovall, B. J.; Xu, Z.; Arrington, C. B.; Long, T. E.; Odle, R. R.; Liu, G. L., Impact of metal cations on the thermal, mechanical, and rheological properties of telechelic sulfonated polyetherimides. *Polym. Chem.* **2020**, *11*, 393-400.
16. Mushtaq, N.; Chen, G. F.; Sidra, L. R.; Liu, Y.; Fang, X. Z., Synthesis and crosslinking study of isomeric poly(thioether ether imide)s containing pendant nitrile and terminal phthalonitrile groups. *Polym. Chem.* **2016**, *7*, 7427-7435.

17. Yoo, T.; Kim, K.; Han, P.; Jang, W.; Han, H., Norbornene end-capped polyimide for low CTE and low residual stress with changes in the diamine linkages. *Macromol. Res.* **2015**, *23*, 776-786.
18. Jung, M. S.; Joo, W. J.; Kwon, O.; Sohn, B. H.; Jung, H. T., A high-performance positive-working photosensitive polyimide: Effects of reactive end groups on the physical properties of the films. *J. Appl. Polym. Sci.* **2006**, *102*, 2180-2188.
19. Liu, C.; Wang, J. Y.; Lin, E. C.; Zong, L. S.; Jian, X. G., Synthesis and properties of phthalonitrile-terminated oligomeric poly(ether imide)s containing phthalazinone moiety. *Polym. Degrad. Stab.* **2012**, *97*, 460-468.
20. Kratochvil, A. M.; Koros, W. J., Decarboxylation-Induced Cross-Linking of a Polyimide for Enhanced CO₂ Plasticization Resistance. *Macromolecules* **2008**, *41*, 7920-7927.
21. Lu, Y. X.; Tournilhac, F.; Leibler, L.; Guan, Z., Making insoluble polymer networks malleable via olefin metathesis. *J. Am. Chem. Soc.* **2012**, *134*, 8424-8427.
22. Shen, J.; Lin, X.; Liu, J.; Li, X., Effects of cross-link density and distribution on static and dynamic properties of chemically cross-linked polymers. *Macromolecules* **2018**, *52*, 121-134.
23. Liu, C.; Lin, E. C.; Zong, L. S.; Liu, C. D.; Yu, G. P.; Wang, J. Y.; Hu, F. Y.; Weng, Z. H.; Jian, X. G., Phthalonitrile-functionalized poly(ether imide) oligomers derived from phthalazinone-containing dianhydride: facile synthesis, curing and properties. *Polym. Bulletin.* **2018**, *75*, 1037-1054.
24. Rosu, L.; Sava, I.; Rosu, D., Modification of the surface properties of a polyimide film during irradiation with polychromic light. *Appl. Surf. Sci.* **2011**, *257*, 6996-7002.
25. Han, S. S.; Im, S. S.; Won, J. C.; Lee, J. H.; Choi, K. Y.; Kim, Y. S., Synthesis and characterization of new polyimides containing ethynylene linkages. *Eur. Polym. J.* **2007**, *43*, 1541-1548.

26. Tillet, G.; Boutevin, B.; Ameduri, B., Chemical reactions of polymer crosslinking and post-crosslinking at room and medium temperature. *Prog. Polym. Sci.* **2011**, *36*, 191-217.
27. Bai, Y.; Song, N.; Gao, J. P.; Sun, X.; Wang, X.; Yu, G.; Wang, Z. Y., A new approach to highly electrooptically active materials using cross-linkable, hyperbranched chromophore-containing oligomers as a macromolecular dopant. *J. Am. Chem. Soc.* **2005**, *127*, 2060-2061.
28. Tashvigh, A. A.; Feng, Y. N.; Weber, M. R. T.; Maletzko, R. T.; Chung, T. S., 110th Anniversary: Selection of Cross-Linkers and Cross-Linking Procedures for the Fabrication of Solvent-Resistant Nanofiltration Membranes: A Review. *Ind. Eng. Chem. Res.* **2019**, *58*, 10678-10691.
29. Xia, Y.; Verduzco, R.; Grubbs, R. H.; Kornfield, J. A., Well-defined liquid crystal gels from telechelic polymers. *J. Am. Chem. Soc.* **2008**, *130*, 1735-1740.
30. Powell, C. E.; Duthie, X. J.; Kentish, S. E.; Qiao, G. G.; Stevens, G. W., Reversible diamine cross-linking of polyimide membranes. *J. Membr. Sci.* **2007**, *291*, 199-209.
31. Li, G.; Wang, H.; Zheng, H.; Bai, R., Room-temperature RAFT copolymerization of 2-chloroallyl azide with methyl acrylate and versatile applications of the azide copolymers. *J. Polym. Sci. A: Polym. Chem.* **2010**, *48*, 1348-1356.
32. Gao, C.; He, H.; Zhou, L.; Zheng, X.; Zhang, Y., Scalable Functional Group Engineering of Carbon Nanotubes by Improved One-Step Nitrene Chemistry. *Chem. Mater.* **2009**, *21*, 360-370.
33. Nyffeler, P. T.; Liang, C. H.; Koeller, K. M.; Wong, C. H., The chemistry of amine-azide interconversion: catalytic diazotransfer and regioselective azide reduction. *J. Am. Chem. Soc.* **2002**, *124*, 10773-10778.
34. Fehlhammer, W. P.; Beck, W., Azide chemistry—an inorganic perspective, Part I metal azides: overview, general trends and recent developments. *Z. Anorg. Allg. Chem.* **2013**, *639*, 1053-1082.

35. Cao, K.; Xu, Z.; Guo, D.; Liu, G. L., Poly(ether imide)s with tailored end groups. *J. Polym. Sci.* **2021**, *59*, 2365-2377.
36. Grissom, T. G.; Serrine, J. M.; Long, T. E.; Esker, A. R.; Morris, J. R., Interaction parameters for the uptake of sulfur mustard mimics into polyurethane films. *Prog. Org. Coat.* **2017**, *107*, 14-17.
37. Kim, D.; Park, K., Swelling and mechanical properties of superporous hydrogels of poly(acrylamide-co-acrylic acid)/polyethylenimine interpenetrating polymer networks. *Polymer* **2004**, *45*, 189-196.
38. Reviakine, I.; Johannsmann, D.; Richter, R. P., Hearing What You Cannot See and Visualizing What You Hear: Interpreting Quartz Crystal Microbalance Data from Solvated Interfaces. *Anal. Chem.* **2011**, *83*, 8838-8848.
39. Burdzinski, G.; Hackett, J. C.; Wang, J.; Gustafson, T. L.; Hadad, C. M.; Platz, M. S., Early events in the photochemistry of aryl azides from femtosecond UV/Vis spectroscopy and quantum chemical calculations. *J. Am. Chem. Soc.* **2006**, *128*, 13402-13411.
40. Cao, K.; Zhang, M.; Liu, G., The effect of end group and molecular weight on the yellowness of polyetherimide. *Macromol. Rapid Commun.* **2018**, *39*, e1800045.
41. Huang, D. Y.; Yan, G. B., Recent Advances in Reactions of Azides. *Adv. Synth. Catal.* **2017**, *359*, 1600-1619.
42. Pandurangi, R. S.; Karra, S. R.; Katti, K. V.; Kuntz, R. R.; Volkert, W. A., Chemistry of Bifunctional Photoprobes. 1. Perfluoroaryl Azido Functionalized Phosphorus Hydrazides as Novel Photoreactive Heterobifunctional Chelating Agents: High Efficiency Nitrene Insertion on Model Solvents and Proteins. *J. Org. Chem.* **1997**, *62*, 2798-2807.

43. Li, Y. Z.; Kirby, J. P.; George, M. W.; Poliakoff, M.; Schuster, G. B., 1,2-Didehydroazepines from the Photolysis of Substituted Aryl Azides - Analysis of Their Chemical and Physical-Properties by Time-Resolved Spectroscopic Methods. *J. Am. Chem. Soc.* **1988**, *110*, 8092-8098.
44. Taranekar, P.; Fulghum, T.; Patton, D.; Ponnampati, R.; Clyde, G.; Advincula, R., Investigating carbazole jacketed precursor dendrimers: sonochemical synthesis, characterization, and electrochemical crosslinking properties. *J. Am. Chem. Soc.* **2007**, *129*, 12537-12548.
45. Herrmann-Schönherr, O.; Schneller, A.; Seifert, A. M.; Soliman, M.; Wendorff, J. H., Chain dimensions, entanglement molecular weights and molecular weight distributions of poly (aryl ethers). A combined rheological and MNDO analysis. *Makromol. Chem.* **1992**, *193*, 1955-1974.
46. Wu, J. Y.; Yuan, L. X.; Zhang, W. X.; Li, Z.; Xie, X. L.; Huang, Y. H., Reducing the thickness of solid-state electrolyte membranes for high-energy lithium batteries. *Energ. Environ. Sci.* **2021**, *14*, 12-36.
47. Tan, M.; He, G.; Dai, Y.; Wang, R.; Shi, W., Calculation on phase diagrams of polyetherimide/N, N-dimethylacetamide/H₂O-BuOH casting system and their relevance to membrane performances. *Front. Chem. Sci.* **2014**, *8*, 312-319.
48. Hansen, C. M., *Hansen solubility parameters: a user's handbook*. CRC press: 2007.
49. Gao, X. Q.; Yu, H. M.; Xie, F.; Hao, J. K.; Shao, Z. G., High performance cross-linked anion exchange membrane based on aryl-ether free polymer backbones for anion exchange membrane fuel cell application. *Sustain. Energy Fuels* **2020**, *4*, 4057-4066.
50. Liu, T.; Liu, G., Porous organic materials offer vast future opportunities. *Nat. Commun.* **2020**, *11*, 1-3.

Chapter 5: Investigation of Photo-oxidative Aging in Semi-Crystalline Polymers based upon Chemical Characterization Techniques

Part of this chapter is adapted from a manuscript submitted to International Journal of Solids and Structures. Full text of the submitted manuscript, entitled “*Physics-based Constitutive Modeling of Photo-oxidative Aging in Semi-Crystalline Polymers based on Chemical Characterization Techniques*” by Aimane Najmeddine, Zhen Xu, Gehui Liu; Zacary L. Croft, Guoliang (Greg) Liu, Alan R. Esker, and Maryam Shakiba.

5.1 Abstract

Photo-oxidation, induced by exposure to ultra-violet (UV) light and oxygen, is one of the dominant degradation mechanisms affecting the lifespan of polymers. In this work, we characterized the physiochemical changes of low-density polyethylene (LDPE) to understand the photo-oxidation degradation process. The evolution of a macroscopic property, mechanical properties, was characterized by tensile stress-strain experiments. Materials after aging showed improved tensile stress and modulus, with reduced elongation property. The observation was further investigated using microscopic techniques including DSC and QCM-D to reveal the changes in crystallinity and mass loss, respectively. QCM-D showed good accuracy for monitoring the evolution of mass change during aging process and provided support to the mechanical performance, which demonstrated the potential of QCM-D as an efficient technique for monitoring the minute mass loss of plastic during aging. This work shed light on the evolution of the macromolecular network in LDPE under extreme photo-oxidation conditions and the evolution of associated mechanical properties of materials.

5.2 Introduction

In the past decades, semi-crystalline polymers have wide applications in different areas including automotive and aerospace industries, electrical insulation technologies, and thermal storage applications due to their excellent mechanical performances and optimal strength-to-weight ratio.¹⁻² Through their service life, semi-crystalline polymers exposed to complex environmental conditions, such as ultra-violet (UV) light, heat, mechanical, and chemical processes (Figure 5.1). These environmental factors can slowly degrade polymers and thus degenerate their mechanical properties, resulting in permanent failure. Among these factors, UV light emitted by the sun and other artificial light sources are the most common factor of plastic degradation in nature.³⁻⁵ The presence of oxygen in addition to UV light accelerates the photodegradation of polymer materials and this process is known as photo-oxidation.⁶ The resistance of polymers to photo-oxidation depends upon the polymer composition, possible inherent contaminants, and the inclusion of pigments, additives, or fillers.⁷⁻⁹ For instance, polymers with weak bond energies and a high density of chromophores (i.e., chemical groups that are capable of absorbing light) are more susceptible to photo-oxidation.¹⁰

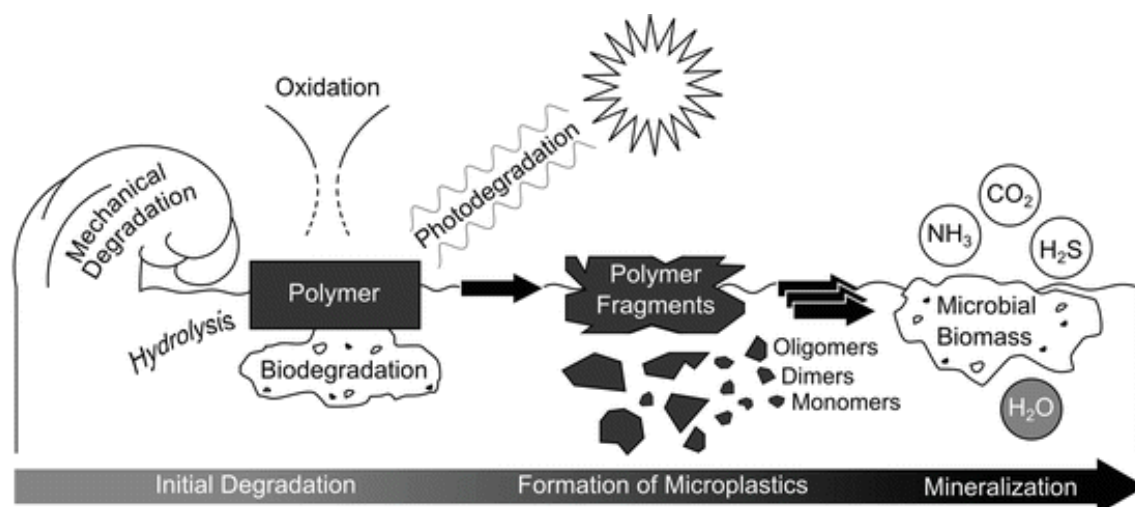


Figure 5.1 Degradation pathways of synthetic polymers under environmental factors. Reproduced from Knepper et al. (Copyright 2018 Springer).¹¹

Photo-oxidation and its harmful effects on the lifespan of semi-crystalline polymers have been a research topic for decades.¹²⁻¹³ Photo-oxidation contributes to the degeneration of the structure of semi-crystalline polymers, resulting in weaker materials.¹⁴⁻¹⁷ Ultimately, photo-oxidation leads to complete material failure. In semi-crystalline polyolefins, for instance, photo-oxidation can be initiated either through hydroperoxide decomposition or through ketone photolysis via Norrish reactions.⁶ As a result of these initiators, polymers can undergo an initial period of random chain-scission followed by a secondary period of crosslinking that is responsible for surface embrittlement. Due to this embrittlement, the polymers harden, and visible cracks can potentially occur on their surface.¹⁸ Photo-oxidation reactions occur in the amorphous region of semi-crystalline polymers that is favorable to oxygen diffusion.¹⁹ Moreover, the random coil structure of the amorphous region favors dynamic chain entanglements. Therefore, when polymer is exposed to light and oxygen, photo-oxidation-induced molecular chain alterations such as chain-scission and crosslinking occur in the amorphous phase. As a result, it is obvious that structural

changes of semi-crystalline polymers induced by photo-oxidation have a direct relationship with the mechanical response of the aged polymers (i.e., embrittlement, crack initiation, propagation, etc.).²⁰⁻²¹

With brittle mechanical properties, plastics fragment easily in the ocean under mechanical stirring of wind and wave, grinding polymers into smaller particles known as microplastics.²² Due to their minuscule sizes, microplastics can travel in large amounts through water pathways into the ocean system. The microplastics accumulated in the marine environment have become a major environmental concern in today's environmental discussion.²³⁻²⁵ However, the generation of microplastic is poorly understood.²⁶⁻²⁸ The kinetics of the generation of microplastic from photo-oxidation degradation are still rarely investigated.²⁹ Moreover, effects of polymer composition on the microplastic evolution, such as polymer crystallinity, crosslinking density, and morphologies, are poorly understood.³⁰ The major difficulty of micro/nanoplastic investigation is the lack of sensitive analytical methods and instrumentation.³¹⁻³⁴ Due to the small size and massive number of nanoplastic, continuous monitoring of plastic degradation is difficult by microscopes and analytical balances. As a real-time and label-free analytical instrument, a quartz crystal microbalance with dissipation monitoring (QCM-D) can provide information about mass and structural changes in thin films at nanoscale. Mass changes as low as 0.5 ng cm⁻² and thickness changes from 1 Å to 1 μm on the QCM-D sensor surfaces can be measured.³⁵ Due to these unique features, QCM-D is successfully used to study the degradation process of different materials with high accuracy in the literature.³⁶⁻³⁸ Therefore, QCM-D can serve as a perfect candidate to monitor the mass changes of plastic films during aging degradation process.

In this work, the mechanical performance of the polymer films during aging were investigated by tensile tests. Differential scanning calorimetry (DSC) was then employed to determine the evolution of the crystallinity of LDPE films during aging. Finally, QCM-D was used to determine the evolution of the minute mass ratio between the initial unaged thin polymer films and the corresponding aged samples. The mass loss characterizes the direct damage from photo-oxidation reactions of polymers during aging process. To our best knowledge, there is no current study that uses the mass loss evolution to quantify the degree of photo-oxidation in polymers. The introduction of QCM-D method provides an alternative solution to determine minute mass loss evolution in this research area.

5.3 Experimental Section

5.3.1 Materials

Low density polyethylene (LDPE) pellets were purchased and used as received from Sigma-Aldrich with a density of 0.93 g cm^{-2} and a melting point of $116 \text{ }^{\circ}\text{C}$. LDPE films were prepared at $180 \text{ }^{\circ}\text{C}$ for 2 min under loading of 8 tons through thermo-pressing. The resulting films were cooled down from $180 \text{ }^{\circ}\text{C}$ to room temperature in the air and were then thermally annealed at $110 \text{ }^{\circ}\text{C}$ for 1 h with a final thickness of 30 to $80 \text{ }\mu\text{m}$. The range of film thickness was designed for homogeneous oxidation and to avoid diffusion-limited-oxidation (DLO) conditions.

5.3.2 UV Aging

LDPE films were aged under a 250 W UV lamp with a wavelength of 254 nm and a maximum UV dose of 125 kW m^{-2} at room temperature to simulate the LDPE photo-oxidation in the air in a shorter time. In addition, the LDPE coated QCM-D gold sensors

were UV aged under the lamp for varying aging times (e.g., 0, 24, 48, 72, and 112 h). Compared with the solar radiation that has a UV intensity of 100 to 200 W m², the maximum aging time in this work (112 h) equals 432 days of solar radiation in the air.

5.3.3 Mechanical Testing

LDPE films were cut into dog-bone shapes and tensile tests were then performed following ASTM-D-638 standard to determine the stress-strain response before and after film aging. LDPE samples were stretched in tensile mode up to rupture at a constant strain rate of 0.004 s⁻¹ to ensure the quasi-static loading. Three parallel samples were performed for each tensile test.

5.3.4 Determination of Polymer Crystallinity by Differential Scanning Calorimetry (DSC)

DSC was conducted on a Discovery DSC2500 (TA Instruments) from 40 to 200 °C at a heating rate of 30 °C min⁻¹ under a nitrogen flow of 50 mL min⁻¹. Polymer crystallinity can be calculated using heat of fusion of LDPE from DSC divided by 293 J g⁻¹ for the 100% crystalline material. DSC characterization on LDPE films for crystallinity was performed with sample thicknesses ranging between 30 and 80 μm since the sensitivity of DSC could be low at low sample mass with thicknesses smaller than 1 μm.³⁹

5.3.5 Evolution of Mass Loss by a Quartz Crystal Microbalance with Dissipation Monitoring (QCM-D)

QCM-D was introduced to measure the minute mass ratio between the aged and unaged LDPE films in this study. Three different thicknesses of polymer films (i.e., 146, 158, and 200 nm) were prepared on QCM-D gold sensors by spin-coating to study the effect of film

thickness on the mass change, and each thickness of films had three parallel samples. The film thickness was modified by adjusting the spin-coating speed of the xylene solution with LDPE (6 wt.%) and calculated based upon the film mass from QCM-D and film density. To prevent polymer precipitation, the QCM-D sensors and LDPE solutions were heated using an IR lamp during spin-coating. LDPE coated sensors were then thermally annealed in a vacuum oven under the same conditions (*i.e.*, at 110 °C for 1 h) as bulk films before the aging experiments and QCM-D measurements. After UV aging, the LDPE coated QCM-D sensors were rinsed with deionized water to dissolve and remove the polymer fragments and subsequently dried with a gentle nitrogen flow. The QCM-D sensors were then placed in the vacuum oven at room temperature for 12 h to remove any residual moisture. Finally, the sensors were loaded into the QCM-D chamber and monitored by the system frequency changes were converted into mass changes using the Sauerbrey equation.⁴⁰

5.4 Results and Discussion

5.4.1 DSC Analysis

Data from DSC in Figure 5.2A demonstrates the evolution of the crystallinity of LDPE films for different photo-oxidation times. Under applied aging treatments, the degree of crystallinity of polymer films increased linearly with aging time. After 48 h of photo-oxidation, the crystallinity increased from the initial value of around 43% to 47% and at the end of 112 h, the crystallinity reached approximately 52%. Figure 5.2B shows the heating thermograms of LDPE films for different photo-oxidation aging times. As shown in the graph, additional endothermic shoulders appeared below the melting temperature, and this temperature is higher than the exposure temperature (25 °C). Therefore, these

results indicated that the newly formed crystallites are secondary. The increase in crystallinity contributes to a further stiffening in the polymer films after photo-oxidation. As a result, stiffness and ultimately embrittlement are significantly amplified.

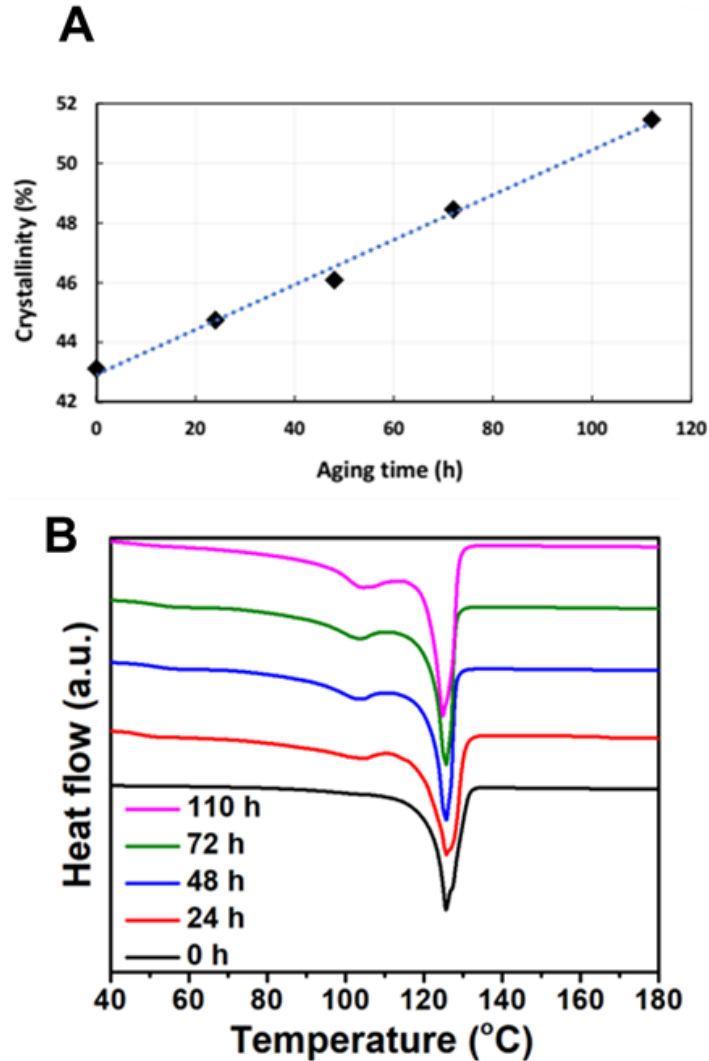


Figure 5.2 (A) Evolution of crystallinity as a function of photo-oxidation aging time obtained from DSC, (B) DSC thermograms of LDPE films with varying photo-oxidation aging times.

The trend of crystallinity change (Figure 5.3) in this work is similar to the work of Rodriguez et al.,¹⁸ while the initial crystallinity for LDPE films in our work is lower than

the work of Rodriguez et al. (i.e., 43% compared to 55%).¹⁸ Particularly, after 112 h of UV aging, our material was just as crystalline as the material used in Rodriguez et al. initially was before any UV exposure. This unique difference in the measured initial crystallinity may have a significant contribution to the differences observed in the mechanical performance of unaged and aged samples between our work and the work by Rodriguez et al.¹⁸

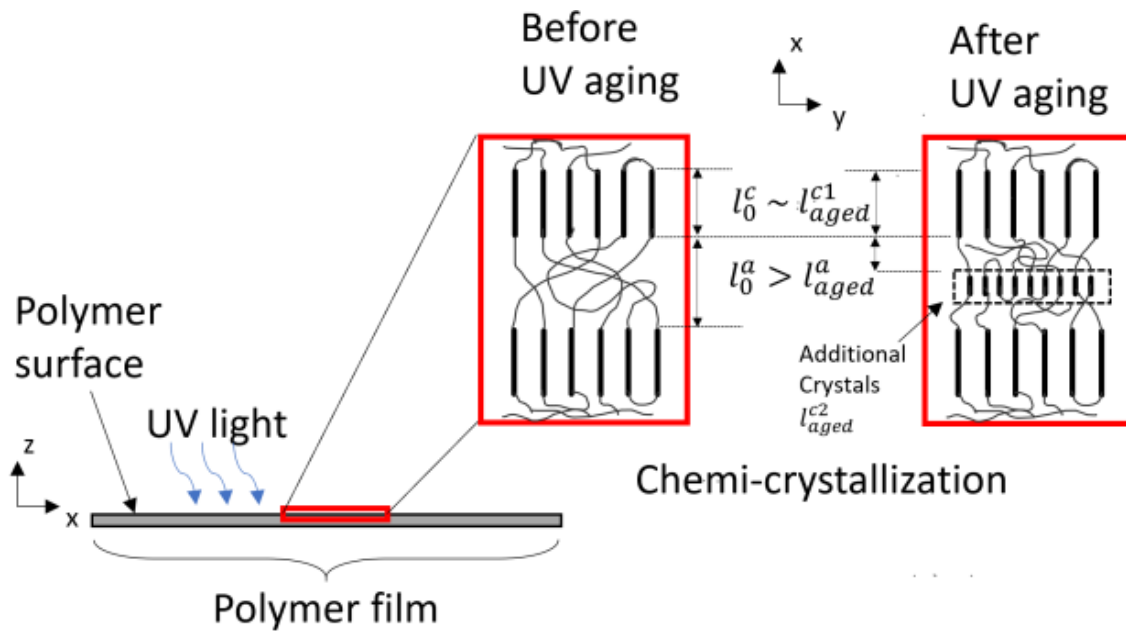


Figure 5.3 Schematic representation of chemi-crystallization due to photo-oxidation. Upon exposure to UV light, the molecular chains in the amorphous region break and degrade causing the formation of additional crystals within the amorphous domain.

5.4.2 QCM-D Measurements

Figure 5.4 demonstrates the evolution of the minute mass ratio for three different LDPE film thicknesses as a function of aging time measured by QCM-D. Samples showed considerable weight loss after 112 h of UV aging with a UV intensity of 125 kW m^{-2} . The 200-nm-thick film underwent almost 5% weight loss after 120 h UV aging and the other

two thinner films experienced more weight loss up to 15% after the same aging time. The weight loss of the LDPE film after UV aging indicated damage of polymer chain integrity, compromising the stability of the film. The loss of weight may be attributed to two reasons: 1) small hydrophilic molecules produced from PE photo-degradation (*e.g.*, alcohol, alkane and ketone), and 2) micro- or nanoplastics formed from film fragmentation. Indeed, microplastics are found in large amounts mainly due to plastic-fragmentation caused by the exposure to environmental perturbations such as UV irradiation.⁴¹

Obtaining the minute mass loss evolution functions is challenging due to the minor weight loss which is negligible for thick polymer films. Therefore, the introduction of a thin film is an optimal solution to accurately monitor the mass loss during the aging process. However, the issue with thin films is that the thickness effect on the film behavior is considerable. For example, the film thickness has a significant effect on T_g of polymers when the thickness is around 100 nm owing to the increased surface effect of thin films.⁴² As a result, consider the negligible mass loss for thick films and the thickness effects on thermal properties for thin films, LDPE films with thickness less than 1 μm but greater than 100 nm were selected to amplify the mass loss during the aging process and at the same time accurately monitor the mass change.

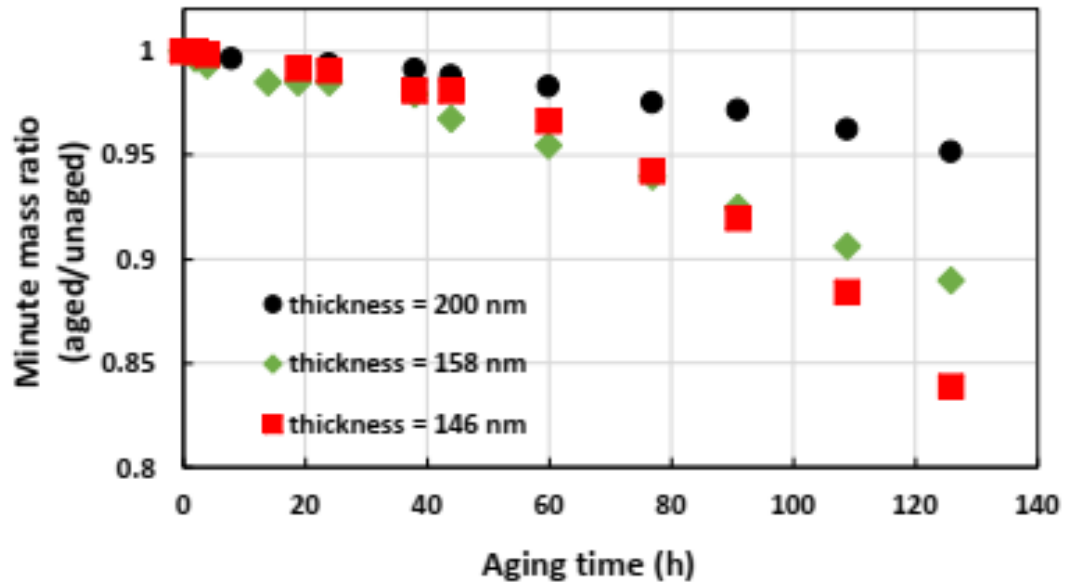


Figure 5.4 Evolution of the minute mass ratio between the aged and unaged samples as a function of photo-oxidation aging time obtained from the QCM-D test. The minute mass ratio is presented for three film thicknesses: 200 nm, 158 nm, and 146 nm represented by circles, diamonds, and squares, respectively.

5.4.3 Mechanical testing

Tensile stress-strain curves for LDPE films were obtained for aging times from 0 to 112 h in this work. Three parallel samples were measured for each aging time and the averages were taken and plotted in Figure 5.5. As is shown, both initial stiffness and the yield stress increased with the increase of aging times. However, the films displayed a significant reduction in elongation. These phenomena could be explained by the chemo-crystallization and chain crosslinking for the increase in the initial stiffness and yield stress and the reduction in the molecular weight for the decrease in elongation, which was consistent with DSC traces and QCM-D data. On one hand, the expansion of the crystalline domain after aging obtained from DSC demonstrates the enhanced initial stiffness and

yield stress. On the other hand, the minute mass loss determined by QCM-D indicates LDPE degradation during photo-oxidation. This reduces chain integrity and affects the mechanical performance, resulting in a substantial decrease in material elongation over exposure time. Although the weight loss in bulk polymer films may not be comparable with that in thin films spin-coated on the QCM-D sensors, the loss of chain integrity after photo-oxidation is expected to be comparable due to good UV light transmittance in LDPE. Therefore, except for the crystallinity change determined by DSC, the elongation change after photo-oxidation can also be explained by the mass loss measured by QCM-D.

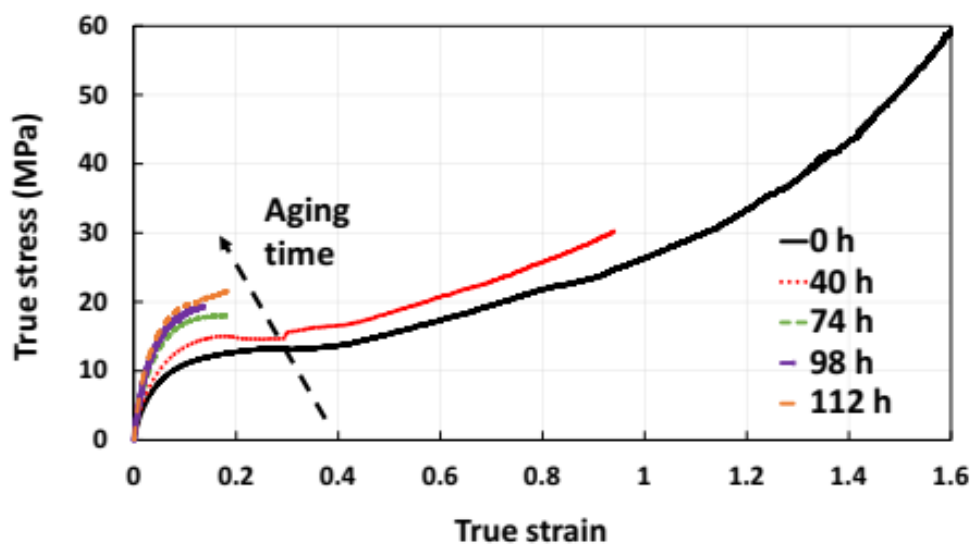


Figure 5.5 Average stress-strain curves from each LDPE film with three replicates corresponding to different aging times (i.e., 0, 40, 74, 98, and 112 h).

5.5 Conclusions

In this work, the potential of QCM-D for monitoring plastic film aging effect is evaluated. The minute mass change of PE under UV aging was monitored by QCM-D and showed good accuracy. PE degraded slowly and generated water-soluble small molecules and fragmented plastic pieces during UV aging, causing mass changes and polymer

damage. Compared with the macroscopic mechanical characterization of the aged LDPE films, QCM-D provided strong supporting evidence for the formation of nanoplastics. For example, along with the UV aging, LDPE weight loss and film integrity was compromised, resulting in weaker mechanical properties. The changes in the mass of the material under aging may bridge the gap between molecular network evolution and its effect on the overall macroscopic mechanical changes, which previously cannot be observed easily by conventional techniques such as an analytical balance, microscopes, Fourier-transform infrared spectroscopy, Raman spectroscopy, DSC, thermal gravimetric analysis. Therefore, QCM-D is a highly applicable tool in the PE aging study with great accuracy.

5.6 References

1. Ning, N. Y.; Fu, S. R.; Zhang, W.; Chen, F.; Wang, K.; Deng, H.; Zhang, Q.; Fu, Q., Realizing the enhancement of interfacial interaction in semicrystalline polymer/filler composites via interfacial crystallization. *Prog. Polym. Sci.* **2012**, *37*, 1425-1455.
2. Bigg, D. M., Mechanical property enhancement of semicrystalline polymers-A review. *Polym. Eng. Sci.* **1988**, *28*, 830-841.
3. Yousif, E.; Haddad, R., Photodegradation and photostabilization of polymers, especially polystyrene: review. *Springerplus* **2013**, *2*, 1-32.
4. Ranjan, V. P.; Goel, S., Degradation of Low-Density Polyethylene Film Exposed to UV Radiation in Four Environments. *J. Hazard. Toxic Radio.* **2019**, *23*, 04019015.
5. Guo, X.; Wang, J., The chemical behaviors of microplastics in marine environment: A review. *Mar. Pollut. Bull.* **2019**, *142*, 1-14.
6. Rabek, J. F., *Polymer photodegradation: mechanisms and experimental methods*. Springer Science & Business Media: 1994.

7. Feldman, D., Polymer weathering: Photo-oxidation. *J. Polym. Environ.* **2002**, *10*, 163-173.
8. Mistretta, M. C.; Fontana, P.; Ceraulo, M.; Morreale, M.; La Mantia, F. P., Effect of compatibilization on the photo-oxidation behaviour of polyethylene/polyamide 6 blends and their nanocomposites. *Polym. Degrad. Stabil.* **2015**, *112*, 192-197.
9. Dintcheva, N. T.; La Mantia, F. P.; Malatesta, V., Photo-oxidation behaviour of polyethylene/multi-wall carbon nanotube composite films. *Polym. Degrad. Stabil.* **2009**, *94*, 162-170.
10. Dintcheva, N. T.; Filippone, G.; La Mantia, F. P.; Acierno, D., Photo-oxidation behaviour of polyethylene/polyamide 6 blends filled with organomodified clay: Improvement of the photo-resistance through morphology modification. *Polym. Degrad. Stabil.* **2010**, *95*, 527-535.
11. Klein, S.; Dimzon, I. K.; Eubeler, J.; Knepper, T. P., Analysis, Occurrence, and Degradation of Microplastics in the Aqueous Environment. In *Freshwater Microplastics*, Wagner, M.; Lambert, S., Eds. Springer International Publishing: Cham, 2018; pp 51-67.
12. Cundiff, K. N.; Madi, Y.; Benzerga, A. A., Photo-oxidation of semicrystalline polymers: Damage nucleation versus growth. *Polymer* **2020**, *188*, 122090.
13. Yakimets, I.; Lai, D. W.; Guigon, M., Effect of photo-oxidation cracks on behaviour of thick polypropylene samples. *Polym. Degrad. Stab.* **2004**, *86*, 59-67.
14. Hsu, Y. C.; Weir, M. P.; Truss, R. W.; Garvey, C. J.; Nicholson, T. M.; Halley, P. J., A fundamental study on photo-oxidative degradation of linear low density polyethylene films at embrittlement. *Polymer* **2012**, *53*, 2385-2393.

15. Celina, M. C., Review of polymer oxidation and its relationship with materials performance and lifetime prediction. *Polym. Degrad. Stabil.* **2013**, *98*, 2419-2429.
16. Julienne, F.; Lagarde, F.; Delorme, N., Influence of the crystalline structure on the fragmentation of weathered polyolefines. *Polym. Degrad. Stabil.* **2019**, *170*, 109012.
17. Hedir, A.; Moudoud, M.; Lamrous, O.; Rondot, S.; Jbara, O.; Dony, P., Ultraviolet radiation aging impact on physicochemical properties of crosslinked polyethylene cable insulation. *J. Appl. Polym. Sci.* **2020**, *137*, 48575.
18. Rodriguez, A. K.; Mansoor, B.; Ayoub, G.; Colin, X.; Benzerga, A. A., Effect of UV-aging on the mechanical and fracture behavior of low density polyethylene. *Polym. Degrad. Stabil.* **2020**, *180*, 109185.
19. Ayoub, G.; Rodriguez, A. K.; Mansoor, B.; Colin, X., Modeling the visco-hyperelastic–viscoplastic behavior of photodegraded semi-crystalline low-density polyethylene films. *Int. J. Solids Struct.* **2020**, *204*, 187-198.
20. Bottino, F. A.; Cinquegrani, A. R.; G., D. P.; Leonardi, L.; Pollicino, A., Chemical modifications, mechanical properties and surface photo-oxidation of films of polystyrene (PS). *Polym. Test.* **2004**, *23*, 405-411.
21. Suresh, B.; Maruthamuthu, S.; Kannan, M.; Chandramohan, A., Mechanical and surface properties of low-density polyethylene film modified by photo-oxidation. *Polym. J.* **2011**, *43*, 398-406.
22. Andrady, A. L., The plastic in microplastics: A review. *Mar. Pollut. Bull.* **2017**, *119*, 12-22.

23. Brandon, J.; Goldstein, M.; Ohman, M. D., Long-term aging and degradation of microplastic particles: Comparing in situ oceanic and experimental weathering patterns. *Mar. Pollut. Bull.* **2016**, *110*, 299-308.
24. Da Costa, J. P.; Nunes, A. R.; Santos, P. S.; Girao, A. V.; Duarte, A. C.; Rocha-Santos, T., Degradation of polyethylene microplastics in seawater: Insights into the environmental degradation of polymers. *J. Environ. Sci. Health A* **2018**, *53*, 866-875.
25. Bergmann, M.; Mutzel, S.; Primpke, S.; Tekman, M. B.; Trachsel, J.; Gerdt, G., White and wonderful? Microplastics prevail in snow from the Alps to the Arctic. *Sci. Adv.* **2019**, *5*, eaax1157.
26. Mendoza, L. M. R.; Karapanagioti, H.; Álvarez, N. R., Micro (nanoplastics) in the marine environment: current knowledge and gaps. *Curr. Opin. Environ. Sci. Health* **2018**, *1*, 47-51.
27. Kalogerakis, N.; Karkanorachaki, K.; Kalogerakis, G. C.; Triantafyllidi, E. I.; Gotsis, A. D.; Partsinevelos, P.; Fava, F., Microplastics Generation: Onset of Fragmentation of Polyethylene Films in Marine Environment Mesocosms. *Front. Mar. Sci.* **2017**, *4*, 84-89.
28. Andrady, A. L., Microplastics in the marine environment. *Mar. Pollut. Bull.* **2011**, *62*, 1596-1605.
29. Lambert, S.; Wagner, M., Characterisation of nanoplastics during the degradation of polystyrene. *Chemosphere* **2016**, *145*, 265-268.
30. Hebner, T. S.; Maurer-Jones, M. A., Characterizing microplastic size and morphology of photodegraded polymers placed in simulated moving water conditions. *Environ. Sci. Process Impacts* **2020**, *22*, 398-407.

31. Xu, J. L.; Thomas, K. V.; Luo, Z.; Gowen, A. A., FTIR and Raman imaging for microplastics analysis: State of the art, challenges and prospects. *Trends Analyt. Chem.* **2019**, *119*, 115629.
32. Tian, L.; Chen, Q.; Jiang, W.; Wang, L.; Xie, H.; Kalogerakis, N.; Ma, Y.; Ji, R., A carbon-14 radiotracer-based study on the phototransformation of polystyrene nanoplastics in water versus in air. *Environ. Sci. Nano* **2019**, *6*, 2907-2917.
33. Dehaut, A.; Hermabessiere, L.; Duflos, G., Current frontiers and recommendations for the study of microplastics in seafood. *Trends Analyt. Chem.* **2019**, *116*, 346-359.
34. Phuong, N. N.; Zalouk-Vergnoux, A.; Poirier, L.; Kamari, A.; Châtel, A.; Mouneyrac, C.; Lagarde, F., Is there any consistency between the microplastics found in the field and those used in laboratory experiments? *Environ. Pollut.* **2016**, *211*, 111-123.
35. Handley, J., Product review: quartz crystal microbalances. ACS Publications: 2001.
36. Wang, C.; Kittle, J. D.; Qian, C.; Roman, M.; Esker, A. R., Chitinase activity on amorphous chitin thin films: a quartz crystal microbalance with dissipation monitoring and atomic force microscopy study. *Biomacromolecules* **2013**, *14*, 2622-2628.
37. Turon, X.; Rojas, O. J.; Deinhammer, R. S., Enzymatic kinetics of cellulose hydrolysis: a QCM-D study. *Langmuir* **2008**, *24*, 3880-3887.
38. Suchy, M.; Linder, M. B.; Tammelin, T.; Campbell, J. M.; Vuorinen, T.; Kontturi, E., Quantitative Assessment of the Enzymatic Degradation of Amorphous Cellulose by Using a Quartz Crystal Microbalance with Dissipation Monitoring. *Langmuir* **2011**, *27*, 8819-8828.

39. Wang, Y.; Ge, S.; Rafailovich, M.; Sokolov, J.; Zou, Y.; Ade, H.; Lüning, J.; Lustiger, A.; Maron, G., Crystallization in the thin and ultrathin films of Poly (ethylene–vinyl acetate) and Linear Low-Density Polyethylene. *Macromolecules* **2004**, *37*, 3319-3327.
40. Sauerbrey, G. J. Z. P., The use of quarts oscillators for weighing thin layers and for microweighing. *Z. Phys.* **1959**, *155*, 206-222.
41. Ribeiro, F.; O'Brien, J. W.; Galloway, T.; Thomas, K. V., Accumulation and fate of nano- and micro-plastics and associated contaminants in organisms. *Trac-Trend. Anal. Chem.* **2019**, *111*, 139-147.
42. Peter, S.; Meyer, H.; Baschnagel, J., Thickness-dependent reduction of the glass-transition temperature in thin polymer films with a free surface. *J. Polym. Sci. B Polym. Phys.* **2006**, *44*, 2951-2967.

Chapter 6: Conclusions and Suggested Future Work

6.1 Overall Conclusions

This dissertation focused on the use of a powerful surface analysis technique, a quartz crystal microbalance with dissipation monitoring (QCM-D) for different polymer thin film measurements. The interactions between natural polymer films in plant and fungal cell walls, solvent resistance of crosslinked thermoplastic films, and the evolution of physiochemical changes during photo-oxidation degradation of thermoplastic films were investigated by QCM-D and other techniques.

Adsorption of mixed-linkage glucan (MLG) onto regenerated chitin (RChitin) and cellulose (RC) surfaces was investigated by QCM-D and atomic force microscopy (AFM). MLG was irreversibly adsorbed onto both surfaces from QCM-D results. The adsorbed MLG layers have a thickness around 10 nm and formed hydrogel-like layers with viscoelastic properties obtained from viscoelastic modeling. Surface concentrations of adsorbed MLG on both RChitin and RC surfaces were quantified based upon modeling results. Compared with RC surfaces, adsorption of MLG onto RChitin surfaces tended to be more dissipative and hydrogel-like, resulting in layers with larger thicknesses. This work established a QCM-D method to mimic and assemble the natural polymers of fungal cell walls.

Crosslinked poly(ether imide) (X-PEI) was prepared from azide-terminated N_3 -PEI- N_3 via a simple thermal crosslinking method. Despite the lower molecular weights of oligomer precursors, X-PEIs possessed higher glass transition temperature (T_g) and storage moduli than high-molecular-weight Ultem 1010. More importantly, X-PEIs exhibited outstanding solvent-resistance to common organic solvents, including N-methyl-2-pyrrolidone, dimethylformamide, chloroform, and dichloromethane. The competing effects between N_3 -PEI- N_3 molecular weight and relative azide concentration determined that N_3 -PEI- N_3 -8 had the highest crosslinking density with the best

physical properties (highest T_g , storage modulus, and solvent resistance). This study presents a simple and efficient method to prepare the first solvent-resistant and yet processing friendly PEI from oligomers. It advances the chemistry of polymer materials and can be applicable to other polymers for different applications.

The effect of photooxidative aging on the physiochemical properties of low-density polyethylene (LDPE) were investigated using QCM-D, differential scanning calorimetry (DSC), and tensile stress-strain tests. The crystallinity, mechanical properties, and weight loss were correlated to understand the aging behavior. LDPE degraded slowly and generated water-soluble small molecules and fragmented plastic pieces during UV aging. Consequently, damaged polymer films had higher tensile stress and modulus, with reduced mass and elongation properties. The aging-induced damage of polymer chain integrity was first determined by QCM-D through the evolution of mass loss during aging, providing support to the changes of mechanical properties under aging, which may bridge the gap between molecular network evolution and its effects on the overall macroscopic mechanical changes.

6.2 Suggested Future Work

6.2.1 Adsorption of Mannan onto MLG coated RChitin Films and Chitinase Accessibility Evaluation

Some fungi are toxic and can cause instant death in plants, animals and humans.¹⁻² Hence, fungal invasion is an important issue in medical and scientific research over the past decades. Pathogenic fungal cells can attack beneficial plant cell hosts by adhering themselves onto the plant cells (Figure 6.1).³⁻⁴ Afterwards, fungal cells will penetrate and destroy the multilayered plant cell walls via enzymatic degradation prior to entering into plant cells, which eventually kills the plant cells. At the same time, the host plant cells excrete inhibitor proteins to prevent degradation

induced by fungal enzymes and release reactive polysaccharide enzymes to degrade the fungal cell walls.⁵⁻⁶ Therefore, investigating the interactions of natural polymer components in fungal cell walls and the enzyme accessibility are critical for understanding the fungal invasion mechanism and thus addressing the invasion issue.

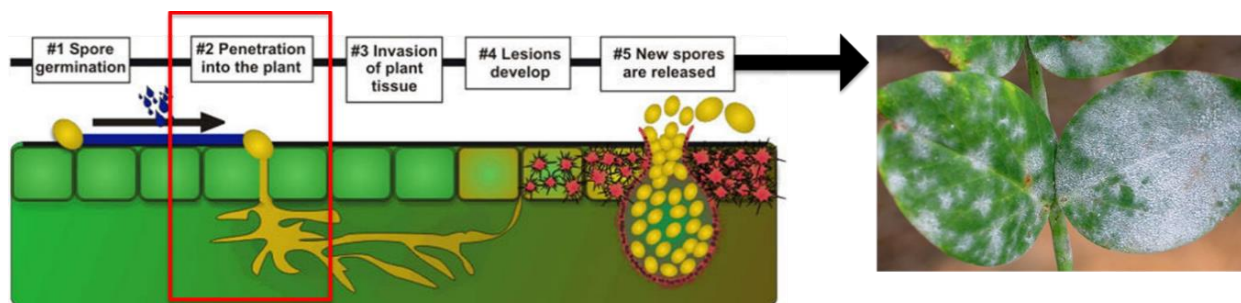


Figure 6.1 Process of fungal invasion into plants.

The fungal cell wall has a dynamic multilayer structure shown in Figure 6.1. The chitin layer exists in the inner most part of fungal cell walls next to the cell membrane and glucan layers.⁷ Above the glucan layers, there are mannan and some protein layers.^{3, 8} In chapter 3, the glucan layers were adsorbed onto RChitin films successfully using the QCM-D method. Based upon the fungal cell wall model, if we want to have a complete understanding of the interactions of components within the cell wall, it is necessary to study the adsorption of the top layer, mannan, onto the glucan coated RChitin films by QCM-D. Once the mannan is adsorbed, a complete cell wall model will be assembled, and chitinase accessibility experiments can be conducted by flowing enzyme solution into the system using QCM-D.

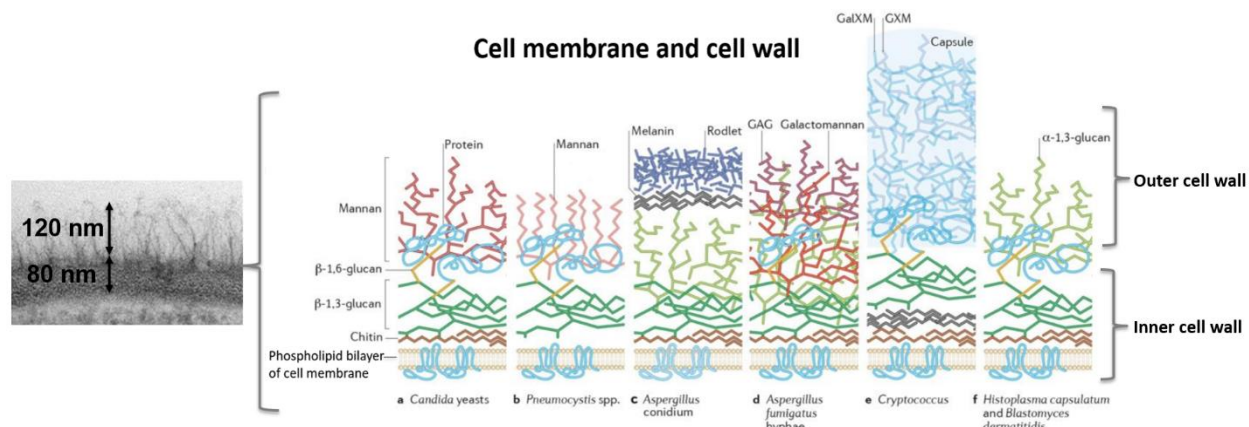


Figure 6.2 Structures of the fungal cell walls. Adapted from Hardison et al. (Copyright 2012 Springer Nature).⁹

6.2.2 Interaction Parameters (χ) between Different Solvents and Regenerated Chitin (RChitin) Films

Chitin was first found and isolated in the early nineteenth century from insects, fungi and plants as a protective biomaterial.¹⁰⁻¹² It is well acknowledged that the attractiveness of chitin resides in its low toxicity, biocompatibility, and biodegradability. Thus, owing to the large availability and structural versatility, chitin is modified as various kinds of new functional biomaterials which have been widely explored as antimicrobial agents, matrices for drug release, or wound-dressing materials.^{11, 13-14} However, modification of chitin has been limited by the lack of organic solubility due to the high molecular weight and hydrogen bonding of chitin.¹⁵⁻¹⁶ Therefore, very few studies have examined fundamental thermodynamic properties of chitin, such as solubility parameters (δ) and Flory-Huggins interaction parameters (χ) with different solvents.¹⁷⁻¹⁹

Based upon the theory that a polymer solvent is a solvent with the approximately the same solubility parameter (δ) as the polymer, chitin ($\delta = 11.0-12.5$), different common solvents including butanol ($\delta = 11.30$), isopropanol ($\delta = 11.6$), dimethylformamide ($\delta = 12.1$) and ethanol ($\delta = 12.9$) will be chosen for following solvent vapor sorption experiments.

According to the approach of Grissom et al.,¹⁷ this project will examine vapor sorption into chitin films prepared through spin coating as a function of solvent activity. The solvent activity is defined as $a_1 = P_1/P_1^*$, where P_1 is the vapor pressure and P_1^* is the vapor pressure of the pure liquid at the temperature of the film. The volume fraction of the polymer (ϕ_2) will be deduced from QCM-D sorption data. According to Flory-Huggins theory for polymer solutions, χ can be deduced from Equation 3.

$$\ln a_1 = \ln \left(\frac{P_1}{P_1^*} \right) = \ln(1 - \phi_2) + \phi_2 + \chi\phi_2^2 \quad (6.1)$$

From measurements with different solvent systems, estimation of the solubility parameter (δ) and a good solvent for chitin are expected from the minimum of a plot of χ vs δ . Subsequent work will focus on the production of chitin derivatives from analogous methods of cellulose and other polysaccharides to develop novel chitin derivatives with better solubility characteristics. A preliminary result of volume fractions (ϕ_2) of RChitin films and the corresponding interaction parameters (χ) at different pyridine activities from QCM-D measurements is shown in Table 6.1 below.

Table 6.1 Vapor sorption results between pyridine and RChitin films.

Solvent	a_1	ϕ_2 RChitin	χ RChitin
Pyridine	0.89	0.073 ± 0.009	1.8
	0.80	0.059 ± 0.008	1.9
	0.71	0.049 ± 0.005	1.9
	0.59	0.039 ± 0.004	1.9
	0.49	0.032 ± 0.002	1.9
	0.40	0.027 ± 0.002	1.8
	0.32	0.018 ± 0.005	2.0
	0.22	0.011 ± 0.002	2.1
	0.14	0.008 ± 0.002	2.0

6.2.3 Crosslinking of Modified Poly(tetrafluorophenyl 4-vinylbenzene sulfonate) Films and Crosslinking Density from QCM-D Experiments

Chapter 4 demonstrates the significant role of crosslinking density to the properties of polymers, including the mechanical, thermal, and solvent resistance properties.²⁰ Therefore, if we can develop a simple method to quantify the crosslinking density of a material, it will be beneficial for people to have a deeper knowledge of the properties of that specific material and thus explore its potential applications.²¹⁻²² Based upon the above information, the cross-linking groups can be introduced into a specific polymer system to produce model networks.²³⁻²⁵ Afterwards, a characterization technique should be chosen to determine the crosslinking density.

A possible plan is to prepare poly(tetrafluorophenyl 4-vinylbenzene sulfonate) materials and introduce QCM-D technique for the further characterization. This polymer can be spin-coated onto the QCM-D sensor, easily modified, and crosslinked by introducing the crosslinking reagent, ethylenediamine shown in Figure 6.3. After that, QCM-D can be applied to study the solvent vapor uptake towards crosslinked polymer films. The crosslinking density could be deduced from the Flory-Huggins's Theory combined with Flory-Rehner Equation based upon the swelling data from QCM-D.

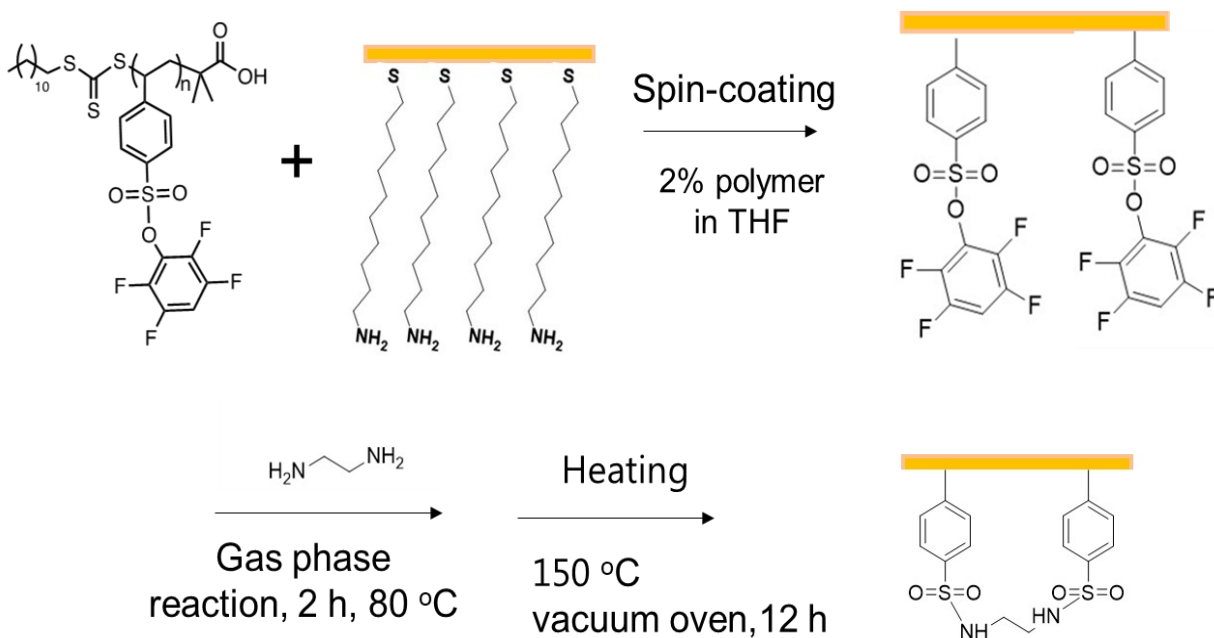


Figure 6.3 Crosslinking of modified poly(tetrafluorophenyl 4-vinylbenzene sulfonate) films.

6.3 References

1. Geoghegan, I.; Steinberg, G.; Gurr, S., The Role of the Fungal Cell Wall in the Infection of Plants. *Trends Microbiol.* **2017**, *25*, 957-967.
2. Oliver, R. P.; Solomon, P. S., Recent fungal diseases of crop plants: is lateral gene transfer a common theme? *Mol. Plant Microbe Interact.* **2008**, *21*, 287-293.

3. Free, S. J., Fungal cell wall organization and biosynthesis. *Adv. Genet.* **2013**, *81*, 33-82.
4. Chaffin, W. L., *Candida albicans* cell wall proteins. *Microbiol. Mol. Biol. Rev.* **2008**, *72*, 495-544.
5. Keegstra, K., Plant cell walls. *Plant Physiol.* **2010**, *154*, 483-486.
6. Ham, K. S.; Wu, S. C.; Darvill, A. G.; Albersheim, P., Fungal pathogens secrete an inhibitor protein that distinguishes isoforms of plant pathogenesis-related endo- β -1, 3-glucanases. *Plant J.* **1997**, *11*, 169-179.
7. Kang, X.; Kirui, A.; Muszynski, A.; Widanage, M. C. D.; Chen, A.; Azadi, P.; Wang, P.; Mentink-Vigier, F.; Wang, T., Molecular architecture of fungal cell walls revealed by solid-state NMR. *Nat. Commun.* **2018**, *9*, 2747-2758.
8. Gow, N. A. R.; Latge, J. P.; Munro, C. A., The Fungal Cell Wall: Structure, Biosynthesis, and Function. *Microbiol. Spectr.* **2017**, *5*, 1-25.
9. Hardison, S. E.; Brown, G. D., C-type lectin receptors orchestrate antifungal immunity. *Nat. Immunol.* **2012**, *13*, 817-822.
10. Carvalho, L. C.; Queda, F.; Santos, C. V.; Marques, M. M., Selective Modification of Chitin and Chitosan: En Route to Tailored Oligosaccharides. *Chem. Asian J.* **2016**, *11*, 3468-3481.
11. Zargar, V.; Asghari, M.; Dashti, A., A Review on Chitin and Chitosan Polymers: Structure, Chemistry, Solubility, Derivatives, and Applications. *ChemBioEng. Rev.* **2015**, *2*, 204-226.
12. Rinaudo, M., Chitin and chitosan: Properties and applications. *Prog. Polym. Sci.* **2006**, *31*, 603-632.
13. Balan, V.; Verestiuc, L., Strategies to improve chitosan hemocompatibility: A review. *Eur. Polym. J.* **2014**, *53*, 171-188.

14. Mincea, M.; Negrulescu, A.; Ostafe, V., Preparation, Modification, and Applications of Chitin Nanowhiskers: A Review. *Rev. Adv. Mater. Sci.* **2012**, *30*, 225-242.
15. Minke, R.; Blackwell, J., The structure of alpha-chitin. *J. Mol. Biol.* **1978**, *120*, 167-181.
16. El Knidri, H.; Belaabed, R.; Addaou, A.; Laajeb, A.; Lahsini, A., Extraction, chemical modification and characterization of chitin and chitosan. *Int. J. Biol. Macromol.* **2018**, *120*, 1181-1189.
17. Grissom, T. G.; Serrine, J. M.; Long, T. E.; Esker, A. R.; Morris, J. R., Interaction parameters for the uptake of sulfur mustard mimics into polyurethane films. *Prog. Org. Coat.* **2017**, *107*, 14-17.
18. Ravindra, R.; Krovvidi, K. R.; Khan, A. A., Solubility parameter of chitin and chitosan. *Carbohydr. Polym.* **1998**, *36*, 121-127.
19. Hu, X.; Du, Y.; Tang, Y.; Wang, Q.; Feng, T.; Yang, J.; Kennedy, J., Solubility and property of chitin in NaOH/urea aqueous solution. *Carbohydr. Polym.* **2007**, *70*, 451-458.
20. Xu, Z.; Liu, G.; Cao, K.; Guo, D.; Serrano, J.; Esker, A.; Liu, G., Solvent-Resistant Self-Crosslinked Poly(ether imide). *Macromolecules* **2021**, *54*, 3405-3412.
21. Xu, Z.; Croft, Z. L.; Guo, D.; Cao, K.; Liu, G., Recent development of polyimides: Synthesis, processing, and application in gas separation. *J. Polym. Sci.* **2021**, *59*, 943-962.
22. Shen, J.; Lin, X.; Liu, J.; Li, X., Effects of cross-link density and distribution on static and dynamic properties of chemically cross-linked polymers. *Macromolecules* **2018**, *52*, 121-134.
23. Liu, C.; Wang, J. Y.; Lin, E. C.; Zong, L. S.; Jian, X. G., Synthesis and properties of phthalonitrile-terminated oligomeric poly(ether imide)s containing phthalazinone moiety. *Polym. Degrad. Stab.* **2012**, *97*, 460-468.

24. Powell, C. E.; Duthie, X. J.; Kentish, S. E.; Qiao, G. G.; Stevens, G. W., Reversible diamine cross-linking of polyimide membranes. *J. Membr. Sci.* **2007**, *291*, 199-209.
25. Jung, M. S.; Joo, W. J.; Kwon, O.; Sohn, B. H.; Jung, H. T., A high-performance positive-working photosensitive polyimide: Effects of reactive end groups on the physical properties of the films. *J. Appl. Polym. Sci.* **2006**, *102*, 2180-2188.